



*Citation for published version:*

Qiu, D, Wang, H, Ma, T, Huang, J, Meng, Z, Fan, D, Bowen, CR, Lu, H, Liu, Y & Chandrasekaran, S 2024, 'Promoting Electrocatalytic Oxygen Reactions Using Advanced Heterostructures for Rechargeable Zinc-Air Battery Applications', *ACS Nano*, vol. 18, no. 33, pp. 21651-21684. <https://doi.org/10.1021/acsnano.4c02289>

*DOI:*

[10.1021/acsnano.4c02289](https://doi.org/10.1021/acsnano.4c02289)

*Publication date:*

2024

*Document Version*

Peer reviewed version

[Link to publication](#)

This document is the Accepted Manuscript version of a Published Work that appeared in final form in ACS Nano, copyright © American Chemical Society after peer review and technical editing by the publisher. To access the final edited and published work see <https://doi.org/10.1021/acsnano.4c02289>

**University of Bath**

**Alternative formats**

If you require this document in an alternative format, please contact:  
[openaccess@bath.ac.uk](mailto:openaccess@bath.ac.uk)

**General rights**

Copyright and moral rights for the publications made accessible in the public portal are retained by the authors and/or other copyright owners and it is a condition of accessing publications that users recognise and abide by the legal requirements associated with these rights.

**Take down policy**

If you believe that this document breaches copyright please contact us providing details, and we will remove access to the work immediately and investigate your claim.

# Promoting Electrocatalytic Oxygen Reactions using Advanced Heterostructures for Rechargeable Zinc-Air Battery Applications

Dingrong Qiu<sup>a,b†</sup>, Huihui Wang<sup>a,b†</sup>, Tingting Ma<sup>a,b†</sup>, Jiangdu Huang<sup>a,b</sup>, Zhen Meng<sup>a,b</sup>, Fan Dayong<sup>a,b</sup>, Chris Bowen<sup>c</sup>, Huidan Lu<sup>a,b\*</sup>, Yongping Liu<sup>a,b\*</sup>, and Sundaram Chandrasekaran<sup>a,b\*</sup>

<sup>a</sup>Guangxi Key Laboratory of Electrochemical and Magneto-chemical, Functional Materials, College of Chemistry and Bioengineering, Guilin University of Technology, Guilin, 541004 P.R. China.

<sup>b</sup>Guangxi Colleges and Universities Key Laboratory of Surface and Interface Electrochemistry, College of Chemistry and Bioengineering, Guilin University of Technology, Guilin 541004, P.R. China.

<sup>c</sup>Department of Mechanical Engineering, University of Bath, BA2, 7AY, Bath, UK.

† These authors contributed equally

## Email:

Yongping Liu: liuyp624@163.com

Huidan Lu: lhuidangl@163.com

Sundaram Chandrasekaran: yes.chandrasekaran@gmail.com & chandru@glut.edu.cn

## Abstract

In order to facilitate electrochemical oxygen reactions in electrically rechargeable zinc-air batteries (ZABs) there is a need to develop new approaches for efficient oxygen electrocatalysts. Due to their reliability, high energy density, material abundance, and eco-friendliness, rechargeable ZABs hold promise as next-generation energy storage and conversion devices. However, the large-scale application of ZABs is currently hindered by the slow kinetics of the oxygen reduction reaction (ORR) and oxygen evolution reaction (OER). However, the development of heterostructure-based electrocatalysts has the potential to surpass the limitations imposed by the intrinsic properties of a single material. This review begins with an explanation of the configurations of ZABs and the fundamentals of the oxygen electrochemistry of the air electrode. Then, we summarize recent progress with respect to the variety of heterostructures that exploit bifunctional electrocatalytic reactions and overview their impact on the ZAB performance. The range of heterointerfacial engineering strategies for improving ORR/OER and ZAB performance includes tailoring the surface

chemistry, dimensionality of catalysts, interfacial charge transfer, mass and charge transport, and morphology. We highlight the multi-component design approaches that take these features into account to create new forms of highly active bifunctional catalysts. Finally, we discuss the challenges and future perspectives on this important topic, which aims to enhance the bifunctional activity and performance of zinc-air batteries.

**Keywords:** Bifunctional electrocatalysts, Heterointerfaces, Oxygen reduction reaction, Oxygen evolution reaction, Zinc-air batteries.

## 1. Introduction

Highly efficient sustainable energy conversion and storage technologies have received significant interest due to the rising energy demand from net zero carbon emissions, electric vehicles, and consumable electronics.<sup>1-3</sup> Due to their range of potential benefits, which include safety of operation and high theoretical energy density, metal-air batteries, such as zinc–air batteries (ZABs), show significant promise compared to other batteries,<sup>4, 5</sup> where the redox reaction between the metal electrode and air electrode in a zinc-air battery (ZAB) results in the generation of electrical energy.<sup>6-8</sup> Notably, platinum (Pt) group-based noble metal materials such as Pt/C are regarded as an ideal electrocatalyst for oxygen reduction (ORR), while RuO<sub>2</sub> and IrO<sub>2</sub> are regarded as effective electrocatalysts for oxygen evolution reactions (OER); however, the major challenges include not only their high-cost and scarcity but also the effect of catalyst poisoning.<sup>4, 9-12</sup> Additional short-comings include a lack of catalytic bifunctionality and low durability.<sup>13-16</sup> Therefore, it is common practice to combine both ORR and OER catalysts, where each provides a unique function, to develop a bifunctional oxygen electrocatalyst for the discharge/charge process in rechargeable ZABs. However, their low power density and poor stability due to a slow oxygen reduction reaction (ORR) during discharge and a slow oxygen evolution reaction (OER) during charging limits

their widespread use.<sup>14, 17-19</sup> As a result, there is a need to create reliable, effective, and low-cost robust bifunctional oxygen electrocatalysts to improve the power density, recharge capability, and stability of ZABs by increasing the oxygen reaction kinetics. Generally, bifunctional ORR and OER electrocatalysis for rechargeable ZABs occur only at the interface of a solid catalyst, liquid electrolyte, and gaseous products.<sup>20-24</sup> Hence, the development of low-dimensional electrocatalysts has advanced significantly over the last few decades, in particular in the areas of active site engineering and the creation of novel catalysts. However, the performance of commonly studied bifunctional electrocatalysts based on low-dimensional nanocatalysts remains unsatisfactory.<sup>25-27</sup> The bifunctional electrocatalytic activity and the corresponding ZAB performance are rarely improved by optimizing a single physical property, such as the Gibbs free energy of adsorption/desorption for reaction intermediates. This is a result of the stability and activity of catalysts being also influenced by the local reaction environment, which is highly connected to the performance of a rechargeable ZAB.<sup>28-</sup><sup>30</sup> This indicates that there is a significant gap between present electrocatalyst research, that has a focus on conditions of high half-wave potential for ORR and low overpotential for OER, and the practical applications of rechargeable ZABs. Research on heterostructures to date are either based on metal-free and/or transition metals, and their combinations, that have emerged as alternatives to the bifunctional precious metal-based oxygen electrocatalysts, where the performance of the heterostructures is closely related to the practical application of ZAB technologies.<sup>31-36</sup> In the past few years, an increasing number of heterostructured catalysts have been designed and tested for ORR, OER, and rechargeable ZABs with industrially-relevant performance (see **Scheme 1**); this has included tailoring a range of functional properties by increasing the number of exposed active sites, electronic structure modulation, heterointerface formation, strain

engineering, defect engineering, and electrical conductivity enhancement by synergetic coupling of various metals or non-metals.<sup>33, 37-40</sup> For example, there are more than 6000 papers related to ORR, 5000 papers on OER, and 2000 papers on traditional bifunctional electrocatalysis in 2019, among more than 4000 papers with the area of heterostructured bifunctional electrocatalysts for ZABs (**Figure 1**). However, the number of papers on heterostructured bifunctional electrocatalysts for ZABs continues to grow; the research field is still relatively new when compared to research of highly active ORR and OER catalysts. Remarkably, in the last decades, several reviews have focused on carbon based materials as cathode catalysts for ZABs.<sup>41-45</sup> In addition, Dias et al.<sup>46</sup> discussed transition metal chalcogenides carbon-based cathode catalysts, while Chen et al.<sup>47</sup> overviewed recent advances in the bifunctional activity of ternary metal sulfides, without emphasis on the ZABs. Leong et al.<sup>48</sup> discussed advancements in the Zn-anode, electrolytes, and oxygen catalysts and, recently, Lv et al.<sup>49</sup> and Nazir et al.<sup>43</sup> provided a general discussion on rechargeable ZABs. In addition, Bi et al.<sup>50</sup> discussed the fundamental promises of rechargeable zinc-air versus lithium-air battery for industrial applications. However, there is a need to review the most recent advances in the heterostructured electrocatalysts in rechargeable ZABs, where it is clear that more work is necessary to develop heterostructured bifunctional electrocatalysts for ZABs, in particular due to importance for the widespread practical application of ZAB technologies.

In light of recent advances in the intriguing area of the design of heterostructured bifunctional electrocatalysts for rechargeable ZAB technologies, this review first highlights the developments in the design of the range of heterostructured bifunctional electrocatalysts. The heterostructured catalysts considered here are those commonly examined as bifunctional ORR and OER reactions for rechargeable ZABs unless

indicated. Such a threshold in the bifunctional ORR and OER potential difference ( $\Delta E = E_{j=10} - E_{1/2}$ ) of the novel heterostructures was selected since the bifunctional operation and performance is usually higher than the combination of precious metal-based electrocatalysts (e.g. Pt/C+RuO<sub>2</sub> or Pt/C+IrO<sub>2</sub>) for commercial ZAB technologies. Following a discussion of recent developments and prospects in the multiscale design of heterostructured catalysts, several important factors influencing the bifunctional electrocatalytic reactions and rechargeable ZAB performance of catalysts are examined; these include catalyst dimensionality, surface chemistry, morphology, electron transport pathway, and catalyst-electrolyte interaction for a variety of heterostructured catalysts. Finally, we propose future research directions with existing challenges in this vital topic, to further enhance the bifunctional electrocatalytic and rechargeable ZAB performance.

## 2. Impact of Bifunctional Oxygen Reactions in Rechargeable Zn–air batteries

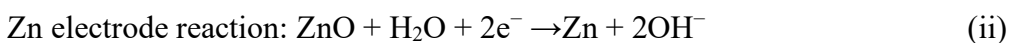
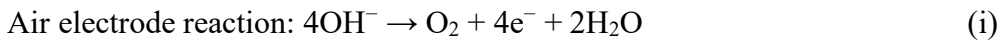
A zinc-air battery (ZAB) is a form of renewable energy technology that generates electricity through a redox reaction between a Zn metal electrode and an air electrode.<sup>25,39,51,52</sup> Rechargeable ZAB technologies have received significant attention recently because of their potential in future mobile power supplies and consumer electronics industries. Typically, rechargeable ZABs offer significant benefits compared to other battery systems in several ways. For example, because of their high open circuit voltage, high power density, extended operational life, and relatively low objective energy density (<350 W h kg<sup>-1</sup>), metal-ion batteries (particularly lithium and sodium ion batteries) have demonstrated widespread applicability in electronic devices. Furthermore, the higher energy and power density of proton exchange membrane fuel cells (PEMFCs) makes them a desirable alternative.<sup>25,36,39,51</sup> In contrast, rechargeable ZABs exhibit several favourable capabilities when compared to other potential

alternatives. These include an economical cost (today ~\$100 per kW h; and potentially expected to be as low as ~\$10 per kW h in the future), high theoretical energy density (~1353 W h kg<sup>-1</sup>), environmentally sustainable practices, and exceptional safety.<sup>25, 53</sup> As a result, ZABs are regarded as a promising alternative for the next generation innovative energy devices.

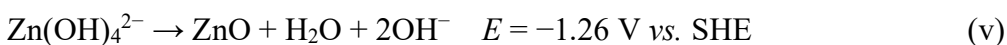
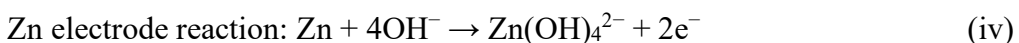
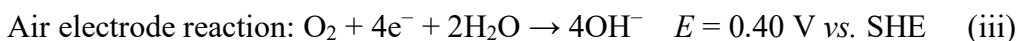
Rechargeable ZABs generally consist of a zinc (Zn) electrode, an air electrode (which contains an oxygen electrocatalyst(s), a gas diffusion layer, and a current collector), an electrolyte (typically an alkaline solution at a high concentration), and a separator, as illustrated in **Figure 2**. In general, rechargeable ZABs can be categorized into two different types, namely electrically and mechanically rechargeable ZABs.<sup>47,54</sup> The replacement of the Zn electrode and electrolyte can be used to externally recharge mechanically rechargeable ZABs.<sup>55,56,57</sup> However, it is worth noting that both types of recharging are possible and are done in rechargeable ZAB. Mechanically rechargeable ZABs were less common due to their high cost, short lifespan, erratic operation, and the emerging popularity of Li-ion batteries.<sup>57</sup> Though, materials engineering offers fascinating potential for the design of electrically rechargeable ZABs that require bifunctional oxygen electrocatalysts that enable both the OER during the recharging process and ORR during the discharging process. Typically, the working principle of rechargeable ZAB is based on redox reactions between the zinc metal electrode and air electrode.<sup>58-60</sup> The metallic Zn electrode will experience an oxidation reaction as the discharging process is taking place. This process is also accompanied by the generation and transportation of electrons, while oxygen at the air electrode and the triple interface created by solid (electrocatalysts) - liquid (electrolyte) and gas (oxygen) undergoes a reduction process to produce OH<sup>-</sup>.<sup>3, 25, 61-63</sup> During the charging process, the OH<sup>-</sup> at the triple-phase interfaces of the air electrode experiences an oxidation reaction to generate

$\text{O}_2$ , while the divalent zinc on the zinc electrode takes part in a reduction reaction to form metallic Zn. It is worth noting that the charging (OER) and discharging (ORR) reactions in rechargeable ZABs are reversible processes and may be written as follows.<sup>3,25,64-67</sup>

During the charging process:



During the discharging process:



The overall reaction is:



Owing to the multiple electron transfer process, the primary reaction sites of rechargeable ZABs are at the surface/interface of the cathode and anode, and the characteristic properties of these sites have a direct impact on the overall performance of rechargeable ZABs.<sup>32, 63, 68</sup> More importantly, whatever zinc electrode structure is used, the formation of zinc dendrites can significantly impact battery security, lifetime, and performance, regardless of the electrode structure.<sup>69-75</sup> In addition, the non-negligible hydrogen evolution (HER) process in alkaline conditions can cause the electrode to corrode and decrease its coulombic efficiency.<sup>76-79</sup> Under strong alkaline conditions, zinc would also be passivated to some extent, producing a non-conductive layer of zinc oxide. These issues have severely impacted the lifetime and consistency of ZABs, and create several risk considerations that hinder their widespread application. Currently, two major approaches have been used to resolve zinc electrode challenges,

this includes surface treatment or adding additives (e.g. copper oxide) to zinc electrodes without modifying the zinc itself.<sup>80</sup> The alternative option is to modify the zinc material to create a zinc sponge or composite material that can replace pure zinc as the electrode material for ZABs, such as by modifying or alloying with metallic components.<sup>69,81,82</sup>

Before assessing rechargeable ZABs, several considerations must be taken into account.

(i) The overall reaction indicates that a ZAB has a high open circuit voltage of  $\sim 1.66$  V; however, polarization of the zinc electrode and air electrode can result in a voltage drop. To evaluate the degree of polarization of a ZAB, an important metric in this regard is the open circuit voltage. (ii) The ratio of discharge capacity to total zinc metal consumed can be used to evaluate the energy density of a ZAB. (iii) The power density of a ZAB is directly proportional to the catalyst activity and oxygen transfer efficiency, since it is the ratio of power output to catalyst weight or electrode area. (iv) The rate performance of a ZAB refers to the output voltage at a variety of discharge current densities. (v) During the charging and discharging process, the polarization of the charge-discharge process is represented by the discrepancy between the theoretical open circuit voltage and the charge-discharge voltage. (vi) Stability is often measured in terms of charge-discharge cycles for prolonged time periods. (vii) A rechargeable ZAB energy utilization efficiency is measured by its round-trip efficiency, defined as the ratio of the charge to discharge energy capacity where the voltage is also considered with units of mWh, e.g. 5 min at -5 mA and 1.2 V, 5 min at +5 mA and 2.1 V, and the efficiency of  $\sim 57\%$ . Typically, the complex triple-phase reaction environment in the charging (OER process) and discharging (ORR process) processes leads to slow kinetic activity and mass transfer resistance, which typically limits the round-trip efficiency of ZABs ( $\sim 55\text{-}65\%$ ); it also greatly limits the large-scale application of rechargeable ZABs.<sup>25, 32, 68, 83</sup> Hence, the rational engineering of the surface and interface of an air

electrode is of significance. As a result, the use of surface/interface engineering to regulate the reaction energy barrier, electrical conductivity, reaction surface area, and mass transfer behavior in rechargeable ZABs can play a vital role in enhancing performance and is crucial for addressing the aforementioned issues. The electrocatalysts and air electrode in the electrode of a rechargeable ZAB forms a triple-phase interface reaction environment (solid-liquid-gas). The kinetic activity of the ORR and OER is determined by the surface/interface properties of electrocatalysts, whereas the surface/interface sites of air electrodes are crucial for the efficient loading of an electrocatalyst and the rapid transportation of oxygen molecules, electrolyte, and electrons.<sup>19, 25, 84-87</sup> Therefore, careful multiscale interfacial regulation may effectively regulate the electrochemical efficiency, which is highly reliant on the triple-phase reaction interface of the air electrode and the interface structure of bifunctional electrocatalysts. The next sections will provide a more in-depth discussion of these challenges.

### **3. Impact of heterostructure design for bifunctional electrocatalysis and ZABs**

In oxygen-involved heterogeneous electrocatalytic reactions, the reactant molecules are adsorbed, activated, and transformed into new oxygen-containing species at the electrocatalyst surface and interface sites.<sup>24, 25, 33, 88</sup> For example, during the OER process hydroxide ions ( $\text{OH}^-$ ) initially migrate from the bulk electrolyte and subsequently adsorb onto the active sites. Then, there is an oxidation process to form an adsorbed  $\text{OH}^*$  intermediate, which is then further oxidized to form  $\text{O}^*$  and  $\text{OOH}^*$  intermediates. Following the sequence of surface reactions, such as bond formation/breaking, it is transformed to  $\text{O}_2$  and released from active sites.<sup>88-91</sup> It is worth noting that ORR proceeds via a reversed version of OER; however, it is difficult for an electrocatalyst to simultaneously possess the optimum catalytic performance for both reactions due to their unique needs since the oxygen reaction intermediates such as

$\text{O}^*$ ,  $\text{OH}^*$ ,  $\text{OOH}^*$ , and  $\text{O}_2$  can have an impact on the catalytic capabilities of the electrocatalysts for both the ORR and OER. In addition, based on the Sabatier principle, the adsorption strength of oxygen reaction intermediates on active sites should neither be too strong, nor too weak. During the ORR process, the rate-determining step (RDS) is small and the reaction steps are a downhill Gibbs free energy.<sup>53, 91, 92</sup> However, every OER reaction step is upward, with the RDS being the largest step. As a result, an optimal ORR catalyst is often ineffective for the OER reaction, and vice versa. The need for a potential difference ( $\Delta E$ ) between the OER low overpotential to reach a current density of  $10 \text{ mA cm}^{-2}$  ( $E_{10}$ ) and the ORR half-wave potential ( $E_{1/2}$ ), where  $\Delta E = E_{j=10} - E_{1/2}$ , is a crucial factor in the development of high-performance bifunctional ORR/OER electrocatalysts and is often used as a measure of bifunctional activity.<sup>53, 92</sup> Thus optimizing the adsorption/desorption behavior of oxygen reaction using rich active sites and heterointerface engineering is a viable technique for creating high-performance ORR/OER bifunctional electrocatalysts. Remarkably, the ORR/OER reaction kinetic activity and the oxygen mass transfer at the triple-phase interfaces are both influenced by the surface/interface architectures of the electrocatalyst.<sup>39, 93, 94</sup> Notably, in a rechargeable ZAB, the enrichment of electrocatalytic efficiency is highly dependent on the triple-phase (solid-liquid-gas) interface environment.<sup>92, 95</sup> Hence, developing bifunctional electrocatalysts with an optimum interface for effective mass transfer and more exposed active sites for improving activity is of importance. An adequate amount of contact between electrocatalysts, liquid aqueous electrolytes, and oxygen ( $\text{O}_2$ ) reactants is necessary for the gas-consuming ORR process that occurs during the discharge reaction. As a gas evolution process, the OER requires the rapid removal of the  $\text{O}_2$  product for optimal performance. By balancing these oxygen gas effects, a bifunctional electrocatalyst with a well-designed structure can meet the combined requirements of the ORR and OER

processes.<sup>95, 96</sup> From this perspective, the bifunctional electrocatalytic ORR and OER performance is highly influenced by mass transport capacity, charge transfer efficiency, density of the accessible active sites, and the intrinsic reactivity of the electrocatalysts. These behaviours can be regulated and enriched using surface and interface engineering technologies to form heterostructure-based catalysts. In recent years, heterostructure-based surface and interface engineering has received significant attention for the ORR/OER and ZABs.<sup>25, 33, 96</sup> To improve electrocatalytic performance, approaches such as morphology tuning, strain/defecting engineering, electronic structure engineering via constructing heterointerfaces, nano-confinement effects, crystallographic tailoring, regulation of the catalyst/substrate interface, and catalyst/electrolyte interface engineering have been developed and employed.<sup>97-99</sup> Fine-tuning the electronic structure of an electrocatalyst is a common technique to regulate the adsorption behaviour of any reaction intermediates,<sup>25, 53</sup> since electronic interactions at the interface of a catalyst can play a critical role in modulating the electronic structure of the active species.<sup>99</sup> Interfacial effects are a result of the combination of two or more components in a heterostructure that can be triggered by changes in Fermi levels, geometric structure, and electron affinity. The Fermi level mismatch can lead to a redistribution of charge at the interface, and the built-in electric field that results from this process can lead to charge separation. Considering the geometric structure, dislocations at the lattice can lead to a generation of a tensile or compressive strain, where a shift in the d-band center also leads to the formation of defects.<sup>93, 100</sup> Furthermore, charge transfer via interfacial chemical bonding can be triggered by differences in electronic affinities, and by carefully modulating the electronic nature, these activities can increase the intrinsic activity of the catalyst.<sup>12, 101,</sup>  
<sup>102</sup> In addition, it is possible to increase the number of exposed active sites by reducing

the particle size to attain a large exposed surface area. There is also potential to modulate the interface through heterostructure formation, which can preserve the structural integrity of the high density of exposed active sites, while maintaining structural stability in the long-term. The structure-activity scaling relationship of heterogeneous catalysts is another aspect that limits catalyst activity.<sup>103-105</sup> Typically, oxygen electrocatalysis involves a number of reaction intermediates with a multistep electron transfer mechanism, and the adsorption of these intermediates are interconnected, so that optimizing the bonding strength is beneficial. Breaking such a scaling law is possible through the formation of a heterostructure and interfacial engineering, to thereby combine robust catalysts with complimentary activities.<sup>62, 103, 106-109</sup> Notably, the aforementioned effects are typically connected, either directly or indirectly, and collectively they form the foundation for hetero-interface engineering for energy conversion and storage.

#### **4. Strategic heterostructures for enhancing ORR/OER and ZABs**

##### **4.1. Metal-free heterostructures for ORR/OER and ZABs**

Carbon-based metal-free materials have excellent electrical conductivity and diversified morphologies, high specific surface area, high mechanical strength, and can achieve synergistic effects by composite design, defect engineering, and doping modification, thereby improving bifunctional electrocatalytic activity and stability. These factors can enhance the energy density, power density, and life cycle of ZABs.<sup>84, 110-113</sup> Therefore, it is of interest to employ bifunctional catalysts with excellent activity towards both the ORR and OER by fabricating heterogeneous structures containing carbon materials and active OER catalytic materials. For example, as shown in **Figure 3(i)**, Zhao et al.<sup>114</sup> reported that a unique N-SMCTs@N-rGO heterostructure with a directional interface electron transfer resulted in dual-site collaborative adsorption and

significantly lower internal resistance. In addition, rapid electron transfer and more active sites were produced by coupling higher Fermi level N-SMCTs with N-rGO to activate directional interfacial electron transfer. In addition, the creation of sub-micron sized N-SMCTs prevented the stacking of two-dimensional graphene sheets and provided a highly open and rapid mass diffusion pathway. As a result, the N-SMCTs@N-rGO catalyst exhibited an excellent  $E_{1/2}$  of ~0.87 V vs. RHE with a durability of over 20 h, greater than N-SMCTs and N-rGO. In addition, during the OER reaction, the N-SMCTs@N-rGO catalyst required a low OER potential of ~351 mV to reach a current density of 10 mA cm<sup>-2</sup>, it was higher than those of N-SMCTs (~518 mV) and N-rGO (~496 mV). Moreover, the N-SMCTs@N-rGO based ZAB exhibited a high power density of ~126 mW cm<sup>-2</sup> at 165 mA cm<sup>-2</sup>, greater than that of Pt/C+IrO<sub>2</sub> (~112 mW cm<sup>-2</sup>).

Xu et al.<sup>24</sup> developed a fabrication strategy based on metal-organic frameworks to produce a hybrid material based on 2D nitrogen-doped carbon nanotubes/graphene (GNCNTs) nanocatalysts; see **Figure 3(ii)**. Due to the enriched electronic structure modulation as a result of a synergistic hybrid coupling between the hierarchical structure and doping of heteroatom effects, the optimal GNCNTs-4 based rechargeable ZAB delivered a high specific capacity of 801 mAh g Zn<sup>-1</sup> and maximum power density of ~253 mW cm<sup>-2</sup> with excellent cyclic stability of over 3000 h at 5 mA cm<sup>-2</sup>, this outperformed commercial precious metal catalyst-based ZAB. In addition, in a N,S-GOQD-RGO/CNT heterostructure, the incorporation of CNTs prevented the stacking of graphene nanosheets, while the incorporation of N and S doping and graphene quantum dots (GOQDs) could provide an active heterointerface and thus enhance charge transport via electronic structure modulation.<sup>115</sup> As a consequence, the N,S-GOQD-RGO/CNT heterostructured hybrid showed an excellent  $E_{1/2}$  value of ~0.84 V

vs. RHE and a higher current density of  $\sim$ 5.88 mA cm $^{-2}$ . As a bifunctional catalyst, the N,S-GOQD-RGO/CNT heterostructured catalyst exhibited a lower potential difference ( $\Delta E$ ) of  $\sim$ 0.78 V and long-term stability. Furthermore, the N,S-GOQD-RGO/CNT based ZAB exhibited an excellent open circuit potential of  $\sim$ 1.414 V, and a maximum power density of  $\sim$ 134.3 mW cm $^{-2}$ , this was higher than a Pt/C+Ru/C based ZAB. As shown in **Figure 3(iii)**, it has been shown that van der Waals heterostructures produced from a combination of 2D materials and graphitic carbon significantly enhance the bifunctional electrocatalytic reactions and rechargeable ZAB performance through improved electronic conduction.<sup>116</sup> In addition, nitrogen and phosphorous-doped carbon nanotubes (CNTs) loaded on the micro-folds of graphene (CGFs) exhibited a mesoporous nature with a large specific surface area, which allows more exposed carbon skeleton of CGFs with abundant active sites.<sup>110</sup> As a result, the hybrid catalyst exhibited excellent bifunctional electrocatalytic performance with a  $\Delta E$  of  $\sim$ 0.9 V, long-term durability, and high methanol tolerance, see **Table 1**.

#### **4.2 MXene-based heterostructures for ORR/OER and ZABs**

MXene is an emerging family of 2D nanomaterials with excellent electronic, optical, mechanical, and electrochemical properties.<sup>117-119</sup> Due to its large specific surface area and flexibility of surface termination, MXene-based heterostructures have been used as an air electrode catalyst to mediate the ORR/OER in ZABs.<sup>118, 120</sup> For example, Han et al.<sup>121</sup> prepared a multi-dimensional hierarchical CoS<sub>2</sub>@MXene using CoS<sub>2</sub> nanowires and MXene nanosheets through selective etching and exfoliation by a facile hydrothermal reaction followed by a sulfurization process. The CoS<sub>2</sub>@MXene material was produced using 10 mL of MXene (referred to as CoS<sub>2</sub>@10MXene) and exhibited the best OER performance with the lowest overpotential of  $\sim$ 270 mV at 10 mA cm $^{-2}$ . Specifically, the overpotential was smaller than those of other samples,

including CoS<sub>2</sub> (~323 mV), bare MXene (~431 mV), and RuO<sub>2</sub> (~302 mV). Notably, the mixed CoS<sub>2</sub> and MXene (CoS<sub>2</sub>+MXene) showed a higher OER overpotential compared to CoS<sub>2</sub>@MXene. This result indicates that, in a CoS<sub>2</sub>@MXene electrocatalyst, the stronger electronegativity of MXene compared to CoS<sub>2</sub> can accelerate facile charge transfer from CoS<sub>2</sub> to MXene, which results in modulation of surface electronic structure. In addition, the CoS<sub>2</sub>@MXene also exhibited an excellent electrocatalytic HER activity in terms of a smaller overpotential of 175 mV compared to CoS<sub>2</sub> (~225 mV) and MXene (~260 mV) at 10 mA cm<sup>-2</sup>; this was ascribed to the synergistic effect between CoS<sub>2</sub> and MXene. Moreover, the CoS<sub>2</sub>@MXene exhibited a higher ORR onset potential ( $E_{\text{onset}}$ ) of ~0.87 V vs. RHE and a higher  $E_{1/2}$  value (0.80 V vs. RHE) compared to CoS<sub>2</sub> and MXene. This enhancement in electrocatalytic performance was attributed to a synergistic coupling between the CoS<sub>2</sub> and MXene, while the isolated 2D MXene with a large specific surface area can provide more anchored sites for active CoS<sub>2</sub>. In addition, the unique structure based on CoS<sub>2</sub> nanowires parallelly grown on MXene nanosheets can improve interfacial effects between the electrode and electrolyte; it also provides rich reaction sites and promotes mass transport of reactants to enhance the electrocatalytic activity and stability. As a consequence, a typical sandwich structured ZAB made by CoS<sub>2</sub>@MXene-based air electrode exhibited a higher peak power density of ~29 mW cm<sup>-2</sup> compared to Pt/C based ZAB (~21 mW cm<sup>-2</sup>). During discharge performance testing, the CoS<sub>2</sub>@MXene is stable at ~1.28 and 1.23 V with current densities of ~1 and 3 mA cm<sup>-2</sup>, respectively. Furthermore, the CoS<sub>2</sub>@MXene-based air electrode displayed significant long-term durability, with a small decay in the voltage gap.

Lei et al.<sup>122</sup> prepared NiCo<sub>2</sub>O<sub>4</sub>/MXene, where the ultrasmall-sized NiCo<sub>2</sub>O<sub>4</sub> nanoparticles were decorated on a few-layered MXene surface by an in situ one-pot

hydro-thermal process; see **Figure 4(i)**. Remarkably, the NiCo<sub>2</sub>O<sub>4</sub>/MXene achieves a higher  $E_{1/2}$  value of ~0.7 V vs. RHE and a larger limiting current density (~5.82 mA cm<sup>-2</sup>) compared to bare MXene and NiCo<sub>2</sub>O<sub>4</sub>. The ORR limiting current density of NiCo<sub>2</sub>O<sub>4</sub>/MXene was similar to that of Pt/C, indicating the considerable catalytic performance of the ORR. In addition, the NiCo<sub>2</sub>O<sub>4</sub>/MXene catalyst reached a low OER overpotential of ~310 mV at 10 mA cm<sup>-2</sup>, which is superior to NiCo<sub>2</sub>O<sub>4</sub> and MXene individually. As a consequence, the ZAB manufactured using the NiCo<sub>2</sub>O<sub>4</sub>/MXene electrode attained a high open-circuit potential ( $V_{oc}$ ) of ~1.40 V, and a power density of ~277 mW cm<sup>-2</sup>. This suggests the superior activity of the NiCo<sub>2</sub>O<sub>4</sub>/MXene electrode could be attributed to the NiCo<sub>2</sub>O<sub>4</sub> nanocrystals, that are grown and stabilized by Ni/Co–F bonds that acted as electrocatalytic sites for ORR and OER. Notably, using NEXAFS analysis, it was observed that Ni/Co–F bonds lead to a synergistic effect in terms of electron cloud migration, resulting in a facile charge transport during catalytic reactions. In addition, a heterostructure based on (MnCo<sub>2</sub>O<sub>4</sub>/N-GQD/MXene) and Ti<sub>3</sub>C<sub>2</sub>T<sub>x</sub> (MXene) nanosheets decorated with spinel manganese-cobalt oxide (MnCo<sub>2</sub>O<sub>4</sub>) nanoparticles and N-doped-graphene quantum dots (N-GQD) is also a high performance electrocatalyst for the reversible ORR and OER in rechargeable ZABs.<sup>123</sup> Notably, the MnCo<sub>2</sub>O<sub>4</sub>/NGQD/MXene based ZAB exhibited an excellent power density of 152.8 mW cm<sup>-2</sup>, this was higher than that of the Pt/C+IrO<sub>2</sub>/C (133.5 mW cm<sup>-2</sup>). Notably, no voltage loss was observed during long discharge times. Furthermore, the specific capacity of MnCo<sub>2</sub>O<sub>4</sub>/NGQD/MXene based battery, that was standardized to the amount of the Zn used, was 753 mAh gZn<sup>-1</sup> at  $j = 10$  mA cm<sup>-2</sup>; this was higher than a Pt/C-IrO<sub>2</sub> based battery (722 mAh gZn<sup>-1</sup>). A zinc-air battery with MnCo<sub>2</sub>O<sub>4</sub>/NGQD/MXene also shows a smaller charge-discharge gap from 0.92 to 0.94 V after 300 h. This result is indicative of superior charge-discharge behavior and

stability of MnCo<sub>2</sub>O<sub>4</sub>/NGQD/MXene bifunctional ORR/OER electrocatalyst. This enhancement was associated with the high surface area, highly porous structure, and enriched electron conductivity, thereby providing a large number of active sites and channels for electron/ion transfer. As a result of the unique morphological features and enriched charge transfer kinetics, the NiCoFe-layered double hydroxides/MXene/N-doped carbon nanotube composite exhibited a higher  $E_{1/2}$  value of ~0.78 V *vs.* RHE than NiCoFe-LDH and was similar to the Pt/C catalyst.<sup>124</sup> During an OER test, the NiCoFe-LDH/MXene/NCNT exhibited a low OER potential of ~332 mV; this was less than NiCoFe-LDH (~336 mV), IrO<sub>2</sub>/C (~353 mV), Pt/C (~492 mV) and MXene (~525mV) at a current density of 10 mA cm<sup>-2</sup>. These results demonstrate that the heterostructure formed based on NiCoFe-LDH/MXene/NCNT has the potential to be a promising non-precious electrocatalyst for the ORR/OER. As a consequence, a ZAB based on the NiCoFeLDH/MXene/NCNT electrocatalyst showed a high specific capacity of ~753 mAh g<sup>-1</sup> at a current density of 10 mA cm<sup>-2</sup> and a large energy density of 843 Wh kg<sup>-1</sup>; this was higher than the Pt/C+IrO<sub>2</sub> (826 Wh kg<sup>-1</sup>). Moreover, the battery retains its high open circuit voltage (OCP) at 1.54 V for a long time period of 80 h. Zong et al.<sup>120</sup> observed that in a Nb<sub>2</sub>CO<sub>2</sub>@COF nanocatalyst, the oxygen-terminated Nb<sub>2</sub>CO<sub>2</sub> MXene plays an active role in enhancing the hysteresis reaction of oxygen intermediates. Hui et al.<sup>125</sup> reported that, in a Ti<sub>3</sub>C<sub>2</sub>@SrTiO<sub>3</sub> hybrid heterostructure, abundant Ti-vacancy defects formed in the Ti<sub>3</sub>C<sub>2</sub> MXene can optimize the electronic structure and thus accelerate electron transfer to promote electrocatalytic redox kinetics, while the oxygen vacancies produced in the SrTiO<sub>3</sub> crystals could strengthen the absorption capability of reaction oxygen intermediates and further improve the bifunctional catalytic activity of SrTiO<sub>3</sub>, see **Figure 4(ii)**.

Wang et al.<sup>126</sup> proposed that spray-lyophilization of 2D sheets of  $\text{Ti}_3\text{C}_2\text{T}_x$  and in-situ growth of BCN nanotubes between MXene sheets may increase the specific surface area of the catalyst and expose more active sites; it may also restrict the stacking of MXenes. In this regard, Zhang et al.<sup>127</sup> developed a novel one-pot pyrolysis method to prepare a catalyst based on a nanoalloy of FeCo that was encapsulated with N-doped carbon nanotubes (CNT) along with anchored N-doped MXene (Fe/Co-CNT@MXene-T); see **Figure 4(iii)**. Among the range of Fe/Co-CNT@MXene samples examined, Fe/Co-CNT@MXene-8 exhibited the highest  $E_{1/2}$  value of  $\sim 0.85$  V vs. RHE. In addition, the Fe/Co-CNT@MXene-8 has a smaller OER overpotential than the other compositions and RuO<sub>2</sub> at the current density of 10 mA cm<sup>-2</sup>, while the overpotential of Fe/Co-CNT@MXene-7, Fe/Co-CNT@MXene-8, Fe/Co-CNT@MXene-9 and RuO<sub>2</sub> is  $\sim 379$  mV, 360 mV, 390 mV, 380 mV. Among all the as-prepared catalysts, Fe/Co-CNT@MXene-8 also shows the smallest  $\Delta E$  of  $\sim 0.73$  V, this value was lesser than a benchmark Pt/C||RuO<sub>2</sub>. As a result, the maximum power density of ZAB with Fe/Co-CNT@MXene-8 was as high as 138 mW cm<sup>-2</sup>; this activity was higher than that of Pt/C||RuO<sub>2</sub>. The specific capacity of ZAB with Fe-Co/CNT@MXene-8 reached as high as  $\sim 759$  mA h g<sup>-1</sup> at 10 mA cm<sup>-2</sup>; this was 18 mA h g<sup>-1</sup> higher than Pt/C||RuO<sub>2</sub>. In addition, the Fe-Co/CNT@MXene-8 based ZAB exhibited a steady voltage plateau during a 375 h long-term charge-discharge test operation. It has been observed that the high performance and stability could be attributed to the 3D structure. The CNT reorganizes the alignment of the  $\text{Ti}_3\text{C}_2$  flakes, leading to facile electronic transport pathways being developed on heterostructures, while the MXene acts as the electrically conductive material and the CoFe nanoalloy embedded CNT acts as the origin of active sites. Thus, due to their enhanced electronic nature, MXene-based heterostructural

design and optimization of the composition can be a promising approach for the design of ZABs with high current densities and high capacities.

#### **4.3. Precious metal-based heterostructures for ORR/OER and ZABs**

Noble metal materials, such as Pt, Pd, RuO<sub>2</sub>, and IrO<sub>2</sub>, have proven to be effective electrocatalysts for both the ORR and OER.<sup>128-133</sup> However, their large-scale application is hindered by their poor operational stability, CO<sub>2</sub> poisoning effects, scarcity, and the high cost of precious metals. To reduce production costs, an effective strategy to improve the activity of catalysts is to combine two or more non-precious catalytic materials with a small amount of precious metals to construct heterostructures.<sup>135,136</sup> These metals are used as catalysts for the oxygen reduction reaction (ORR) and oxygen evolution reaction (OER), which are vital for the application of rechargeable zinc–air batteries (ZABs). For example, Kang et al.<sup>137</sup> reported that for a Pd/CoO<sub>x</sub>/d-NC nanocatalyst, the electron-deficient palladium (Pd) and free electron at oxygen vacancies can facilitate the adsorption of oxygen species during the OER reaction, while the hybridization of defect-rich N-doped carbon with catalytically active Pd nanoparticles can improve the ORR activity and enhance the bifunctional activity. As a consequence, an aqueous Zn-air battery based on a Pd/CoO<sub>x</sub>/d-NC air electrode exhibited a high power density of 184 mW cm<sup>-2</sup>; this was higher than the benchmark of Pt/C+IrO<sub>2</sub>. Wang et al.<sup>138</sup> reported that in a Ni SAs-Pd@NC, Pd nanocrystals with sub-10 nm sized strongly contribute to the ORR activity, while the Ni-N<sub>4</sub> sites with a high atom utilization efficiency and low catalytic barriers are responsible for the OER; this results in a higher selectivity towards the respective ORR in terms of the highest onset potential ( $E_{onset} \sim 0.94\text{V}$  vs. RHE) and half-wave potentials ( $E_{1/2} \sim 0.84\text{ V}$  vs. RHE). For the OER the Ni SAs-Pd@NC exhibited a small overpotential of  $\sim 380\text{ mV}$  at  $10\text{ mA cm}^{-2}$ , close to that of RuO<sub>2</sub> and higher than Ni

SAs@NC. As a consequence, a Zn-air battery assembled with a Ni SAs-Pd@NC exhibited a high open circuit voltage (OCV) of  $\sim$ 1.44 V. In addition, the Ni SAs-Pd@NC ZAB exhibited a maximum power density of  $\sim$ 134.2 mW cm $^{-2}$ , higher than that of a Pt/C+RuO<sub>2</sub>-based ZAB ( $\sim$ 109.7 mW cm $^{-2}$ ).

Li et al.<sup>139</sup> outlined that alloying Pd and Ni could lead to a modulation of both the geometry and electronic structure of reaction sites of a PdNi/Ni@N-C catalyst, which could lead to improved performance of a bifunctional catalyst compared to mono-metallic Pd and Ni; see **Figure 5(i)**. As a consequence, PdNi/Ni@N-C-based ZABs achieved a specific capacity of  $\sim$ 719.2 mA h g<sub>Zn</sub> $^{-1}$  at 5 mA cm $^{-2}$ , corresponding to an energy density of  $\sim$ 923.3 Wh kg<sub>Zn</sub> $^{-1}$ ; this was superior to a Pd/C+RuO<sub>2</sub> driven battery. As a bifunctional catalyst, the optimal amount of Ru-loaded Ni<sub>0.5</sub>Co<sub>0.5</sub>(OH)<sub>2</sub>/CC nanoneedles (2% Ru-NCO/CC) exhibited excellent OER performance of  $\eta_{50} = 233$  mV,  $\eta_{100} = 269$  mV compared to 0.02% Ru-NCO ( $\eta_{50} = 291$  mV,  $\eta_{100} = 318$  mV), 0.2% Ru-NCO ( $\eta_{50} = 281$  mV,  $\eta_{100} = 303$  mV), and 4% Ru-NCO ( $\eta_{50} = 295$  mV,  $\eta_{100} = 318$  mV).<sup>140</sup> In addition, during ORR testing, 2% Ru-NCO/CC showed a high  $E_{1/2}$  value of  $\sim$ 0.88 V *vs.* RHE and a high kinetic current density ( $J_k@0.85$  V = 14.65 mA cm $^{-2}$ ), greater than that of a commercial noble metal Pt/C ( $E_{1/2} = 0.86$  V,  $J_k@0.85$  V = 11.83 mA cm $^{-2}$ ). It has been observed that Ru doping can modulate the electronic energy state of a NiO/Co<sub>3</sub>O<sub>4</sub> heterostructure and thereby regulate the activation energy and Gibbs free energy of the catalyst. As shown in **Figure 5(ii)**, the excellent water splitting and Zn-air battery performance of the Ru-FeRu@C/NC catalyst was attributed to effective charge transfer from the Fe atom to Ru at the interface of Ru-FeRu@C/NC, that modulated the electronic structure of the heterostructured catalyst and thus improved the reaction kinetics between the electrocatalyst and electrolyte. As a consequence, the Ru-FeRu@C/NC-based battery exhibited a high specific capacity of  $\sim$ 754.2 mAh g $^{-1}$ ,

greater than that of an IrO<sub>2</sub>||Pt/C assembled cell (~736.8 mAh g<sup>-1</sup>).<sup>141</sup> In addition, the loading of Ru in Co<sub>9</sub>S<sub>8</sub> (Ru-Co<sub>9</sub>S<sub>8</sub>) exhibits superior OER activity compared to Co<sub>9</sub>S<sub>8</sub>. Specially, the 10Ru-Co<sub>9</sub>S<sub>8</sub> material required a low OER overpotential of only 163 mV to reach 10 mA cm<sup>-2</sup>; this was lower than that of Co<sub>9</sub>S<sub>8</sub> (~300 mV), 5Ru-Co<sub>9</sub>S<sub>8</sub> (~268 mV), 20Ru-Co<sub>9</sub>S<sub>8</sub> (~325 mV), and RuO<sub>2</sub> (306 mV).<sup>142</sup> In addition, the catalyst demonstrated excellent durability over 48 h. As an ORR electrocatalyst, the samples had  $E_{1/2}$  values of ~0.75, 0.79, 0.80, 0.81, and 0.83 V vs. RHE, for Co<sub>9</sub>S<sub>8</sub>, 5Ru-Co<sub>9</sub>S<sub>8</sub>, 10Ru-Co<sub>9</sub>S<sub>8</sub>, 20Ru-Co<sub>9</sub>S<sub>8</sub>, and Pt/C respectively. In addition, it has been observed that the introduction of Ru can regulate the electronic structure of Co<sub>9</sub>S<sub>8</sub>, hence, the reaction barriers for OER and ORR were greatly reduced. As a result, the 10Ru-Co<sub>9</sub>S<sub>8</sub> based ZAB exhibited a high open circuit voltage of ~1.36 V. In addition, the ZAB displayed a maximum peak power density of ~92.0 mW cm<sup>-2</sup>; this was comparable to Pt/C+RuO<sub>2</sub> based ZAB. Of particular interest is that the 10Ru-Co<sub>9</sub>S<sub>8</sub>-based ZAB exhibited a long durability over 500 h at 5 mA·cm<sup>-2</sup> without any degradation of the charge-discharge voltage gap.

#### **4.4. Transition metal oxide/hydroxide-based heterostructures for ORR/OER and ZABs**

Transition metal oxide/hydroxide-based heterostructures (e.g. Co, Fe, Mn, Ni, and Cu) are electrocatalysts that have attracted interest due to their abundant availability, low cost, and comparable catalytic performance to noble metals.<sup>143-150</sup> These electrocatalysts have been used in electrochemical water splitting for sustainable hydrogen production and ZAB applications. Gao et al.<sup>151</sup> reported on a heterostructured bifunctional catalyst based on oxides and layered hydroxides (LDH) of CoFeRu-oxides/LDH that were prepared by partially oxidizing LDH to provide additional active sites for ORR and OER. Notably, as a bifunctional catalyst, RuO<sub>2</sub>, Fe<sub>2</sub>O<sub>3</sub>, and LDH

exhibited a high activity towards OER, whereas the  $\text{Co}_3\text{O}_4$  showed a high reactivity towards ORR. In addition, as shown in **Figure 6(i)**, due to the high electrical contact through the bimetal coupling interactions, the Fe/Co-DHO nanoparticles strongly anchored on the carbon nanotubes (FeCo-DHO/NCNTs) to provide a high ORR half-wave potential ( $E_{1/2} \sim 0.86$  V vs. RHE) and a low OER potential of  $\sim 1.55$  V than Fe-NCNTs and Co-NCNTs, respectively.<sup>152</sup> As a ZAB air electrode, the FeCo-DHO/NCNTs showed a high specific capacity of  $\sim 793.0$  mAh g<sup>-1</sup>, corresponding to energy densities of  $\sim 930.6$  Wh kg<sup>-1</sup>; this was higher than a Pt/C + RuO<sub>2</sub> catalyst (854.3 Wh kg<sup>-1</sup>). Mondal et al.<sup>153</sup> utilized the hydrothermal method to produce a 2D heterojunction of  $<20$  nm thick double perovskite oxide NSs of  $\text{Pr}_{0.5}\text{Ba}_{0.5}\text{Mn}_{1.8-x}\text{Nb}_x\text{Co}_{0.2}\text{O}_{6-\delta}$  (PBMNC- $x$ ,  $x = 0, 0.1, 0.2, 0.3, \delta = 0.38-0.59$ ) with NiFe-LDH (PBMNC/LDH-y). Notably, it was observed that the Nb-doping at the B-site of perovskites may increase the net cationic charge, which lowers the oxygen non-stoichiometry. As a result, 5 at% Nb-doping was identified to exhibit the best ORR/OER bifunctional activity compared to other samples. As shown in **Figure 6(ii)**, Moloudi et al.<sup>154</sup> proposed that a Ni-Co-Fe LDH on a Ni nanocone (NiNC)-decorated Ni foam with amorphous tri-metal borate (TMB@NiNC), can act as a high performance bifunctional electrocatalyst. As a result of a heterointerface-rich nature and self-reconstruction properties, the ZAB based on the TMB@NiNC exhibited a high open-circuit voltage of  $\sim 1.477$  V and a specific energy of  $\sim 918$  W h kg<sub>Zn</sub><sup>-1</sup>. In addition, due to the synergistic coupling of  $\text{NiCo}_2\text{O}_4$  and NiCoFe-hydroxide, the  $\text{NiCo}_2\text{O}_4@\text{NiCoFe}-\text{hydroxide}$  nanoarrays exhibited an excellent ORR and OER activity and good ZAB recharging performance.<sup>155</sup> In addition, it has been reported that in a CoN/ $\text{Co}_3\text{O}_4$  HNPs@NCNWs catalyst, interfacial engineering of CoN and  $\text{Co}_3\text{O}_4$  HNPs with NCNWs can modify the electronic structure, improve the electronic conductivity,

enhance the number of active sites, and thereby shorten the transport pathways for electron/reactants during bifunctional electrocatalytic reactions and ZAB testing.<sup>156</sup> Zhu et al.<sup>157</sup> indicated that establishing a tri-phase interfacial structure by integrating a highly-crystallized  $\text{Fe}_x\text{Ni}$  metal alloy, carbon shell, and tuneable outer active  $\text{FeO}_y$  layer could lead to facile charge transfer across a thin oxide layer at the interface, thus significantly increasing intrinsic activity during oxygen catalysis.

#### **4.5. Transition metal chalcogenide-based heterostructures for ORR/OER and ZABs**

Recently, transition metal chalcogenides have been increasingly important in energy conversion and storage applications due to their low cost, high electronic conductivity, abundant redox chemistry, remarkable electrochemical activities, and ease of production.<sup>158-160</sup> Moreover, innovative features, functionalities, and improved performance for a variety of applications have been achieved by combining two or more constituents into a heterostructure. For example, Gui et al.<sup>161</sup> reported that the synergistic coupling among ultrafine  $\text{Co}_{0.85}\text{Se}$  nanoparticles and N-doped CNFs heterostructures can lead to enriched electrochemical active sites for both the ORR and OER. As a result, a  $\text{Co}_{0.85}\text{Se}@\text{CNFs}$  heterostructure exhibited a high  $E_{1/2}$  value of ~0.84 V vs. RHE and a low OER potential of ~1.58 V vs. RHE at 10 mA cm<sup>-2</sup>. It was observed that, in a  $\text{CoSe}@\text{NMC}$  heterostructure, a nitrogen-doped mesoporous carbon (NMC) may also modify the electronic nature of CoSe nanocrystals.<sup>162</sup> In addition, as a result of the formation of a hetero-interface, the high percentage of  $\text{Ni}^{3+}$  in the nanoparticles of  $\text{Ni}_{0.85}\text{Se}-\text{NHCS}$  could serve as active sites for a bifunctional electrocatalyst toward ORR/OER.<sup>163</sup> As a result, the ZAB formed from a  $\text{Ni}_{0.85}\text{Se}-\text{NHCS}$  electrode exhibited a high discharging-charging performance and extended lifetime. Zheng et al.<sup>164</sup> outlined the synthesis of different interfacial densities of  $\text{NiSe}_2/\text{CoSe}_2$  heterostructures

by an ion injection method. Their investigation revealed that the introduction of an interface at atomic levels can potentially affect the bimetallic Ni-Co active sites (while the  $\text{Ni}^{2+}$  is easier to activate than  $\text{Co}^{2+}$ ), and facilitate electronic coupling between the selenides located within the core and the in-situ formed oxides and hydroxides to decrease the oxidation overpotential. Due to enriched active sites as a result of the heterointerface formed the  $\text{Co}_{0.85}\text{Se-NHCS}$  mixed with  $\text{Ni}_{0.85}\text{Se-NHCS}$  (i.e.,  $\text{Ni}_{0.85}\text{Se}/\text{Co}_{0.85}\text{Se-NHCS-2}$ ) exhibited an enhanced ORR and OER catalytic activity compared to single selenide catalysts, see **Figure 7(i)**.<sup>165</sup> Notably, the OER and ORR enhancement of  $\text{Ni}_{0.85}\text{Se}/\text{Co}_{0.85}\text{Se-NHCS-2}$  was attributed to the enriched  $\text{Ni}^{3+}$  in  $\text{Ni}_{0.85}\text{Se-NHCS}$  and abundant  $\text{Co}^{2+}$  in  $\text{Co}_{0.85}\text{Se-NHCS}$  active sites, respectively. Moreover, a ZAB based on a  $\text{Ni}_{0.85}\text{Se}/\text{Co}_{0.85}\text{Se-NHCS-2}$  catalyst exhibited an outstanding charge and discharge performance and high stability compared to precious metal-based catalysts. In addition, due to modulation of the electronic structure, a ZAB based on a bifunctional electrocatalysts of  $\text{Co}_9\text{S}_8/\text{Co}_{1-x}\text{S@NSC}$  demonstrated an excellent open circuit potential of  $\sim 1.48$  V, while the maximum power density was  $\sim 141.9$  mW cm $^{-2}$  at 189.2 mA cm $^{-2}$ , and outperformed the Pt/C+IrO<sub>2</sub> catalyst-based system ( $\sim 116.3$  mW cm $^{-2}$  at 157.1 mA cm $^{-2}$ ).<sup>166</sup> Peng et al.<sup>167</sup> proposed that the incorporation of an optimal amount of ZnS into N and S-doped carbon could be beneficial to regulate the bifunctional catalytic properties through electronic coupling and an increase in the number of active sites for the bifunctional electrocatalytic reactions. In addition, Shang et al.<sup>168</sup> reported on a unique  $\text{MoS}_2@\text{Co-Fe}$  heterojunction structure with a nitrogen-doped carbon, which could optimize the electronic structure of the active centers for ORR and OER, and thereby enhance ZAB performance. Cao et al.<sup>169</sup> demonstrated that creating heterointerfaces of  $\text{NiS}_2/\text{CoS}_2$  nanohybrids could accelerate the rapid charge transfer rate during bifunctional catalysis, see **Figure 7(ii)**.

As a result, the NiS<sub>2</sub>/CoS<sub>2</sub> displayed OER potential of ~295 mV at 10 mA cm<sup>-2</sup>; this was ~61, 92 and 101, 61 and 92 mV lower than that of Ir/C, NiS<sub>2</sub>, and CoS<sub>2</sub>, respectively. However, after the OER reaction, the structure of NiS<sub>2</sub>/CoS<sub>2</sub> showed some agglomeration and an amorphous nature, which may be due to the formation of an amorphous layer on the surface of NiS<sub>2</sub>/CoS<sub>2</sub> nano hybrid electrode. Meanwhile, the NiS<sub>2</sub>/CoS<sub>2</sub> displayed a low ORR onset potential ( $E_{onset}$ ) of ~0.90 V vs. RHE and a  $E_{1/2}$  value of ~0.79 V vs. RHE. In addition, the ZAB based on NiS<sub>2</sub>/CoS<sub>2</sub> electrode displayed a high power density of 101 mW cm<sup>-2</sup>, higher than a Pt/C+Ir/C system. The improved ZAB performance of NiS<sub>2</sub>/CoS<sub>2</sub> was attributed to the synergistic effect between the two domains that resulted in improved electron conductivity and increased catalytic active sites, as well as optimized the chemisorption /desorption efficiency and improved rate of mass transfer.

#### **4.6. Transition metal phosphides-based heterostructures for ORR/OER and ZABs**

Recent research has shown that heterostructured transition metal phosphides (TMPs) are superior to single transition metal phosphides in terms of catalytic activity.<sup>170-174</sup> This is due to the fact that TMP-based heterostructures can enhance conductivity and surface reaction active sites, leading to superior catalytic and ZAB performance. For example, Shi et al.<sup>175</sup> proposed that, in a Co<sub>2</sub>P-NPC/CF catalyst, the simultaneous doping of P and N atoms in carbon may induce an enhanced coupling of Co<sub>2</sub>P NPs with N, P-co-doped carbon, which can improve the exposure of bifunctional catalytic active sites and ZAB performance. In addition, due to the use of multi-component hollow spheres of CoP<sub>x</sub> wrapped in N-doped graphitic carbon, the Co<sub>x</sub>P-NC-420 showed the highest ORR activity with an excellent  $E_{1/2}$  value of 0.860 V vs. RHE; this was higher than that of 0.824 V vs. RHE for Pt/C.<sup>176</sup> In addition, the Co<sub>x</sub>P-NC-420 showed the lowest OER overpotential of 273 mV and a Tafel slope of 81 mV

$\text{dec}^{-1}$ . As a result of the effect of the use of a multicomponent system, a charge transfer resistance of  $87.8 \Omega$  was attained for  $\text{Co}_x\text{P-NC-420}$ , indicating a rapid electron transfer rate for the catalyst. Notably, the  $\text{Co}_x\text{P-NC-420}$  based ZAB exhibited an open-circuit potential of 1.374 V, this was  $\sim 27$  mV lower than 1.401 V for the Pt/C based ZAB. Remarkably, the incorporation of Cu atoms on the  $\text{Co}_2\text{P}/\text{carbon}$  nanofiber (Cu- $\text{Co}_2\text{P}/\text{CNFs}$ ) prepared by electrospinning, followed by high-temperature heat treatment, showed an excellent electronic reconfiguration.<sup>177</sup> As a consequence, the optimal amount of Cu doping of 7% Cu-Co<sub>2</sub>P/CNFs showed a high  $E_{1/2}$  value of  $\sim 0.792$  V vs. RHE, it was higher than 4% Cu-Co<sub>2</sub>P/CNFs; the 10% Cu-Co<sub>2</sub>P/CNFs and showed a similar activity to Pt/C. In addition, the OER overpotential of 7% Cu-Co<sub>2</sub>P/CNFs was  $\sim 360$  mV and was larger than 4% Cu-Co<sub>2</sub>P/CNFs ( $\sim 370$  mV), Cu-Co<sub>2</sub>P/CNFs ( $\sim 400$  mV), and Co<sub>2</sub>P/CNFs ( $\sim 410$  mV), signifying the electronic coupling of Cu and the formation of active hydroxide species. Moreover, the ZAB based on 7% Cu-Co<sub>2</sub>P/CNFs exhibited a high discharge current density and the power density of  $\sim 375.0$   $\text{mA cm}^{-2}$  and  $\sim 230$   $\text{mW cm}^{-2}$ , respectively; this activity was higher than the Pt/C-RuO<sub>2</sub> based battery ( $\sim 156.3$   $\text{mA cm}^{-2}$  and  $\sim 79.6$   $\text{mW cm}^{-2}$ ), and a long term durability of over 80 h was also observed. In addition, Co<sub>2</sub>P@N,P-doped carbon polyhedral derived from CoCo-PBA and melamine have been shown to promote a high charge transfer rate and enhance the ORR/OER kinetics compared to Co@NC-1, Co@NC-2 and CoP@NPPC.<sup>178</sup> Notably, the open-circuit voltage of Co<sub>2</sub>P@NPPC-based ZABs ( $\sim 1.4$  V) was higher than that of Pt/C+RuO<sub>2</sub>-based ( $\sim 1.373$  V). As a result, the peak power density of Co<sub>2</sub>P@NPPC-based primary ZABs was  $\sim 226$   $\text{mW cm}^{-2}$ ; this was superior to the Pt/C-RuO<sub>2</sub>-based ZAB ( $\sim 215$   $\text{mW cm}^{-2}$ ). In addition, the Co<sub>2</sub>P@NPPC-based ZAB showed excellent recharge ability for 160 h at  $10 \text{ mA cm}^{-2}$ . Nanohybrids of the Ni<sub>x</sub>P nanoparticle anchored N, namely P-doped porous carbon (Ni<sub>x</sub>P-NP-C900) were

fabricated from hexagonal NiZn-MOFs and demonstrated a high ORR  $E_{\text{onset}}$  and  $E_{1/2}$  values of 0.9 V and 0.76 V vs. RHE, respectively; this was much higher than the  $\text{Ni}_x\text{P-NP-C1000}$ , and exhibited similar activity to 20%Pt/C.<sup>179</sup> In addition, it was predicted that the small  $\text{Ni}_2\text{P}$  nanoparticles could act as active sites to enhance the bifunctional ORR and OER catalytic activity and increase durability. In addition, a synergetic coupling between the  $\text{Ni}_x\text{P}$  and N-P doped carbon skeleton may induce structural defects and thereby regulate the electronic structure to result in a greater number of exposed active sites and improved catalytic activity. As a consequence, the  $\text{Ni}_x\text{P-NP-C900}$  based ZAB delivered a high power density of  $\sim 266 \text{ mW cm}^{-2}$  and a small charge-discharge voltage gap. It has also been demonstrated that, in a Ni-Fe based heterostructured catalysts, the Ni/Fe metal ratios could influence the ORR and OER activity via regulated coupling effect and electronic structure modulation, see **Figure 8(i)**.<sup>180</sup> As a consequence, the  $\text{NiFe(1:2)P/Pi}$  catalyst exhibited a high ORR  $E_{\text{onset}}$  value of  $\sim 0.98 \text{ V}$  vs. RHE and a low OER overpotential of  $\sim 0.21 \text{ V}$  at  $10 \text{ mA cm}^{-2}$  with the lowest potential difference ( $\Delta E = E_{10} - E_{1/2}$ ) of  $\sim 0.62 \text{ V}$ ; this surpasses a benchmark  $\text{Pt/C+RuO}_2$  catalysts. In addition, the  $\text{NiFe(1:2)P/Pi}$ -based ZAB demonstrated an outstanding discharge capacity of  $900 \text{ mAh g}^{-1}$  @ $10 \text{ mA cm}^{-2}$  and a high power density of  $395 \text{ mW cm}^{-2}$  along with steady cycles. Due to the synergetic coupling between the nanocrystals of CoFeP and N-P doped carbon, the  $\text{CoFeP@C}$  exhibited an excellent bifunctional electrocatalytic reaction and ZAB performance, see **Figure 8(ii)**.<sup>181</sup> It has also been observed that there is in-situ conversion of metal derivatives, such as metal chalcogenides and metal phosphides, to corresponding metal oxides, hydroxides, and/or oxyhydroxide under accelerated environments during OER and/or ORR of rechargeable ZABs, which reduces the Gibbs free energies.<sup>182,183</sup>

#### 4.7 Other mixed heterostructures for ORR/OER and ZABs

Mixed-heterostructures, that involve the combination of materials with multiple dimensionalities, provide a wide range of multi-functionality that cannot be simply achieved by a pure heterostructure material.<sup>39, 184, 185</sup> Typically, across the mixed-interfaces, the degree of electrostatic screening and the discontinuous changes in the energy dependence of the density of states can alter the magnetic, electrical, optical, and thermal properties, thereby introducing novel and/or enhanced functionalities.<sup>186-</sup><sup>189</sup> For example, due to the enriched electronic charge density by the coupling of CeO<sub>2</sub> with CoSe<sub>2</sub>-NCs, the CeO<sub>2</sub>@CoSe<sub>2</sub>-NCs, the CeO<sub>2</sub>@CoSe<sub>2</sub>-NCs required a low OER overpotential of ~0.32 V to reach a current density of 10 mA cm<sup>-2</sup>, while it exhibited the high  $E_{1/2}$  value of ~0.76 V vs. RHE. Notably, the ORR performance of CeO<sub>2</sub>@CoSe<sub>2</sub>-NCs is almost similar to the Pt/C. In addition, the peak power density of CeO<sub>2</sub>@CoSe<sub>2</sub>-NCs based ZABs was ~153 mWcm<sup>-2</sup>, and was higher than that of the ZABs assembled with the Pt/C-IrO<sub>2</sub> (~138 mWcm<sup>-2</sup>).<sup>190</sup> Zhang et al.<sup>191</sup> proposed that due to the combined effect of the formation of a heterostructure with a large pore volume via a porous structure of Co/Co<sub>9</sub>S<sub>8</sub>@SNC-900, rapid charge and mass transfer rates were facilitated. As a result, the Co/Co<sub>9</sub>S<sub>8</sub>@SNC-900 exhibited a high diffusion-limited current density of ~5.2 mA cm<sup>-2</sup>; this activity was similar to commercial Pt/C (5.5 mA cm<sup>-2</sup>). The Co/Co<sub>9</sub>S<sub>8</sub>@SNC-900 exhibited a high  $E_{1/2}$  value of ~0.82 V vs. RHE, and this performance was similar to commercial Pt/C (~0.84 V vs. RHE). The electrocatalytic OER activity of Co/Co<sub>9</sub>S<sub>8</sub>@SNC-900 showed a low overpotential of ~0.31 V at a current density of 10 mA cm<sup>-2</sup>, indicating its OER activity is the best among all other prepared samples including RuO<sub>2</sub>. Moreover, after OER stability testing, the Co/Co<sub>9</sub>S<sub>8</sub>@SNC-900 maintained a stable rod structure, signifying the robustness of Co/Co<sub>9</sub>S<sub>8</sub>@SNC900. As a bifunctional electrocatalyst, the Co/Co<sub>9</sub>S<sub>8</sub>@SNC-900 exhibited a potential difference ( $\Delta E$ ) of ~0.73 V, which was lower

than that of a precious metal catalyst (~0.78 V). In addition, the Co/Co<sub>9</sub>S<sub>8</sub>@SNC-900 based ZAB delivered a high power density of ~106.6 mW cm<sup>-2</sup> at a current density of 163.2 mA cm<sup>-2</sup>; this was higher than a ZAB based on Pt/C+ RuO<sub>2</sub> (~105 mW cm<sup>-2</sup> at 161.8 mA cm<sup>-2</sup>). As shown in **Figure 9(i)**, due to the enriched active sites through the formation of a heterostructure of Co<sub>3</sub>W<sub>3</sub>C/CoP nanoparticles anchored on N, the P-doped hierarchically porous carbon fibers showed excellent bifunctional ORR and OER performance compared to Co@WC<sub>1-x</sub>/NCNTs (N-doped carbon nanotubes), W<sub>2</sub>N/WC, FeCo/Co<sub>2</sub>P@NPCF, Co/CNFs (1000).<sup>192</sup> As a consequence, the CoWCP-NPC-2:1-based Zn-air battery exhibited a high open circuit voltage of ~1.41 V and was stable for 12 h, where the open circuit voltage was ~31 mV higher than Pt/C based ZAB. The CoWCP-NPC-2:1 achieved a higher peak power density of ~205.5 mW cm<sup>-2</sup> than Pt/C (~75.1 mW cm<sup>-2</sup>). In addition, it has been validated that the formation of a Mott-Schottky heterojunction based on Co/Co<sub>2</sub>P nanoparticles encapsulated in the intertwined NPCNT skeletons could improve the bifunctional electrocatalytic activity through the formation of a favorable pathway for electron transport, see **Figure 9(ii)**.<sup>193</sup>

Tian et al.<sup>194</sup> proposed that the formation of a heterointerface of Co<sub>9</sub>S<sub>8</sub> and CoO in a Co–S–O/NSCN electrocatalysts could modulate the electron distribution, and develop a local electric field around the hetero-interface, thereby accelerating the electron transfer efficiency for facile electrocatalytic ORR and OER process. Moreover, it was predicted that the formation of the hetero-interface by two different crystal phases may lead to structural distortion and hence result in a large active surface area for bifunctional electrocatalytic reactions. As a result, the Co–S–O/NSCN exhibited an excellent  $\Delta E$  value (~0.80 V) compared to a commercial Pt/C system (~0.91 V). In addition, an assembled ZAB battery based on Co–S–O/NSCN was able to deliver an open-circuit voltage of ~1.47 V, with a maximum power density of ~162 mW cm<sup>-2</sup> at

$241 \text{ mA cm}^{-2}$ ; this was superior to the Pt/C based ZAB ( $\sim 93 \text{ mW cm}^{-2}$  at  $139 \text{ mA cm}^{-2}$ ).

The  $\text{CoSe}_2/\text{Co@NCNF-3}$  heterostructure helps to regulate the adsorption of reaction intermediates and improve catalytic efficiency.<sup>195</sup> In addition, the catalyst demonstrated long-term durability compared to Pt/C and  $\text{IrO}_2$  in ORR and OER respectively. Hu et al.<sup>196</sup> reported that oxygen vacancies/defects formed during the formation of a heterostructure of  $\text{NiFe}/\text{NiSe}_2@\text{NCNT}$  catalyst could promote the bifunctional catalytic activity towards the ORR ( $E_{1/2}=0.811 \text{ V vs. RHE}$ ), and OER ( $\eta=292 \text{ mV}@10 \text{ mA cm}^{-2}$ ) with a low  $\Delta E$  of  $\sim 0.711 \text{ V}$ , which greatly improved the ZAB performance; see **Figure 10(i)**. Furthermore, Wang et al.<sup>197</sup> proposed that in a  $\text{CoS}/\text{CoO}$  porous nanorod (PNRs) heterostructure, the  $\text{CoO}$  surface may lead to a lower Fermi level and larger work function, so that electrons tend to flow from  $\text{CoS}$  to  $\text{CoO}$ ; this results in enhanced bifunctional electrocatalytic ORR and OER performance, see **Figure 10(ii)**. Notably, a ZAB based on  $\text{CoS}/\text{CoO}$  PNRs delivered a high open circuit voltage (OCV) of  $\sim 1.35 \text{ V}$  and a peak power density of  $\sim 58.8 \text{ mW cm}^{-2}$  that was higher than a Pt/C +  $\text{RuO}_2$ -based ZAB ( $\sim 55.1 \text{ mW cm}^{-2}$ ). Due to the highly exposed active surface area and synergistic coupling at its interfaces, the  $\text{FeCo}_2\text{O}_4@\text{FeCo}_2\text{S}_4/\text{NF}$  showed an excellent bifunctional ORR and OER performance.<sup>198</sup> Moreover, the  $\text{FeCo}_2\text{O}_4@\text{FeCo}_2\text{S}_4/\text{NF}$ -based ZAB achieved a peak power density of  $\sim 189.75 \text{ mW cm}^{-2}$  at  $10 \text{ mA cm}^{-2}$ . Notably,  $\text{FeCo}_2\text{O}_4@\text{FeCo}_2\text{S}_4/\text{NF}$ -based ZAB displayed a negligible charge/discharge voltage gap and good cycling capacity of up to  $\sim 227 \text{ h}$  at  $10 \text{ mA cm}^{-2}$ . In addition, it has been reported that the  $\text{CoNi}/\text{CoNiP}$  heterostructure anchored on a 3D MXene framework with a hierarchical structure can modulate the electron transfer rate via a synergetic coupling that facilitates the mass transfer of the reactants and provide facile paths for reactant diffusion, thereby significantly enhancing electrocatalytic bifunctional reaction kinetics and ZAB performance; see **Figure 10(iii)**.<sup>119</sup> It has also

been revealed that the synergistic coupling effect between CoP and CoO could enrich the active sites and lower the energy barrier for adsorption of reaction intermediate species in a bifunctional CoP/CoO@MNC-CNT electrocatalyst.<sup>199</sup>

## 5. Core-shell heterostructures for ORR/OER and ZABs

Recently, numerous bifunctional core-shell heterostructured catalysts with a range of material features, including a hollow core-shell porous structure, metal-metal core-shell structure, and metal-carbon core-shell structure, have been produced to enhance bifunctional reactions and ZAB performance.<sup>33, 200-202</sup> In addition to the size and shape of the nanoparticles, the method of manufacturing has a major effect on the final material properties.

### 5.1 Metal-Carbon core-shell heterostructures for ORR/OER and ZABs

The primary approach for enhancing catalytic performance and safeguarding the metal-core against corrosion involves constructing a metal-carbon core-shell heterostructure using carbon materials.<sup>203-205</sup> This can be achieved by forming heterointerfaces and exploiting the protective properties of the carbon shell. For example, Yu et al.<sup>206</sup> reported that the core-shell structure of N-doped graphitic carbon-coated Co nanoparticles (Co@NrC) can optimize the oxygen adsorption/dissociation. In addition, the optimal compositional and core-shell architectural features revealed excellent electronic conductivity, regulated electronic configuration, rich defects, and a greater number of exposed active sites to provide enhanced charge transport for ORR and OER. As a consequence, the Co@NrC-0.3 system showed higher onset and halfwave potentials ( $E_{\text{onset}}=0.97 \text{ V vs. RHE}$ ;  $E_{1/2}=0.85 \text{ V vs. RHE}$ ) compared to other Co@NrC catalysts (Co@NrC-0.6:  $E_{\text{onset}}=0.91 \text{ V vs. RHE}$ ;  $E_{1/2}=0.81 \text{ V vs. RHE}$ ; Co@NrC-0.45:  $E_{\text{onset}}=0.92 \text{ V vs. RHE}$ ;  $E_{1/2}=0.81 \text{ V vs. RHE}$ ; Co@NrC-0.15:  $E_{\text{onset}}=0.97 \text{ V vs. RHE}$ ;  $E_{1/2}=0.85 \text{ V vs. RHE}$ ); this was almost similar to commercial Pt/C ( $E_{\text{onset}}=0.99 \text{ V vs. RHE}$ ;

RHE,  $E_{1/2} = 0.85\text{V}$  vs. RHE). In addition, during OER, the Co@NrC-0.3 sample required a small overpotential of  $\sim 386$  mV to reach  $10 \text{ mA cm}^{-2}$ ; this was higher than other Co@NrC materials (Co@NrC-0.6:  $\sim 407$  mV; Co@NrC-0.45:  $\sim 406$  mV; Co@NrC-0.15:  $\sim 466$  mV) and commercial RuO<sub>2</sub> ( $\sim 440$  mV). Notably, the Co@NrC-0.3 exhibited excellent bifunctional activity with a  $\Delta E$  of  $\sim 0.766$  V. In addition, a Co@NrC-0.3-based ZAB demonstrated a larger open-circuit voltage of  $\sim 1.47$  V compared to a Pt/C+RuO<sub>2</sub>-based ZAB ( $\sim 1.44$  V). Xu et al.<sup>207</sup> identified that FeCo core-shell carbon particles embedded on porous nitrogen-doped carbon-nanosheets (FeCo/NUCSs) can facilitate the co-existence of Fe-N<sub>x</sub> and Co-N<sub>x</sub> active sites, which increase ORR activity. As a result, the FeCo/NUCSs showed a high  $E_{1/2}$  value of  $\sim 0.89$  V vs. RHE, higher than pristine FeCo-NPs ( $\sim 0.835$  V vs. RHE) and NUCSs ( $\sim 0.815$  V vs. RHE). In addition, the nitrogen-doped carbon-nanosheets (NUCSs) can enhance the number of catalytic active sites on the surface of the carbon by facilitating electron transport from the FeCo alloy to carbon, while the catalytic active sites Fe-N<sub>x</sub> and Co-N<sub>x</sub> can change charge distribution across the carbon layer. Moreover, catalytic FeOOH/CoOOH species are produced on the FeCo alloy during electrocatalysis that can act as OER active sites. Remarkably, the FeCo/NUCSs exhibited an OER overpotential of  $\sim 310$  mV at  $10 \text{ mA cm}^{-2}$ ; this was lower than FeCo-NPs ( $\sim 440$  mV), Co/NUCSs ( $\sim 450$  mV), Fe/NUCSs ( $\sim 480$  mV), NUCSs ( $\sim 750$  mV) and RuO<sub>2</sub> ( $\sim 390$  mV). As a consequence, the FeCo/NUCSs based ZAB exhibited a higher open circuit voltage ( $\sim 1.51$  V) compared to a Pt/C+RuO<sub>2</sub> based ZAB ( $\sim 1.47$  V). In addition, the FeCo/NUCSs based ZAB showed a maximum power density of  $\sim 152.38 \text{ mW cm}^{-2}$  at  $207.16 \text{ mA cm}^{-2}$ , which was higher than that of Pt/C+RuO<sub>2</sub> based ZAB ( $\sim 113.81 \text{ mW cm}^{-2}$ ). The FeCo/NUCSs based ZAB was also stably cycled over 100 h.

Chen et al.<sup>208</sup> observed that, due to the introduction of defects and multiple activity centers formed by the core-shell heterostructure of nitrogen-doped carbon encapsulated

$\text{FeNi}_3$  ( $\text{FeNi}_3@\text{NC}$ ), there was an increase in the bifunctional electrocatalytic activity. Due to the different polarity between the FeCo alloy components in the N-doped carbon ( $\text{FeCoNC/D}$ ), the reaction energy barrier was lowered when the FeCo alloy nanoparticles were uniformly dispersed, which led to an internal electron redistribution; see **Figure 11(i)**.<sup>209</sup> Meanwhile, the strong bond between the core of the alloy nanoparticle and the N-doped carbon shell prevents the metal from corrosion during the electrocatalytic process. Zhao et al.<sup>210</sup> reported that the use of alloying and sulfurization techniques could be an effective strategy for enhancing the number of exposed catalytic active sites within the catalyst. This includes cobalt or cobalt ferroalloy sulfides, along with their heterojunctions, core-shell structure, and S, N-doped carbon/carbon nanotube ( $\text{CoFe-S@3D-S-NCNT}$ ) electrocatalysts. Consequently, this strategy results in a simultaneous improvement in the catalytic activity for ORR and OER, while minimizing the potential gap ( $\Delta E$ ) to 0.71 V. As a result, liquid ZABs made from a  $\text{CoFe-S@3D-S-NCNT}$  electrocatalyst exhibited a high peak power density of  $223 \text{ mW cm}^{-2}$ , a superior specific capacity of  $815 \text{ mA h gZn}^{-1}$ , and exceptional stability for almost 900 hours at a current density of  $5 \text{ mA cm}^{-2}$ . In addition, the quasi-solid-state zinc-air batteries (ZABs) demonstrate a high peak power density of  $490 \text{ mW cm}^{-2}$  and an excellent voltage round-trip efficiency of 64%. Choi et al.<sup>57</sup> reported that Co nanoparticles-encapsulated in holey N-doped carbon nanotubes ( $\text{Co@H-NCNT}$ ) could provide a greater number of Co/N-C moieties. Notably, the  $\text{Co@H-NCNT}$  microstructure formation was effective in having high catalytic activity and stability toward ORR, OER, and ZAB performance (**Figure 11(ii)**). In addition, due to the core-shell features, the MOF-derived CoP-nitrogen-doped carbon@NiFeP ( $\text{CoP-NC@NFP}$ ) nanoflakes electrocatalyst exhibited an excellent bifunctional electrocatalytic activity, along with good stability and ZAB performance; see **Figure 11(iii)**.<sup>211</sup>

## 5.2 Metal-Metal core-shell heterostructures for ORR/OER and ZABs

Recent investigations have shown that metal-metal core-shell structured nanomaterials with tailored chemical and physical properties, in both the cores and shells, can act as powerful platforms for bifunctional electrocatalysis.<sup>212, 213</sup> In such metal-metal core-shell heterostructures, the lattice mismatch and deficiency of chemical interaction between metals (or metal oxides or sulfides or phosphides) often results in a large interfacial energy, which could lead to strain-rich and defect-rich features, and an edge-terminated environment, thereby increasing the number of exposed active sites for adsorption and desorption of oxygen reactants and increasing the electronic conductivity for facile charge transport.<sup>10, 12, 39, 212, 213</sup> As shown in **Figure 12(i)**, a layer of 1T Co-WS<sub>2</sub> shell-nanochannels at the NiTe<sub>2</sub>/Ni metallic core–nanoskeleton sheet can provide high electrocatalytic activity in terms of  $\eta_{OER}$  of 290 mV @ 30 mA cm<sup>-2</sup> and E<sub>1/2</sub> of 0.781 V for ORR. It was predicted that the interfacial heterojunction of 1T Co-WS<sub>2</sub>/NiTe<sub>2</sub>/Ni may exhibit outstanding electrochemical performance.<sup>214</sup> In addition, the high electrocatalytic bifunctional activity of NiPS<sub>3</sub> nanosheets was achieved by their unusual core-shell heterostructure with NiOOH (ie., NiPS<sub>3</sub>@NiOOH core-shell heterostructure), where the presence of P and S modulates the surface electronic state of nickel and their high density of exposed active metallic-edge sites assisted in improving water oxidation. It was predicted that, during an OER, electron-transport to the NiOOH shell would be facilitated by the metallic edge sites of the NiPS<sub>3</sub> core.<sup>215</sup> In addition, due to an improved electronic conductivity with a greater number of exposed active sites, the metallic Ni core and Fe-doped NiCo alloy shell on carbon nanotubes (Fe/Ni@NiCo-CNT) exhibited superior ORR and OER activities. As a result, the Fe/Ni@NiCo-CNT Zn-air batteries (ZABs) showed a high specific capacity of ~796.5 mA h gZn<sup>-1</sup> and an excellent open circuit potential of 1.427 V.<sup>216</sup> Yan et al.<sup>217</sup> reported

that in a  $\text{MoS}_2@\text{FeN-C}$  NSs core-shell heterostructure, the core-shell of Fe-N-C shields the  $\text{MoS}_2$  core from the corrosive effects of the alkaline electrolyte during the ORR and OER reactions, thereby ensuring the as-built ZABs demonstrate high durability. As a consequence, when repeatedly charged and discharged for 22 h at a high current density of  $10 \text{ mA cm}^{-2}$ , the ZAB based on  $\text{MoS}_2@\text{Fe-N-C}$  NSs showed a high level of cycling stability. In addition, for a Co core@Co oxide shell ( $\text{Co}@\text{CoO}_x$ ) catalyst, the surface of the Co oxide was observed to be more electron enriched.<sup>218</sup> This heterostructure effect and modification of charge conductivity, oxygen affinity, and intermediate transfer channel make the metal@metal oxide catalyst a potential candidate for ORR and OER. Notably, the aqueous ZAB based on  $\text{Co}@\text{CoO}_x$  showed a high specific capacity of  $\sim 694 \text{ mAh g}_{\text{Zn}}^{-1}$  with excellent performance retention after a durability test. Pan et al.<sup>219</sup> prepared the heterostructure of amino-functionalized CNTs with  $\text{CoNi}@\text{CoO-NiO}$  ( $\text{CoNi}@\text{CoO-NiO/NH}_2\text{-CNTs}$ ) core/shell structure by hydrothermal method followed by calcination. Notably, the bifunctional catalysis performance is significantly enhanced by a synergy between the bimetallic CoNi alloy and its corresponding oxides. As a consequence, the  $\text{CoNi}@\text{CoOeNiO/NH}_2\text{-CNT-3}$  catalyst exhibited an excellent  $E_{1/2}$  value of  $\sim 0.794 \text{ V vs. RHE}$  and a low OER potential of  $\sim 1.607 \text{ V vs. RHE}$  at  $10 \text{ mA cm}^{-2}$ . Interestingly, the  $\text{CoNi}@\text{CoOeNiO/NH}_2\text{-CNTs-3}$  based rechargeable ZAB provided a high power density of  $\sim 128.7 \text{ mWcm}^{-2}$ ; this was higher than that of  $\text{Pt/CeRuO}_2$  ( $\sim 88.1 \text{ mW cm}^{-2}$ ). Furthermore, the  $\text{CoNi}@\text{CoOeNiO/NH}_2\text{-CNTs-3}$  based ZAB exhibited a high open circuit voltage (OCV) of  $\sim 1.458 \text{ V}$  and the discharge voltage was  $\sim 1.40 \text{ V}$  at  $10 \text{ mA cm}^{-2}$ . In addition, due to the small core@shell  $\text{CoS}_x@\text{Cu}_2\text{MoS}_4$  hybrids in a  $\text{CoS}_x@\text{Cu}_2\text{MoS}_4\text{-MoS}_2/\text{NSG}$  heterostructured catalyst, the formation of a core-shell structure could lead to defect-rich features with a more edge terminated nature and an increase in the number of

exposed active sites for adsorption and desorption of oxygen reactants and an increase in electronic conductivity for facile charge transport; see **Figure 12(ii)**.<sup>220</sup> A ZAB based on CoS<sub>x</sub>@Cu<sub>2</sub>MoS<sub>4</sub>-MoS<sub>2</sub>/NSG heterostructure exhibited an open-circuit voltage of ~1.44 V and a maximum power density of ~40 mW cm<sup>-2</sup> at 58 mA cm<sup>-2</sup>, which was higher than Pt/C-based ZAB (~32 mW cm<sup>-2</sup> at 50 mA cm<sup>-2</sup>).

### 5.3 Hollow core-shell heterostructures for ORR/OER and ZABs

The energy conversion and storage applications of core-shell materials are increasing due to their multifunctional nature that can be achieved by forming several shells and manipulating the core-shell materials and structure.<sup>33, 221, 222</sup> Furthermore, the removal of the inner core from core-shell structures presents a unique opportunity to create multipurpose hollow core architectures with large electrochemically active surface area, more exposed active sites, improved charge and mass transfer rates, and interfaces with optimal electronic properties.<sup>222-224</sup> In this regard, a hollow yolk@shell Co<sub>3</sub>O<sub>4</sub>/HNCP-40 structure demonstrated excellent performance for the ORR and OER reactions, due to several advantageous factors.<sup>225</sup> These include the presence of more oxygen vacancies and tetrahedral Co<sup>2+</sup> ions, which contribute to enhanced catalytic ORR activity. Furthermore, the hollow yolk-shell interfacial structure facilitated efficient mass transfer, leading to improved catalytic activity. As a result, the hollow yolk@shell Co<sub>3</sub>O<sub>4</sub>/HNCP-40 catalyst exhibited similar catalytic activity to Pt/C for the oxygen reduction reaction (ORR) with an excellent  $E_{1/2}$  value of ~0.834 V vs. RHE and also exhibited an enhanced stability and methanol tolerance compared to Pt/C. In addition, the CoO<sub>x</sub> species and nitrogen-doped carbon in the structure exhibited potential synergistic effects of the optimal yolk@shell Co<sub>3</sub>O<sub>4</sub>/HNCP-40 catalyst; this resulted in the enhancement of OER performance by a low overpotential of ~333 mV at 10 mA cm<sup>-2</sup> and a small Tafel slope of ~69 mV dec<sup>-1</sup>. Notably, these values surpass an IrO<sub>2</sub>

catalyst ( $\sim 409$  mV at  $10$  mA  $\text{cm}^{-2}$ ). In addition, the catalyst has similar catalytic activity for the oxygen reduction reaction (ORR), while exhibiting improved stability and methanol tolerance compared to commercially available Pt/C (20 wt %). These findings suggest that the catalyst has the potential to serve as a bifunctional electrocatalyst for both the OER and ORR. Wang et al.<sup>226</sup> reported that in a porous Ni-Fe-S/xNCQDs hollow nanocage heterostructure, the higher oxygen reduction reaction (ORR) activity can be attributed to the intrinsic heterostructure properties of FeS/NiS and nitrogen doped carbon quantum dots (NCQDs), which resulted in an increased adsorption affinity for  $\text{O}_2$ ; see **Figure 13 (i)**. In addition, the superior mass-transfer was facilitated by the presence of a hollow nanocage structure. The coupling and interaction between the nickel oxyhydroxide (NiOOH) and iron oxyhydroxide (FeOOH) significantly enhanced the process of charge transfer and catalytic performance for oxygen evolution reaction (OER). The porous hollow features can also improve the rate of mass transfer and promote the exposure of a larger number of active sites (ORR/OER) on the surface of Ni-Fe-S/3NCQDs, thereby resulting in a promising bifunctional activity ( $\Delta E \sim 0.675$  V). In addition, the cage structure of the material can prevent the active species from aggregating, thereby ensuring long-term stability. As a result of these features, the Ni-Fe-S/3NCQDs-based ZAB showed an open-circuit voltage and maximum power density of  $\sim 1.389$  V and  $94$  mW  $\text{cm}^{-2}$ , respectively. When a cyclic test was performed at  $\sim 10.0$  mA  $\text{cm}^{-2}$  for  $1700$  h (40 min per cycle), the initial discharge and charge voltages were  $\sim 1.19$  and  $2.11$  V, respectively, where the voltage gaps were  $\sim 0.92$  V and  $\sim 56.3\%$  of the round-trip efficiency was achieved. Following 360 cycles of discharge and recharge, there was a small rise in the voltage gap ( $\sim 1.27$  V) and a slight decrease in the energy efficiency ( $\sim 44.4\%$ ). In addition, the modulated Fe-*d* band center of the Fe-N<sub>4</sub> sites in a NiFe-LDH/Fe<sub>1</sub>-N-C hollow nanorod heterostructure can significantly

reduce the energy barriers of the ORR rate-limiting steps, while the NiFe-layered double hydroxide (NiFe-LDH) nanodots could provide active sites for OER.<sup>227</sup> As a result, the optimal NiFe-LDH/Fe<sub>1</sub>-N-C hollow nanorod heterostructured catalysts showed an excellent outstanding bifunctional activity with a small  $\Delta E$  of ~0.65 V. The ZABs made using NiFe-LDH/Fe<sub>1</sub>-N-C catalyst exhibited a peak power density of ~205 mW cm<sup>-2</sup> and long-term cycling stability of up to 400 h. Furthermore, dual-sided Fe/Fe<sub>3</sub>C@N-doped carbon nanotubes (FNCHFs) containing hierarchical hollow frameworks exhibited excellent electrochemical activity and ZAB performance through the regulated electronic conductivity and more exposed active sites.<sup>228</sup> Due to the synergistic effect between S-dopant and CoFe-N-C active sites in the Fe and Co atoms impregnated N, the S-co-doped hollow carbon spheres (CoFe-SNC) can improve the intrinsic bifunctional electrocatalytic activity, accelerate the reaction kinetics, and enhance ZAB.<sup>95</sup> Moreover, a unique linked nano-spheroidal structure of CuSA@HNCN<sub>x</sub> provided more active sites and increased accessibility of reactive species.<sup>229</sup> As shown in **Figure 13 (ii)**, due to its hollow structural features, the Janus-structured Ni-SAs/HCNFs/Co-NAs exhibited a remarkable bifunctional catalytic activity with a low  $\Delta E$  value of ~0.65 V.<sup>101</sup> Notably, the Ni-As/HCNFs/Co-NAs-based ZAB showed high open-circuit potential, and high specific capacity of ~1.45 V and 808 mAh g<sup>-1</sup> Zn, respectively; it is also possessed excellent long life over 200 h at 10 mA cm<sup>-2</sup>. Due to the formation of Mott–Schottky heterojunction, the oxygen defects-rich CoFe/CoFe<sub>2</sub>O<sub>4</sub> on hollow N-doped carbon sphere (Vo-CoFe/CoFe<sub>2</sub>O<sub>4</sub>@NC) showed an excellent  $E_{1/2}$  value of ~0.858 V vs. RHE, while the high limiting current of ~5.98 mA cm<sup>-2</sup> at 0.5 V was achieved, see **Figure 13 (iii)**.<sup>230</sup> Remarkably, the current density for Vo-CoFe/CoFe<sub>2</sub>O<sub>4</sub>@NC was similar (~98.3%) after a 100 h stability test. In addition, the VoCoFe/CoFe<sub>2</sub>O<sub>4</sub>@NC required a lower OER potential of ~360 mV to

reach  $10 \text{ mA cm}^{-2}$ . With a current density of  $\sim 155.2 \text{ mA cm}^{-2}$  at  $0.8 \text{ V}$  and a peak power density of  $\sim 138.5 \text{ mW cm}^{-2}$  at  $230.2 \text{ mA cm}^{-2}$ , the  $\text{Vo-CoFe/CoFe}_2\text{O}_4@\text{NC}$ -based ZAB was more effective than the  $\text{Pt/C+RuO}_2$ -based ZAB ( $\sim 135.2 \text{ mA cm}^{-2}$  at  $0.8 \text{ V}$  and  $\sim 121.6 \text{ mW cm}^{-2}$  at  $207.2 \text{ mA cm}^{-2}$ ). The  $\text{Vo-CoFe/CoFe}_2\text{O}_4@\text{NC}$ -based ZAB had an initial voltaic energy efficiency of  $\sim 63\%$ , calculated by dividing the discharge voltage by the charge voltage.

## 6. Density Functional Theory Calculations

Computational catalysis has emerged as an effective method for analyzing, understanding, and even predicting the activity and selectivity of various catalytic materials.<sup>231-233</sup> The results of computational studies are utilized to rationally design materials that are more catalytically active. This approach reveals novel catalysts that might be further tested experimentally. Particularly, density functional theory (DFT)-based methods have shown to be essential for understanding the mechanistic details of catalytic features and properties to be tackled, such as identification of active catalytic species, adsorption energies of intermediates, activation energy barriers (*i.e.*, transition states), and electronic structure information which are difficult to investigate through experimental methods because of their high instability at the atomic scale.<sup>233-235</sup> Theoretical research on electrocatalytic oxygen reactions (ORR and OER) has shown that the free energy of the intermediates (\*O, \*OH, and \*OOH) on the catalyst surface strongly influences the reaction activity.<sup>232, 236</sup> Besides, the catalytic activity is significantly influenced by the nature of the catalyst surface, as the adsorption energies of the reaction intermediates are subject to variation. Rather than simply combining several materials with different levels of superiority, a heterostructured catalyst offers several advantages, and the microstructure of heterointerfaces is closely associated with the distinctive advantages of the heterostructure.<sup>236-238</sup> When two building blocks

developed into contact, band alignments may occur at heterointerface, causing charge redistribution around the interfaces.<sup>239</sup> While the Fermi levels ( $E_f$ ) of these materials eventually approach equilibrium. Consequently, a built-in potential is formed as the holes and electrons accumulate near the heterointerface and are separated by a completely ionized depletion area. This built-in potential makes heterostructured materials as highly conductive in forward bias and nearly insulated in reverse bias.<sup>238</sup> Remarkably, the holes and electrons accumulated near the heterointerface may easily adsorb the opposite charge carriers, which can act as active sites for electrocatalytic reactions.<sup>109</sup>

As shown in **Figure 14(i)**, hybridization of NiCoP with NiO may induce a strong synergistic electronic coupling effect.<sup>240</sup> Notably, by giving 0.3420 e<sup>-</sup> to the NiCoP, NiO acts as an electron donor. These findings indicate that the heterojunction of NiCoP/NiO interfaces may result in an inhomogeneous electron aggregation, enriched bonding, and facile regulation of catalytic reactions, and thus enhances the reaction kinetics of bifunctional oxygen reactions. Also, the density of states calculation (DOS) indicates that, in comparison to NiO, NiO with the oxygen vacancy exhibits metallic properties and the charge carrier increases the density at the Fermi level, signifying that the O vacancy structure promotes fast electron transfer because it has no band gap and is nearer to the  $E_f$ . Also, the formation of CoP<sub>3</sub>/CeO<sub>2</sub> heterojunction in 3D flower-like CoP<sub>3</sub>/CeO<sub>2</sub>/C heterostructure may modify the distribution of charges at the interface, lower the energy barriers for electrocatalytic processes, and produce an enhanced electronic environment for OER and ORR.<sup>241</sup> The CoS<sub>2</sub>/Cu<sub>2</sub>S heterostructured catalyst catalyzing the oxygen reaction had the lowest reaction energy barrier than CoS<sub>2</sub> and Cu<sub>2</sub>S, indicating that the strong electronic interaction between CoS<sub>2</sub> and Cu<sub>2</sub>S in a CoS<sub>2</sub>/Cu<sub>2</sub>S heterostructure could increase conversion step.<sup>159</sup> Also, compared to CoS<sub>2</sub>,

and Cu<sub>2</sub>S, the DOS of CoS<sub>2</sub>/Cu<sub>2</sub>S heterostructure exhibited an electron delocalization nature. As a result, the CoS<sub>2</sub>/Cu<sub>2</sub>S heterostructure required an energy of ~0.644 eV for the third step, which is the rate-determining step in the ORR process, which was lower than that of CoS<sub>2</sub> (~0.656 eV, from \*OH to \*O) and Cu<sub>2</sub>S (~0.660 eV, from \*+O<sub>2</sub> to \*OOH). In the OER, the conversion of \*OH and \*O was the crucial step between CoS<sub>2</sub>/Cu<sub>2</sub>S and Cu<sub>2</sub>S, with free energy differences of ~1.311 eV and ~1.391 eV, respectively. Recently Yao et al.<sup>38</sup> proposed that in a Fe<sub>3</sub>N-FeN<sub>0.0324</sub> heterojunction, the electron-rich FeN<sub>0.0324</sub> will be an active site for ORR, where the electrons (e<sup>-</sup>) can be easily transported from the surface of FeN<sub>0.0324</sub> to the adsorbed oxygen-related intermediates, creating a negative charge center for proton (H<sup>+</sup>) to attack, thus significantly accelerating the ORR kinetics (**Figure 14(ii)**). Besides, the hole-rich Fe<sub>3</sub>N could be an active site for OER, subsequently the h<sup>+</sup> may transfer from the surface of catalyst to the adsorbed OH group intermediates, and thus encouraging the deprotonation process. As a result, the electron-/hole-rich center in Fe<sub>3</sub>N-FeN<sub>0.0324</sub> heterojunction showed excellent bifunctional oxygen reaction kinetics.

Also, Hammer and Nørskov developed the d-band hypothesis to describe the electronic structure of adsorbates on metal surfaces.<sup>242, 243</sup> In oxygen electrocatalysis, various oxygen intermediates including O\*, OH\*, OOH\*, and OO\* interact on the catalyst surface to create adsorbed oxygenated species.<sup>20, 243</sup> The localized d-band center mostly regulates the bonding strengths of the adsorption species on the surface of the catalyst. When a bond is formed between metal d-orbitals and oxygen p-orbitals, two states are created, namely the filled bonding state and the partially occupied antibonding state. The d-band center theory states that the adsorption energy of a particular species on a metal surface is influenced by the position of the d-band center (E<sub>d</sub>) relative to the Fermi level (E<sub>f</sub>).<sup>31, 45</sup> Therefore, the energy level of the d-band center (E<sub>d</sub>) directly influences the

number of electrons occupying the antibonding orbital, thereby affecting the strength and stability of the adsorption bond. Additionally, a downshift in the energy state of the d-band center ( $E_d$ ) can improve the desorption capacity of the oxygen-containing intermediates on the surface of the catalyst (owing to a weaker metal–adsorbate bond), hence accelerating the ORR/OER reaction rate. Therefore, the d-band center can be employed as an activity descriptor because this model allows a basic correlation between surface electronic features and catalytic activity with reliable consistency.<sup>244</sup> Recently, it was suggested that a d-band center model based on DFT simulation, could be used to effectively control the electronic structure of cobalt or Iron nanoclusters coupled heterointerfaces.<sup>31, 238, 245</sup> For example, in a Ni<sub>3</sub>FeN/VN heterostructure, after forming the interface of the Ni<sub>3</sub>FeN/VN heterojunction, a small downshift in  $E_d$  has been observed for V 3d and Ni 3d states (see **Figure 14(iii)**).<sup>246</sup> Whereas a slight upshifting to be near to  $E_f$  was observed for the  $E_d$  of Fe 3d, displaying an improved electron occupied Fe 3d states near  $E_f$  and enhancing the electron transfer. The d-band theory states that reducing  $E_d$  to the Fermi level increases the binding strength between reactants and active sites, facilitating the adsorption of reactive molecules. Conversely, it may lead to a weak binding strength, which would make a facile desorption of the reaction intermediate product, hence accelerating the ORR/OER reaction rate.

In addition, several other approaches including multisite adsorption strategies,<sup>247</sup> doping schemes,<sup>157</sup> multiple descriptors,<sup>248</sup> and strain schemes,<sup>249</sup> have been executed for the development of novel heterostructured bifunctional oxygen electrocatalysts with outstanding performance. However, it may be challenging to regulate the adsorption free energies to the appropriate ranges when trying to enhance the efficiency of heterostructured electrocatalysts in experiments. To further rationally design electrocatalysts, it is also important to carefully choose physically feasible descriptors

such as electronic descriptors (d and/or p electrons), geometrical descriptors (coordination environment), activity descriptors (electron affinity, electronegativity, and first ionization energy), and composite descriptors (bond length and electronegativity of neighboring atoms).

## 7. Challenges and Future Perspectives

Recent research has revealed that a range of non-precious metal heterostructured catalysts have provided significant advancements in terms of design, processing, and performance, see **Scheme 3**. Due to their unique interfacial topology, highly exposed active sites, and electrically conductive nature, such catalysts have been employed as electrocatalysts, in particular for improving oxygen reduction and evolution reactions (ORR/OER). Notably, rechargeable zinc-air batteries (ZABs) can benefit greatly from the use of heterostructured electrocatalysts to improve bifunctional oxygen reactions (ORR/OER) since they are low-cost, effective, durable, and environmentally friendly.

In addition, inspired by the advantageous characteristics of the variety of architectures formed, the electrocatalytic performance can be efficiently optimized through the integration of a diverse range of nanostructures. To better understand how to improve the electrochemical performance of rechargeable ZABs, we have surveyed in detail recently developed approaches to regulate heterointerfaces and have focused on several key parameters; these include a synergistic coupling of the different constituents, defect/strain engineering, surface engineering, incorporation of metal-free or precious or non-precious metal heteroatoms, the formation of a range tailored heterostructures, electrocatalyst reaction adsorption, enhancing the electrical conductivity, active sites engineering, increasing the reaction surface area, decreasing the reaction energy barrier, and improving electron and mass transfer. Judicious control of interfacial electronic effects such as electronic charge redistribution, chemical bonding at the interface, and

lattice strain effects can optimize the electronic structure and modulate the chemisorption of diffusion/transportation behaviour of reaction intermediates during the ORR and OER. Tailoring such characteristics can improve the reaction kinetics for the ORR/OER to achieve high electrocatalytic performance for rechargeable ZABs.

Despite their promising performance and wide-ranging potential application, these heterostructured materials require further development for widespread industrial-level ZAB implementation. Typically, the surface and interface engineering of air electrodes and electrocatalysts is crucial for rechargeable Zn–air batteries (ZABs) due to the complex triple-phase gas–solid–liquid reaction environment. Since several catalysts have a high potential difference ( $\Delta E$ ), this indicates that additional effort needs to be made to improve their efficiency. Limited research to date has been made regarding heterostructured electrocatalysts, despite the fact that their long-term durability makes them of particular interest in enabling practical applications; there is therefore a need for substantial bifunctional catalytic current densities at low potentials. In addition, the interfacial bonding and active surface areas critically depend on the chemistry, structure, and mismatch stresses involved in the heterostructures. As a result, the commercialization of ZABs would benefit greatly from efforts in the optimization of structural configuration, improvement in reaction kinetics, and optimal loading of constituents. The primary limitation of heterostructures is the large number of defects induced by lattice mismatches, and typically the formation of a large amount of defects can result in a decrease in the bifunctional electrocatalytic activity and ZAB device performance. In addition, depending on the thickness of the layers and the degree of stress, the heterointerface can be relaxed by creating undesired defects and dislocations, and these defects often result in inferior functionality. Therefore, optimization and regulation of defects and strain is an area worthy of further investigation. Similarly,

further investigations into the reaction mechanism of heterostructures in the context of electrocatalysis are required, in particular for the OER, due to the growing complexity of catalyst components. In an effort to monitor structural reconstruction through real-time examinations and identify active sites for targeted reactions, advanced characterization techniques such as in-situ Raman, TEM, and XANES spectroscopy are essential. This will aid in the design of more efficient bifunctional heterostructures for electrocatalytic reactions by understanding the reaction kinetics and thermodynamics and screening the structure–performance relationship of interfacially modified catalysts. The OER and ORR reactions have relevance to the recharging and discharging processes of rechargeable ZABs and, due to the contrasting reaction requirements and complex multi-electron reaction processes, there remains a gap between the ORR and OER for single heterostructure catalysts. This difference renders a significant number of electrocatalysts unsuitable for use in rechargeable zinc-air battery applications. Thus, it is essential to narrow the gap in the potential difference between the ORR and OER, where the power density, round-trip efficiency, and lifetime of rechargeable ZABs are directly influenced by both ORR and OER on the air electrodes. It is of particular interest that common alkaline electrolytes can create insoluble zinc oxide precipitates and/or zinc dendrites from zinc ions and membrane disintegration. Alkaline solutions can quickly disintegrate the air electrode polymer binder, leading to the loss of active material and high interfacial impedance, which increases the cell overpotential. To solve the alkaline electrolyte problem, alternate electrolytes must therefore be developed. However, integrating multiscale heterointerfacial architectures remains a challenge, where the inherent activity of many micro-scale interfacial regulatory approaches leads to a decrease in performance due to unavoidable obscuring of active site. Thus, the development of high-performance ORR and OER electrocatalysts for

ZABs requires a coordinated multiscale heterointerfacial regulation. Besides, single-cathode and dual cathode zinc-air batteries are also of great interest to enhance the performance. Finally, it may be possible to achieve improved electrochemical performance by precise control of the interface at the micro/atomic level that can only be realized through a combination of theoretical and experimental research that can provide new insights into interface effects. Effort in these directions provides potential to improve the bifunctional ORR/OER electrocatalytic activity and thereby induce the ZAB performance in large-scale applications

### Acknowledgments

This work was supported by the National Natural Science Foundation of China (22262010, 22062005, 22165005, U20A20128), Guangxi Science and Technology Fund for Distinguished High-Talent Introduction Program (AC22035091), Guangxi Science Fund for Distinguished Young Scholars (2019GXNSFFA245016).

### References

- [1] Shinde, S. S.;Jung, J. Y.;Wagh, N. K.;Lee, C. H.;Kim, D.-H.;Kim, S.-H.;Lee, S. U.; Lee, J.-H. Ampere-hour-scale zinc–air pouch cells. *Nat. Energy* **2021**, *6*, 592-604. DOI: <https://doi.org/10.1038/s41893-022-01028-x>.
- [2] Hu, E.; Yang, X.-Q. Rejuvenating zinc batteries. *Nat. Mater.* **2018**, *17*, 480-481. DOI: <https://doi.org/10.1038/s41563-018-0090-9>.
- [3] Sun, W.;Wang, F.;Zhang, B.;Zhang, M.;Küpers, V.;Ji, X.;Theile, C.;Bieker, P.;Xu, K.;Wang, C.; Winter, M. A rechargeable zinc-air battery based on zinc peroxide chemistry. *Science* **2021**, *371*, 46-51. DOI: [doi:10.1126/science.abb9554](https://doi.org/10.1126/science.abb9554).
- [4] Yang, D.;Tan, H.;Rui, X.; Yu, Y. Electrode materials for rechargeable zinc-ion and zinc-air batteries: current status and future perspectives. *Electrochem. Energy Rev.* **2019**, *2*, 395-427. DOI: <https://doi.org/10.1007/s41918-019-00035-5>.
- [5] Liu, J.;Chen, W.;Yuan, S.;Liu, T.; Wang, Q. High-coordination Fe–N4SP single-atom catalysts via the multi-shell synergistic effect for the enhanced

- oxygen reduction reaction of rechargeable Zn–air battery cathodes. *Energy Environ. Sci.* **2024**, *17*, 249–259. DOI: 10.1039/d3ee03183g.
- [6] Sun, Q.;Dai, L.;Luo, T.;Wang, L.;Liang, F.; Liu, S. Recent advances in solid-state metal–air batteries. *Carbon Energy* **2023**, *5*, e276. DOI:<https://doi.org/10.1002/cey2.276>.
- [7] Yang, C.;Xia, J.;Cui, C.;Pollard, T. P.;Vatamanu, J.;Faraone, A.;Dura, J. A.;Tyagi, M.;Kattan, A.; Thimsen, E. All-temperature zinc batteries with high-entropy aqueous electrolyte. *Nat. Sustain.* **2023**, *6* (3), 325–335. DOI: <https://doi.org/10.1038/s41893-022-01028-x>
- [8] Sun, W.;Küpers, V.;Wang, F.;Bieker, P.; Winter, M. A Non-Alkaline Electrolyte for Electrically Rechargeable Zinc-Air Batteries with Long-Term Operation Stability in Ambient Air. *Angew. Chem. Int. Ed.* **2022**, *134* (38), e202207353. DOI: <https://doi.org/10.1002/anie.202207353>
- [9] Li, L.;Cao, Q.;Wu, Y.;Zheng, Y.;Tang, H.;Ge, J.;Liang, M.;Zhou, B.;Jiang, B.; Wu, S. Wood-Derived Continuously Oriented Three-Phase Interfacial Channels for High-Performance Quasi-Solid-State Alkaline Zinc Batteries. *Adv. Mater.* **2023**, 2300132. DOI: <https://doi.org/10.1002/adma.202300132>.
- [10] Jiang, Y.;Deng, Y.-P.;Liang, R.;Fu, J.;Gao, R.;Luo, D.;Bai, Z.;Hu, Y.;Yu, A.; Chen, Z. d-Orbital steered active sites through ligand editing on heterometal imidazole frameworks for rechargeable zinc-air battery. *Nat. Commun.* **2020**, *11* (1), 5858. DOI: <https://doi.org/10.1038/s41467-020-19709-6>
- [11] Chandrasekaran, S.;Khandelwal, M.;Dayong, F.;Sui, L.;Chung, J. S.;Misra, R.;Yin, P.;Kim, E. J.;Kim, W.; Vanchiappan, A. Developments and Perspectives on Robust Nano-and Microstructured Binder-Free Electrodes for Bifunctional Water Electrolysis and Beyond. *Adv. Energy Mater.* **2022**, *12* (23), 2200409. DOI: <https://doi.org/10.1002/aenm.202200409>
- [12] Chandrasekaran, S.;Ma, D.;Ge, Y.;Deng, L.;Bowen, C.;Roscow, J.;Zhang, Y.;Lin, Z.;Misra, R. D. K.;Li, J.;Zhang, P.; Zhang, H. Electronic structure engineering on two-dimensional (2D) electrocatalytic materials for oxygen reduction, oxygen evolution, and hydrogen evolution reactions. *Nano Energy* **2020**, *77*, 105080. DOI: <https://doi.org/10.1016/j.nanoen.2020.105080>.
- [13] Li, L.;Tsang, Y. C. A.;Xiao, D.;Zhu, G.;Zhi, C.; Chen, Q. Phase-transition tailored nanoporous zinc metal electrodes for rechargeable alkaline zinc-nickel

- oxide hydroxide and zinc-air batteries. *Nat. Commun.* **2022**, *13* (1), 2870. DOI: <https://doi.org/10.1038/s41467-022-30616-w>
- [14] Yuan, Y.; Wang, J.; Adimi, S.; Shen, H.; Thomas, T.; Ma, R.; Attfield, J. P.; Yang, M. Zirconium nitride catalysts surpass platinum for oxygen reduction. *Nat. Mater.* **2020**, *19* (3), 282-286. DOI: <https://doi.org/10.1038/s41563-019-0535-9>
- [15] Chandrasekaran, S.; Li, N.; Zhuang, Y.; Sui, L.; Xiao, Z.; Fan, D.; Aravindan, V.; Bowen, C.; Lu, H.; Liu, Y. Interface charge density modulation of a lamellar-like spatially separated Ni<sub>9</sub>S<sub>8</sub> nanosheet/Nb<sub>2</sub>O<sub>5</sub> nanobelt heterostructure catalyst coupled with nitrogen and metal (M = Co, Fe, or Cu) atoms to accelerate acidic and alkaline hydrogen evolution reactions. *Chem. Eng. J.* **2022**, *431*, 134073. DOI: <https://doi.org/10.1016/j.cej.2021.134073>.
- [16] Lv, Q.; Si, W.; He, J.; Sun, L.; Zhang, C.; Wang, N.; Yang, Z.; Li, X.; Wang, X.; Deng, W.; Long, Y.; Huang, C.; Li, Y. Selectively nitrogen-doped carbon materials as superior metal-free catalysts for oxygen reduction. *Nat. Commun.* **2018**, *9* (1), 3376. DOI: [10.1038/s41467-018-05878-y](https://doi.org/10.1038/s41467-018-05878-y).
- [17] Li, L.; Manthiram, A. Long-Life, High-Voltage Acidic Zn–Air Batteries. *Adv. Energy Mater.* **2016**, *6* (5), 1502054. DOI: <https://doi.org/10.1002/aenm.201502054>.
- [18] Lei, H.; Ma, L.; Wan, Q.; Huangfu, Z.; Tan, S.; Wang, Z.; Mai, W. Porous carbon nanofibers confined NiFe alloy nanoparticles as efficient bifunctional electrocatalysts for Zn-air batteries. *Nano Energy* **2022**, *104*, 107941. DOI: <https://doi.org/10.1016/j.nanoen.2022.107941>
- [19] Wang, F.; Borodin, O.; Gao, T.; Fan, X.; Sun, W.; Han, F.; Faraone, A.; Dura, J. A.; Xu, K.; Wang, C. Highly reversible zinc metal anode for aqueous batteries. *Nat. Mater.* **2018**, *17* (6), 543-549. DOI: <https://doi.org/10.1038/s41563-018-0063-z>.
- [20] Li, P.; Qiang, F.; Tan, X.; Li, Z.; Shi, J.; Liu, S.; Huang, M.; Chen, J.; Tian, W.; Wu, J.; Hu, W.; Wang, H. Electronic modulation induced by decorating single-atomic Fe-Co pairs with Fe-Co alloy clusters toward enhanced ORR/OER activity. *Appl. Catal. B: Environ.* **2024**, *340*, 123231. DOI: <https://doi.org/10.1016/j.apcatb.2023.123231>.
- [21] Ding, K.; Hu, J.; Zhao, L.; Jin, W.; Yu, H.; Liu, Y.; Wu, Z.; Cai, S.; Yang, Y.; Zou, G.; Hou, H.; Ji, X. Physical upcycling of spent artificial diamond accelerant into

bifunctional oxygen electrocatalyst with dual-metal active sites for durable rechargeable Zn–air batteries. *Nano Energy* **2024**, *121*, 109270. DOI: <https://doi.org/10.1016/j.nanoen.2024.109270>.

- [22] Yasin, G.;Ali, S.;Ibraheem, S.;Kumar, A.;Tabish, M.;Mushtaq, M. A.;Ajmal, S.;Arif, M.;Khan, M. A.;Saad, A.;Qiao, L.; Zhao, W. Simultaneously Engineering the Synergistic-Effects and Coordination-Environment of Dual-Single-Atomic Iron/Cobalt-sites as a Bifunctional Oxygen Electrocatalyst for Rechargeable Zinc-Air Batteries. *ACS Catal.* **2023**, *13* (4), 2313-2325. DOI: 10.1021/acscatal.2c05654.
- [23] Li, R.;Fan, W.;Rao, P.;Luo, J.;Li, J.;Deng, P.;Wu, D.;Huang, W.;Jia, C.;Liu, Z.;Miao, Z.; Tian, X. Multimetallic Single-Atom Catalysts for Bifunctional Oxygen Electrocatalysis. *ACS Nano* **2023**, *17* (18), 18128-18138. DOI: 10.1021/acsnano.3c04945.
- [24] Xu, Y.;Deng, P.;Chen, G.;Chen, J.;Yan, Y.;Qi, K.;Liu, H.; Xia, B. Y. 2D Nitrogen-Doped Carbon Nanotubes/Graphene Hybrid as Bifunctional Oxygen Electrocatalyst for Long-Life Rechargeable Zn–Air Batteries. *Adv. Fun. Mater.* **2020**, *30* (6), 1906081. DOI: <https://doi.org/10.1002/adfm.201906081>.
- [25] Zhou, T.;Zhang, N.;Wu, C.; Xie, Y. Surface/interface nanoengineering for rechargeable Zn–air batteries. *Energy Environ Sci.* **2020**, *13* (4), 1132-1153. DOI: 10.1039/c9ee03634b.
- [26] Song, Y.;Li, W.;Zhang, K.;Han, C.; Pan, A. Progress on Bifunctional Carbon-Based Electrocatalysts for Rechargeable Zinc–Air Batteries Based on Voltage Difference Performance. *Adv. Energy Mater.* **2024**, *14*, 2303352. DOI: <https://doi.org/10.1002/aenm.202303352>
- [27] Chen, S.;Liang, X.;Hu, S.;Li, X.;Zhang, G.;Wang, S.;Ma, L.;Wu, C.-M. L.;Zhi, C.; Zapien, J. A. Inducing Fe 3d Electron Delocalization and Spin-State Transition of FeN<sub>4</sub> Species Boosts Oxygen Reduction Reaction for Wearable Zinc–Air Battery. *Nano-Micro Lett.* **2023**, *15* (1), 47. DOI: 10.1007/s40820-023-01014-8.
- [28] Zhu, J.;Li, L.; Cao, M. Le Chatelier’s principle to stabilize intrinsic surface structure of oxygen-evolving catalyst for enabling ultra-high catalytic stability of zinc-air battery and water splitting. *Nano Energy* **2024**, *122*, 109300. DOI: <https://doi.org/10.1016/j.nanoen.2024.109300>.

- [29] Wang, Q.;Kaushik, S.;Xiao, X.; Xu, Q. Sustainable zinc–air battery chemistry: advances, challenges and prospects. *Chem. Soc. Rev.* **2023**, *52*, 6139-6190. DOI: 10.1039/d2cs00684g.
- [30] Dong, D.;Wang, T.;Sun, Y.;Fan, J.; Lu, Y.-C. Hydrotropic solubilization of zinc acetates for sustainable aqueous battery electrolytes. *Nat. Sustain.* **2023**, *6* (11), 1474-1484. DOI: 10.1038/s41893-023-01172-y.
- [31] Chandrasekaran, S.;Hu, R.;Yao, L.;Sui, L.;Liu, Y.;Abdelkader, A.;Li, Y.;Ren, X.; Deng, L. Mutual Self-Regulation of d-Electrons of Single Atoms and Adjacent Nanoparticles for Bifunctional Oxygen Electrocatalysis and Rechargeable Zinc-Air Batteries. *Nano-Micro Lett.* **2023**, *15* (1), 48. DOI: <https://doi.org/10.1007/s40820-023-01022-8>.
- [32] Zhang, P.;Chen, K.;Li, J.;Wang, M.;Li, M.;Liu, Y.; Pan, Y. Bifunctional Single Atom Catalysts for Rechargeable Zinc–Air Batteries: From Dynamic Mechanism to Rational Design. *Adv. Mater.* **2023**, *35* (35), 2303243. DOI: <https://doi.org/10.1002/adma.202303243>.
- [33] Zhang, J.;Dong, X.;Wang, G.;Chen, J.; Wang, R. Interfacial engineering-induced Janus heterostructures with enhanced electronic regulation for efficient oxygen electrocatalysis in rechargeable Zn-air batteries. *Appl. Catal. B: Environ.* **2024**, *342*, 123459. DOI: <https://doi.org/10.1016/j.apcatb.2023.123459>.
- [34] Wu, M.;Yang, X.;Cui, X.;Chen, N.;Du, L.;Cherif, M.;Chiang, F.-K.;Wen, Y.;Hassanpour, A.;Vidal, F.;Omanovic, S.;Yang, Y.;Sun, S.; Zhang, G. Engineering Fe-N<sub>4</sub> Electronic Structure with Adjacent Co-N<sub>2</sub>C<sub>2</sub> and Co Nanoclusters on Carbon Nanotubes for Efficient Oxygen Electrocatalysis. *Nano-Micro Lett.* **2023**, *15* (1), 232. DOI: 10.1007/s40820-023-01195-2.
- [35] Kumar, Y.;Mooste, M.; Tammeveski, K. Recent progress of transition metal-based bifunctional electrocatalysts for rechargeable zinc–air battery application. *Curr. Opin. Electrochem.* **2023**, *38*, 101229. DOI: <https://doi.org/10.1016/j.coelec.2023.101229>.
- [36] Sarapuu, A.;Lilloja, J.;Akula, S.;Zagal, J. H.;Specchia, S.; Tammeveski, K. Recent Advances in Non-Precious Metal Single-Atom Electrocatalysts for Oxygen Reduction Reaction in Low-Temperature Polymer-Electrolyte Fuel Cells. *ChemCatChem* **2023**, *15*, e202300849. DOI: <https://doi.org/10.1002/cctc.202300849>

- [37] Zou, X.; Tang, M.; Lu, Q.; Wang, Y.; Shao, Z.; An, L. Carbon-based electrocatalysts for rechargeable Zn-air batteries: Design concepts, recent progress and future perspectives. *Energy Environ Sci.* **2024**, *17*, 386-424. DOI: 10.1039/d3ee03059h.
- [38] Yao, Y.; Wu, J.; Feng, Q.; Zeng, K.; Wan, J.; Zhang, J.; Mao, B.; Hu, K.; Chen, L.; Zhang, H. Spontaneous Internal Electric Field in Heterojunction Boosts Bifunctional Oxygen Electrocatalysts for Zinc–Air Batteries: Theory, Experiment, and Application. *Small* **2023**, *2302015*. DOI: <https://doi.org/10.1002/smll.202302015>.
- [39] Li, Y.; Zhang, L.; Han, Y.; Ji, W.; Liu, Z.; Wang, B.; Zhao, S.; Wu, X.; Zhang, L.; Zhang, R. Interface engineering of bifunctional oxygen electrocatalysts for rechargeable Zn–air batteries. *Mater. Chem. Front.* **2023**, *7* (19), 4281-4303. DOI: 10.1039/d3qm00237c.
- [40] Huang, Z.; Liao, Z.; Yang, W.; Zhou, H.; Fu, C.; Gong, Y.; Chen, L.; Kuang, Y. Different types of nitrogen species in nitrogen-doped carbon material: The formation mechanism and catalytic role on oxygen reduction reaction. *Electrochimica Acta* **2017**, *245*, 957-966. DOI: <https://doi.org/10.1016/j.electacta.2017.06.026>.
- [41] Wu, J.; Liu, B.; Fan, X.; Ding, J.; Han, X.; Deng, Y.; Hu, W.; Zhong, C. Carbon-based cathode materials for rechargeable zinc-air batteries: From current collectors to bifunctional integrated air electrodes. *Carbon Energy* **2020**, *2* (3), 370-386. DOI: <https://doi.org/10.1002/cey2.60>.
- [42] Zhou, T.; Wu, X.; Liu, S.; Wang, A.; Liu, Y.; Zhou, W.; Sun, K.; Li, S.; Zhou, J.; Li, B.; Jiang, J. Biomass-Derived Catalytically Active Carbon Materials for the Air Electrode of Zn-Air Batteries. *ChemSusChem*, **2024**, e202301779. DOI: <https://doi.org/10.1002/cssc.202301779>.
- [43] Nazir, G.; Rehman, A.; Lee, J.-H.; Kim, C.-H.; Gautam, J.; Heo, K.; Hussain, S.; Ikram, M.; AlObaid, A. A.; Lee, S.-Y.; Park, S.-J. A Review of Rechargeable Zinc–Air Batteries: Recent Progress and Future Perspectives. *Nano-Micro Lett.* **2024**, *16*, 138. DOI: 10.1007/s40820-024-01328-1.
- [44] Devi, B.; Kurungot, S. Conductive metal–organic frameworks for zinc–air battery application: design principles, recent trends and prospects. *J. Mater. Chem. A* **2024**, *12*, 2605-2619. DOI: 10.1039/d3ta03753c.

- [45] Kundu, A.;Kuila, T.;Murmu, N. C.;Samanta, P.; Das, S. Metal–organic framework-derived advanced oxygen electrocatalysts as air-cathodes for Zn–air batteries: recent trends and future perspectives. *Mater. Horizons* **2023**, *10*, 745–787. DOI: 10.1039/d2mh01067d.
- [46] Dias, G. d. S.;Costa, J. M.; Almeida Neto, A. F. d. Transition metal chalcogenides carbon-based as bifunctional cathode electrocatalysts for rechargeable zinc-air battery: An updated review. *Adv. Colloid Interface Sci.* **2023**, *315*, 102891. DOI: <https://doi.org/10.1016/j.cis.2023.102891>
- [47] Fu, G.; Lee, J.-M. Ternary metal sulfides for electrocatalytic energy conversion. *J. Mater. Chem. A* **2019**, *7* (16), 9386–9405. DOI: 10.1039/c9ta01438a.
- [48] Leong, K. W.;Wang, Y.;Ni, M.;Pan, W.;Luo, S.; Leung, D. Y. C. Rechargeable Zn-air batteries: Recent trends and future perspectives. *Renew. Sustain. Energy Rev.* **2022**, *154*, 111771. DOI: <https://doi.org/10.1016/j.rser.2021.111771>.
- [49] Lv, X.-W.;Wang, Z.;Lai, Z.;Liu, Y.;Ma, T.;Geng, J.; Yuan, Z.-Y. Rechargeable Zinc–Air Batteries: Advances, Challenges, and Prospects. *Small* **2024**, *20*, 2306396. DOI: <https://doi.org/10.1002/smll.202306396>.
- [50] Bi, X.;Jiang, Y.;Chen, R.;Du, Y.;Zheng, Y.;Yang, R.;Wang, R.;Wang, J.;Wang, X.; Chen, Z. Rechargeable Zinc–Air versus Lithium–Air Battery: from Fundamental Promises Toward Technological Potentials. *Adv. Energy Mater.* **2024**, *14* (6), 2302388. DOI: <https://doi.org/10.1002/aenm.202302388>.
- [51] Anand, P.;Wong, M.-S.; Fu, Y.-P. Perovskite oxide composites for bifunctional oxygen electrocatalytic activity and zinc-air battery application- a mini-review. *Energy Storage Mater.* **2023**, *58*, 362-380. DOI: <https://doi.org/10.1016/j.ensm.2023.03.033>.
- [52] Costa, J. M.;Clark, M. P.;de Almeida Neto, A. F.; Ivey, D. G. In-situ transformation of electrodeposited W–Co oxide to ZnCo<sub>2</sub>O<sub>4</sub> nanoparticles as an effective bifunctional catalysts in Zn-air batteries. *Int. J. Hydrog. Energy* **2020**, *45*, 16122–16132. DOI: <https://doi.org/10.1016/j.ijhydene.2020.04.052>.
- [53] Luo, M.;Sun, W.;Xu, B. B.;Pan, H.; Jiang, Y. Interface Engineering of Air Electrocatalysts for Rechargeable Zinc–Air Batteries. *Adv. Energy Mater.* **2021**, *11* (4), 2002762. DOI: <https://doi.org/10.1002/aenm.202002762>.
- [54] Fu, J.;Cano, Z. P.;Park, M. G.;Yu, A.;Fowler, M.; Chen, Z. Electrically Rechargeable Zinc–Air Batteries: Progress, Challenges, and Perspectives. *Adv. Mater.* **2017**, *29* (7), 1604685. DOI: <https://doi.org/10.1002/adma.201604685>.

- [55] Zhao, Z.;Fan, X.;Ding, J.;Hu, W.;Zhong, C.; Lu, J. Challenges in Zinc Electrodes for Alkaline Zinc–Air Batteries: Obstacles to Commercialization. *ACS Energy Lett.* **2019**, *4* (9), 2259-2270. DOI: 10.1021/acsenergylett.9b01541.
- [56] Zhang, Z.;Deng, Y.-P.;Xing, Z.;Luo, D.;Sy, S.;Cano, Z. P.;Liu, G.;Jiang, Y.; Chen, Z. “Ship in a Bottle” Design of Highly Efficient Bifunctional Electrocatalysts for Long-Lasting Rechargeable Zn–Air Batteries. *ACS Nano* **2019**, *13*, 7062-7072. DOI: 10.1021/acsnano.9b02315.
- [57] Choi, E. Y.;Kim, D. E.;Lee, S. Y.;Park, C. B.; Kim, C. K. Cobalt nanoparticles-encapsulated holey nitrogen-doped carbon nanotubes for stable and efficient oxygen reduction and evolution reactions in rechargeable Zn-air batteries. *Appl. Catal. B: Environ.* **2023**, *325*, 122386. DOI: <https://doi.org/10.1016/j.apcatb.2023.122386>.
- [58] Kumar, Y.;Akula, S.;Kozlova, J.;Kikas, A.;Aruväli, J.;Käärik, M.;Treshchalov, A.;Leis, J.;Kisand, V.;Kukli, K.;Kibena-Põldsepp, E.; Tammeveski, K. Zinc-assisted synthesis of polymer framework-based atomically dispersed bimetal catalysts for efficient oxygen electrocatalysis in rechargeable zinc-air batteries. *J. Energy Storage* **2024**, *86*, 111164. DOI: <https://doi.org/10.1016/j.est.2024.111164>.
- [59] Muuli, K.;Lyu, X.;Mooste, M.;Käärik, M.;Zulevi, B.;Leis, J.;Yu, H.;Cullen, D. A.;Serov, A.; Tammeveski, K. Outstanding platinum group metal-free bifunctional catalysts for rechargeable zinc-air batteries. *Electrochim. Acta* **2023**, *446*, 142126. DOI: <https://doi.org/10.1016/j.electacta.2023.142126>.
- [60] Kumar, Y.;Kibena-Põldsepp, E.;Kozlova, J.;Kikas, A.;Käärik, M.;Aruväli, J.;Kisand, V.;Leis, J.;Tamm, A.; Tammeveski, K. Bimetal Phthalocyanine-Modified Carbon Nanotube-Based Bifunctional Catalysts for Zinc-Air Batteries. *ChemElectroChem* **2021**, *8*, 2662-2670. DOI: <https://doi.org/10.1002/celc.202100498>.
- [61] Lu, Q.;Zou, X.;Bu, Y.; Shao, Z. Structural design of supported electrocatalysts for rechargeable Zn–air batteries. *Energy Storage Mater.* **2023**, *55*, 166-192. DOI: <https://doi.org/10.1016/j.ensm.2022.11.046>
- [62] Li, L.;Tang, X.;Wu, B.;Huang, B.;Yuan, K.; Chen, Y. Advanced Architectures of Air Electrodes in Zinc–Air Batteries and Hydrogen Fuel Cells. *Adv. Mater.* **2023**, 2308326. DOI: <https://doi.org/10.1002/adma.202308326>.

- [63] Zhao, C.-X.;Liu, J.-N.;Wang, J.;Ren, D.;Li, B.-Q.; Zhang, Q. Recent advances of noble-metal-free bifunctional oxygen reduction and evolution electrocatalysts. *Chem. Soc. Rev.* **2021**, *50* (13), 7745-7778. DOI: <https://doi.org/10.1039/D1CS00135C>.
- [64] Zhu, Z.;Jiang, T.;Ali, M.;Meng, Y.;Jin, Y.;Cui, Y.; Chen, W. Rechargeable Batteries for Grid Scale Energy Storage. *Chem. Rev.* **2022**, *122* (22), 16610-16751. DOI: 10.1021/acs.chemrev.2c00289.
- [65] Yuan, L.;Hao, J.;Kao, C.-C.;Wu, C.;Liu, H.-K.;Dou, S.-X.; Qiao, S.-Z. Regulation methods for the Zn/electrolyte interphase and the effectiveness evaluation in aqueous Zn-ion batteries. *Energy Environ. Sci.* **2021**, *14* (11), 5669-5689. DOI: 10.1039/d1ee02021h.
- [66] Kumar, Y.;Kibena-Põldsepp, E.;Mooste, M.;Kozlova, J.;Kikas, A.;Aruväli, J.;Käärik, M.;Kisand, V.;Leis, J.;Tamm, A.;Holdcroft, S.;Zagal, J. H.; Tammeveski, K. Iron and Nickel Phthalocyanine-Modified Nanocarbon Materials as Cathode Catalysts for Anion-Exchange Membrane Fuel Cells and Zinc-Air Batteries\*\*. *ChemElectroChem* **2022**, *9*, e202200717. DOI: <https://doi.org/10.1002/celc.202200717>.
- [67] Bezerra, L. S.;Mooste, M.;Fortunato, G. V.;S. F. Cardoso, E.;R. V. Lanza, M.;Tammeveski, K.; Maia, G. Tuning NiCo<sub>2</sub>O<sub>4</sub> bifunctionality with nitrogen-doped graphene nanoribbons in oxygen electrocatalysis for zinc-air battery application. *J. Electroanal. Chem.* **2023**, *928*, 117000. DOI: <https://doi.org/10.1016/j.jelechem.2022.117000>.
- [68] Hao, J.;Li, X.;Zeng, X.;Li, D.;Mao, J.; Guo, Z. Deeply understanding the Zn anode behaviour and corresponding improvement strategies in different aqueous Zn-based batteries. *Energy Environ. Sci.* **2020**, *13*, 3917-3949. DOI: 10.1039/d0ee02162h.
- [69] Parker, J. F.;Chervin, C. N.;Nelson, E. S.;Rolison, D. R.; Long, J. W. Wiring zinc in three dimensions re-writes battery performance—dendrite-free cycling. *Energy Environ. Sci.* **2014**, *7*, 1117-1124. DOI: 10.1039/c3ee43754j.
- [70] Parker, J. F.;Nelson, E. S.;Wattendorf, M. D.;Chervin, C. N.;Long, J. W.; Rolison, D. R. Retaining the 3D Framework of Zinc Sponge Anodes upon Deep Discharge in Zn–Air Cells. *ACS Appl. Mater. Inter.* **2014**, *6*, 19471-19476. DOI: 10.1021/am505266c.

- [71] Zuo, Y.;Wang, K.;Pei, P.;Wei, M.;Liu, X.;Xiao, Y.; Zhang, P. Zinc dendrite growth and inhibition strategies. *Mater. Today Energy* **2021**, *20*, 100692. DOI: <https://doi.org/10.1016/j.mtener.2021.100692>.
- [72] Yu, H.;Chen, Y.;Wei, W.;Ji, X.; Chen, L. A Functional Organic Zinc-Chelate Formation with Nanoscaled Granular Structure Enabling Long-Term and Dendrite-Free Zn Anodes. *ACS Nano* **2022**, *16*, 9736-9747. DOI: [10.1021/acsnano.2c03398](https://doi.org/10.1021/acsnano.2c03398).
- [73] Yan, Y.;Shu, C.;Zeng, T.;Wen, X.;Liu, S.;Deng, D.; Zeng, Y. Surface-Preferred Crystal Plane Growth Enabled by Underpotential Deposited Monolayer toward Dendrite-Free Zinc Anode. *ACS Nano* **2022**, *16*, 9150-9162. DOI: [10.1021/acsnano.2c01380](https://doi.org/10.1021/acsnano.2c01380).
- [74] Chu, J.;Wang, W. A.;Feng, J.;Lao, C.-Y.;Xi, K.;Xing, L.;Han, K.;Li, Q.;Song, L.;Li, P.;Li, X.; Bao, Y. Deeply Nesting Zinc Sulfide Dendrites in Tertiary Hierarchical Structure for Potassium Ion Batteries: Enhanced Conductivity from Interior to Exterior. *ACS Nano* **2019**, *13*, 6906-6916. DOI: [10.1021/acsnano.9b01773](https://doi.org/10.1021/acsnano.9b01773).
- [75] Tian, Y.;An, Y.;Wei, C.;Xi, B.;Xiong, S.;Feng, J.; Qian, Y. Flexible and Free-Standing Ti<sub>3</sub>C<sub>2</sub>Tx MXene@Zn Paper for Dendrite-Free Aqueous Zinc Metal Batteries and Nonaqueous Lithium Metal Batteries. *ACS Nano* **2019**, *13*, 11676-11685. DOI: [10.1021/acsnano.9b05599](https://doi.org/10.1021/acsnano.9b05599).
- [76] An, Y.;Tian, Y.;Xiong, S.;Feng, J.; Qian, Y. Scalable and Controllable Synthesis of Interface-Engineered Nanoporous Host for Dendrite-Free and High Rate Zinc Metal Batteries. *ACS Nano* **2021**, *15*, 11828-11842. DOI: [10.1021/acsnano.1c02928](https://doi.org/10.1021/acsnano.1c02928).
- [77] Song, X.;Bai, L.;Wang, C.;Wang, D.;Xu, K.;Dong, J.;Li, Y.;Shen, Q.; Yang, J. Synergistic Cooperation of Zn(002) Texture and Amorphous Zinc Phosphate for Dendrite-Free Zn Anodes. *ACS Nano* **2023**, *17*, 15113-15124. DOI: [10.1021/acsnano.3c04343](https://doi.org/10.1021/acsnano.3c04343).
- [78] Jiao, S.;Fu, J.;Wu, M.;Hua, T.; Hu, H. Ion Sieve: Tailoring Zn<sup>2+</sup> Desolvation Kinetics and Flux toward Dendrite-Free Metallic Zinc Anodes. *ACS Nano* **2022**, *16*, 1013-1024. DOI: [10.1021/acsnano.1c08638](https://doi.org/10.1021/acsnano.1c08638).
- [79] Zhong, X.;Shao, Y.;Chen, B.;Li, C.;Sheng, J.;Xiao, X.;Xu, B.;Li, J.;Cheng, H.-M.; Zhou, G. Rechargeable Zinc–Air Batteries with an Ultralarge Discharge

- Capacity per Cycle and an Ultralong Cycle Life. *Adv. Mater.* **2023**, *35*, 2301952. DOI: <https://doi.org/10.1002/adma.202301952>.
- [80] Das, S.;Kundu, A.;Kuila, T.; Murmu, N. C. Recent advancements on designing transition metal-based carbon-supported single atom catalysts for oxygen electrocatalysis: Miles to go for sustainable Zn-air batteries. *Energy Storage Mater.* **2023**, *61*, 102890. DOI: <https://doi.org/10.1016/j.ensm.2023.102890>.
- [81] Shang, N.;Wang, K.;Wei, M.;Zuo, Y.;Zhang, P.;Wang, H.;Chen, Z.; Pei, P. Challenges for large scale applications of rechargeable Zn–air batteries. *J. Mater. Chem. A* **2022**, *10*, 16369-16389. DOI: 10.1039/d2ta04294k.
- [82] An, Y.;Tian, Y.;Liu, C.;Xiong, S.;Feng, J.; Qian, Y. Rational Design of Sulfur-Doped Three-Dimensional Ti<sub>3</sub>C<sub>2</sub>Tx MXene/ZnS Heterostructure as Multifunctional Protective Layer for Dendrite-Free Zinc-Ion Batteries. *ACS Nano* **2021**, *15* (9), 15259-15273. DOI: 10.1021/acsnano.1c05934.
- [83] Tian, H.;Li, Z.;Feng, G.;Yang, Z.;Fox, D.;Wang, M.;Zhou, H.;Zhai, L.;Kushima, A.; Du, Y. Stable, high-performance, dendrite-free, seawater-based aqueous batteries. *Nat. Commun.* **2021**, *12*, 237.
- [84] Chandrasekaran, S.;Zhang, C.;Shu, Y.;Wang, H.;Chen, S.;Nesakumar Jebakumar Immanuel Edison, T.;Liu, Y.;Karthik, N.;Misra, R. D. K.;Deng, L.;Yin, P.;Ge, Y.;Al-Hartomy, O. A.;Al-Ghamdi, A.;Wageh, S.;Zhang, P.;Bowen, C.; Han, Z. Advanced opportunities and insights on the influence of nitrogen incorporation on the physico-/electro-chemical properties of robust electrocatalysts for electrocatalytic energy conversion. *Coord. Chem. Rev.* **2021**, *449*, 214209. DOI: <https://doi.org/10.1016/j.ccr.2021.214209>.
- [85] Wang, N.;Chen, D.;Ning, S.;Lao, J.;Xu, J.;Luo, M.;Zhang, W.;Chen, J.;Yang, M.; Xie, F. Fe Cluster Modified Co<sub>9</sub>S<sub>8</sub> Heterojunction: Highly Efficient Photoelectrocatalyst for Overall Water Splitting and Flexible Zinc-Air Batteries. *Adv. Mater.* **2023**, 2306138. DOI: <https://doi.org/10.1002/adma.202306138>.
- [86] Fan, X.;Zhang, R.;Sui, S.;Liu, X.;Liu, J.;Shi, C.;Zhao, N.;Zhong, C.; Hu, W. Starch-Based Superabsorbent Hydrogel with High Electrolyte Retention Capability and Synergistic Interface Engineering for Long-Lifespan Flexible Zinc– Air Batteries. *Angew. Chem. Int. Ed.* **2023**, *62* (22), e202302640. DOI: <https://doi.org/10.1002/anie.202302640>.

- [87] Chen, J.; Wang, Y.; Tian, Z.; Zhao, J.; Ma, Y.; Alshareef, H. N. Recent developments in three-dimensional Zn metal anodes for battery applications. *InfoMat* **2024**, *6*, e12485. DOI: <https://doi.org/10.1002/inf2.12485>.
- [88] Dong, F.; Wu, M.; Chen, Z.; Liu, X.; Zhang, G.; Qiao, J.; Sun, S. Atomically dispersed transition metal–nitrogen–carbon bifunctional oxygen electrocatalysts for zinc-air batteries: recent advances and future perspectives. *Nano-Micro Lett.* **2022**, *14*, 36. DOI: <https://doi.org/10.1007/s40820-021-00768-3>.
- [89] Tang, K.; Hu, H.; Xiong, Y.; Chen, L.; Zhang, J.; Yuan, C.; Wu, M. Hydrophobization engineering of the air–cathode catalyst for improved oxygen diffusion towards efficient zinc–air batteries. *Angew. Chem. Int. Ed.* **2022**, *134*, e202202671. DOI: <https://doi.org/10.1002/anie.202202671>.
- [90] Zheng, X.; Cao, Y.; Liu, D.; Cai, M.; Ding, J.; Liu, X.; Wang, J.; Hu, W.; Zhong, C. Bimetallic Metal–Organic-Framework/Reduced Graphene Oxide Composites as Bifunctional Electrocatalysts for Rechargeable Zn–Air Batteries. *ACS Appl. Mater. Inter.* **2019**, *11*, 15662–15669. DOI: [10.1021/acsami.9b02859](https://doi.org/10.1021/acsami.9b02859).
- [91] Huo, L.; Lv, M.; Li, M.; Ni, X.; Guan, J.; Liu, J.; Mei, S.; Yang, Y.; Zhu, M.; Feng, Q.; Geng, P.; Hou, J.; Huang, N.; Liu, W.; Kong, X. Y.; Zheng, Y.; Ye, L. Amorphous MnO<sub>2</sub> Lamellae Encapsulated Covalent Triazine Polymer-Derived Multi-Heteroatoms-Doped Carbon for ORR/OER Bifunctional Electrocatalysis. *Adv. Mater.* **2024**, 2312868. DOI: <https://doi.org/10.1002/adma.202312868>.
- [92] Sari, F. N. I.; Lai, Y.-C.; Huang, Y.-J.; Wei, X.-Y.; Pourzolfaghar, H.; Chang, Y.-H.; Ghufron, M.; Li, Y.-Y.; Su, Y.-H.; Clemens, O.; Ting, J.-M. Electronic Structure Engineering in NiFe Sulfide via A Third Metal Doping as Efficient Bifunctional OER/ORR Electrocatalyst for Rechargeable Zinc-Air Battery. *Adv. Funct. Mater.* **2024**, 2310181. DOI: <https://doi.org/10.1002/adfm.202310181>.
- [93] Liu, F.; Fan, Z. Defect engineering of two-dimensional materials for advanced energy conversion and storage. *Chem. Soc. Rev.* **2023**, *52*, 1723–1772. DOI: <https://doi.org/10.1039/D2CS00931E>.
- [94] Sun, H.; Song, S.; Xu, X.; Dai, J.; Yu, J.; Zhou, W.; Shao, Z.; Jung, W. Recent progress on structurally ordered materials for electrocatalysis. *Adv. Energy Mater.* **2021**, *11*, 2101937. DOI: <https://doi.org/10.1002/aenm.202101937>.
- [95] Weng, C.-C.; Ren, J.-T.; Wang, H.-Y.; Lv, X.-W.; Song, Y.-J.; Wang, Y.-S.; Chen, L.; Tian, W.-W.; Yuan, Z.-Y. Triple-phase oxygen electrocatalysis of hollow

- spherical structures for rechargeable Zn-Air batteries. *Appl. Catal. B: Environ.* **2022**, *307*, 121190. DOI: <https://doi.org/10.1016/j.apcatb.2022.121190>.
- [96] Pan, J.;Xu, Y. Y.;Yang, H.;Dong, Z.;Liu, H.;Xia, B. Y. Advanced architectures and relatives of air electrodes in Zn-air batteries. *Adv. Sci.* **2018**, *5*, 1700691. DOI: <https://doi.org/10.1002/advs.201700691>.
- [97] Liu, J. N.;Zhao, C. X.;Ren, D.;Wang, J.;Zhang, R.;Wang, S. H.;Zhao, C.;Li, B. Q.; Zhang, Q. Preconstructing asymmetric interface in air cathodes for high-performance rechargeable Zn-air batteries. *Adv. Mater.* **2022**, *34*, 2109407. DOI: <https://doi.org/10.1002/adma.202109407>.
- [98] Fan, F.;Huang, Q.;Rani, K. K.;Peng, X.;Liu, X.;Wang, L.;Yang, Z.;Huang, D.;Devasenathipathy, R.;Chen, D.-H.;Fan, Y.; Chen, W. Interface and doping engineering of Co-based electrocatalysts for enhanced oxygen reduction and evolution reactions. *Chem. Eng. J.* **2023**, *470*, 144380. DOI: <https://doi.org/10.1016/j.cej.2023.144380>.
- [99] Peng, Y.;Bian, Z.;Zhang, W.; Wang, H. Identifying the key N species for electrocatalytic oxygen reduction reaction on N-doped graphene. *Nano Research* **2023**, *16*, 6642-6651. DOI: 10.1007/s12274-023-5421-0.
- [100] Ma, R.;Lin, G.;Zhou, Y.;Liu, Q.;Zhang, T.;Shan, G.;Yang, M.; Wang, J. A review of oxygen reduction mechanisms for metal-free carbon-based electrocatalysts. *NPJ Comput. Mater.* **2019**, *5*, 78. DOI: 10.1038/s41524-019-0210-3.
- [101] Chen, Y.;Qiao, S.;Tang, Y.;Du, Y.;Zhang, D.;Wang, W.;Zhang, H.;Sun, X.; Liu, C. Double-Faced Atomic-Level Engineering of Hollow Carbon Nanofibers as Free-Standing Bifunctional Oxygen Electrocatalysts for Flexible Zn–Air Battery. *ACS Nano* **2022**, *16*, 15273-15285. DOI: 10.1021/acsnano.2c06700.
- [102] Na, R.;Min, K.;Kim, H.;Son, Y.;Shim, S. E.; Baeck, S.-H. Boosting electrocatalytic activity with the formation of abundant heterointerfaces and N, S dual-doped carbon nanotube for rechargeable Zn-air battery. *J. Energy Chem.* **2023**, *84*, 140-152. DOI: <https://doi.org/10.1016/j.jechem.2023.05.040>.
- [103] Zheng, H.;Wang, S.;Liu, S.;Wu, J.;Guan, J.;Li, Q.;Wang, Y.;Tao, Y.;Hu, S.; Bai, Y. The Heterointerface between Fe<sub>1</sub>/NC and Selenides Boosts Reversible Oxygen Electrocatalysis. *Adv. Funct. Mater.* **2023**, *33*, 2300815. DOI: <https://doi.org/10.1002/adfm.202300815>.

- [104] Wang, P.;Zhao, D.; Yin, L. Two-dimensional matrices confining metal single atoms with enhanced electrochemical reaction kinetics for energy storage applications. *Energy Environ. Sci.* **2021**, *14*, 1794-1834. DOI: <https://doi.org/10.1039/D0EE02651D>.
- [105] Niu, Y.;Xiao, M.;Zhu, J.;Zeng, T.;Li, J.;Zhang, W.;Su, D.;Yu, A.; Chen, Z. A "trimurti" heterostructured hybrid with an intimate CoO/CoxP interface as a robust bifunctional air electrode for rechargeable Zn–air batteries. *J. Mater. Chem. A* **2020**, *8*, 9177-9184. DOI: 10.1039/d0ta01145b.
- [106] Lu, Q.;Zou, X.;Wang, X.;An, L.;Shao, Z.; Bu, Y. Simultaneous reactant accessibility and charge transfer engineering in Co-doped RuO<sub>2</sub>-supported OCNT for robust rechargeable zinc-air batteries. *Appl. Catal. B: Environ.* **2023**, *325*, 122323. DOI: <https://doi.org/10.1016/j.apcatb.2022.122323>.
- [107] Zuo, Y.;Wang, K.;Zhao, S.;Wei, M.;Liu, X.;Zhang, P.;Xiao, Y.; Xiong, J. A high areal capacity solid-state zinc-air battery via interface optimization of electrode and electrolyte. *Chem. Eng. J.* **2022**, *430*, 132996. DOI: <https://doi.org/10.1016/j.cej.2021.132996>.
- [108] Pan, L.;Chen, D.;Pei, P.;Huang, S.;Ren, P.; Song, X. A novel structural design of air cathodes expanding three-phase reaction interfaces for zinc-air batteries. *Appl. Energy* **2021**, *290*, 116777. DOI: <https://doi.org/10.1016/j.apenergy.2021.116777>.
- [109] Tian, Y.;Xu, L.;Li, M.;Yuan, D.;Liu, X.;Qian, J.;Dou, Y.;Qiu, J.; Zhang, S. Interface engineering of CoS/CoO@ N-doped graphene nanocomposite for high-performance rechargeable Zn–Air batteries. *Nano-Micro Lett.* **2021**, *13*, 1-15. DOI: <https://doi.org/10.1007/s40820-020-00526-x>
- [110] Fang, B.;Yang, J.;Chen, C.;Zhang, C.;Chang, D.;Xu, H.; Gao, C. Carbon Nanotubes Loaded on Graphene Microfolds as Efficient Bifunctional Electrocatalysts for the Oxygen Reduction and Oxygen Evolution Reactions. *ChemCatChem* **2017**, *9*, 4520-4528. DOI: <https://doi.org/10.1002/cctc.201700985>.
- [111] Yasin, G.;Ibrahim, S.;Ibraheem, S.;Ali, S.;Iqbal, R.;Kumar, A.;Tabish, M.;Slimani, Y.;Nguyen, T. A.; Xu, H. Defective/graphitic synergy in a heteroatom-interlinked-triggered metal-free electrocatalyst for high-performance rechargeable zinc–air batteries. *J. Mater. Chem. A* **2021**, *9*, 18222-18230. DOI: <https://doi.org/10.1039/D1TA05812F>.

- [112] Xiao, Y.;Cheng, Z.;Zhao, Y.; Qu, L. Highly crumpled nanocarbons as efficient metal-free electrocatalysts for zinc–air batteries. *Nanoscale* **2018**, *10*, 15706–15713. DOI: <https://doi.org/10.1039/C8NR04068K>.
- [113] Mooste, M.;Ahmed, Z.;Kapitulskis, P.;Ivanov, R.;Treshchalov, A.;Piirsoo, H.-M.;Kikas, A.;Kisand, V.;Kukli, K.;Hussainova, I.; Tammeveski, K. Bifunctional oxygen electrocatalyst based on Fe, Co, and nitrogen co-doped graphene-coated alumina nanofibers for Zn-air battery air electrode. *Appl. Surf. Sci.* **2024**, *660*, 160024. DOI: <https://doi.org/10.1016/j.apsusc.2024.160024>.
- [114] Zhao, J.;Li, Q.;Zhang, Q.; Liu, R. Carbon tube-graphene heterostructure with different N-doping configurations induces an electrochemically active-active interface for efficient oxygen electrocatalysis. *Chem. Eng. J.* **2022**, *431*, 133730. DOI: <https://doi.org/10.1016/j.cej.2021.133730>.
- [115] Wang, B.;Zhao, P.;Feng, J.;Chen, D.;Huang, Y.;Sui, L.;Dong, H.;Ma, S.;Dong, L.; Yu, L. Carbon-based 0D/1D/2D assembly with desired structures and defect states as non-metal bifunctional electrocatalyst for zinc-air battery. *J. Colloid Interface Sci.* **2021**, *588*, 184-195. DOI: <https://doi.org/10.1016/j.jcis.2020.12.051>.
- [116] Liu, C.;Liu, F.;Li, H.;Chen, J.;Fei, J.;Yu, Z.;Yuan, Z.;Wang, C.;Zheng, H.;Liu, Z.;Xu, M.;Henkelman, G.;Wei, L.; Chen, Y. One-Dimensional van der Waals Heterostructures as Efficient Metal-Free Oxygen Electrocatalysts. *ACS Nano* **2021**, *15*, 3309-3319. DOI: [10.1021/acsnano.0c10242](https://doi.org/10.1021/acsnano.0c10242).
- [117] Nguyen, T. H.;Tran, P. K. L.;Dinh, V. A.;Tran, D. T.;Kim, N. H.; Lee, J. H. Metal Single-Site Molecular Complex–MXene Heteroelectrocatalysts Interspersed Graphene Nanonetwork for Efficient Dual-Task of Water Splitting and Metal–Air Batteries. *Adv. Funct. Mater.* **2023**, *33*, 2210101. DOI: <https://doi.org/10.1002/adfm.202210101>
- [118] Qiao, J.;Kong, L.;Xu, S.;Lin, K.;He, W.;Ni, M.;Ruan, Q.;Zhang, P.;Liu, Y.; Zhang, W. Research progress of MXene-based catalysts for electrochemical water-splitting and metal-air batteries. *Energy Storage Mater.* **2021**, *43*, 509–530. DOI: <https://doi.org/10.1016/j.ensm.2021.09.034>
- [119] Qiao, J.;Bao, Z.;Kong, L.;Liu, X.;Lu, C.;Ni, M.;He, W.;Zhou, M.; Sun, Z. MOF-derived heterostructure CoNi/CoNiP anchored on MXene framework as

- a superior bifunctional electrocatalyst for zinc-air batteries. *Chinese Chem. Lett.* **2023**, *34*, 108318. DOI: <https://doi.org/10.1016/j.cclet.2023.108318>.
- [120] Zong, H.;Liu, W.;Li, M.;Gong, S.;Yu, K.; Zhu, Z. Oxygen-Terminated Nb<sub>2</sub>CO<sub>2</sub> MXene with Interfacial Self-Assembled COF as a Bifunctional Catalyst for Durable Zinc–Air Batteries. *ACS Appl. Mater. Interfaces* **2022**, *14*, 10738-10746. DOI: <https://doi.org/10.1021/acsami.1c25264>
- [121] Han, S.;Chen, Y.;Hao, Y.;Xie, Y.;Xie, D.;Chen, Y.;Xiong, Y.;He, Z.;Hu, F.;Li, L.;Zhu, J.; Peng, S. Multi-dimensional hierarchical CoS<sub>2</sub>@MXene as trifunctional electrocatalysts for zinc-air batteries and overall water splitting. *Science China Mater.* **2021**, *64*, 1127-1138. DOI: 10.1007/s40843-020-1524-5.
- [122] Lei, H.;Tan, S.;Ma, L.;Liu, Y.;Liang, Y.;Javed, M. S.;Wang, Z.;Zhu, Z.; Mai, W. Strongly Coupled NiCo<sub>2</sub>O<sub>4</sub> Nanocrystal/MXene Hybrid through In Situ Ni/Co–F Bonds for Efficient Wearable Zn–Air Batteries. *ACS Appl. Mater. Interfaces* **2020**, *12*, 44639-44647. DOI: 10.1021/acsami.0c11185.
- [123] Faraji, M.;Yousefzadeh, S.;Nassar, M. F.; Zahra, M. M. A. MnCo<sub>2</sub>O<sub>4</sub>/N-doped graphene quantum dot vigorously coupled to MXene nanosheet: A bifunctional Oxygen electrocatalyst outperforms Pt/IrO<sub>2</sub> benchmark electrocatalysts in metal-air batteries. *J. Alloys Compd.* **2022**, *927*, 167115. DOI: <https://doi.org/10.1016/j.jallcom.2022.167115>
- [124] Faraji, M.; Arianpouya, N. NiCoFe-layered double hydroxides/MXene/N-doped carbon nanotube composite as a high performance bifunctional catalyst for oxygen electrocatalytic reactions in metal-air batteries. *J. Electroanal. Chem.* **2021**, *901*, 115797. DOI: <https://doi.org/10.1016/j.jelechem.2021.115797>
- [125] Hui, X.;Zhang, P.;Wang, Z.;Zhao, D.;Li, Z.;Zhang, Z.;Wang, C.; Yin, L. Vacancy Defect-Rich Perovskite SrTiO<sub>3</sub>/Ti<sub>3</sub>C<sub>2</sub> Heterostructures In Situ Derived from Ti<sub>3</sub>C<sub>2</sub> MXenes with Exceptional Oxygen Catalytic Activity for Advanced Zn–Air Batteries. *ACS Appl. Energy Mater.* **2022**, *5*, 6100-6109. DOI: <https://doi.org/10.1021/acsadm.2c00494>
- [126] Wang, Y.;Gu, F.;Cao, L.;Fan, L.;Hou, T.;Zhu, Q.;Wu, Y.; Xiong, S. TiCN MXene hybrid BCN nanotubes with trace level Co as an efficient ORR electrocatalyst for Zn-air batteries. *Int. J. Hydrot. Energy* **2022**, *47*, 20894-20904. DOI: <https://doi.org/10.1016/j.ijhydene.2022.04.211>
- [127] Zhang, C.;Dong, H.;Chen, B.;Jin, T.;Nie, J.; Ma, G. 3D MXene anchored carbon nanotube as bifunctional and durable oxygen catalysts for Zn–air

- batteries. *Carbon* **2021**, *185*, 17-26. DOI: <https://doi.org/10.1016/j.carbon.2021.09.004>.
- [128] Wang, N.;Ning, S.;Yu, X.;Chen, D.;Li, Z.;Xu, J.;Meng, H.;Zhao, D.;Li, L.; Liu, Q. Graphene composites with Ru-RuO<sub>2</sub> heterostructures: Highly efficient Mott–Schottky-type electrocatalysts for pH-universal water splitting and flexible zinc–air batteries. *Appl. Catal. B: Environ.* **2022**, *302*, 120838. DOI: <https://doi.org/10.1016/j.apcatb.2021.120838>.
- [129] Bharadwaj, N.;Das, S.; Pathak, B. Role of Morphology of Platinum-Based Nanoclusters in ORR/OER Activity for Nonaqueous Li–Air Battery Applications. *ACS Appl. Energy Mater.* **2022**, *5*, 12561-12570. DOI: <https://doi.org/10.1021/acsaem.2c02198>.
- [130] Lu, Y.-C.;Xu, Z.;Gasteiger, H. A.;Chen, S.;Hamad-Schifferli, K.; Shao-Horn, Y. Platinum– gold nanoparticles: a highly active bifunctional electrocatalyst for rechargeable lithium– air batteries. *J Am Chem Soc.* **2010**, *132*, 12170-12171. DOI: <https://doi.org/10.1021/ja1036572>
- [131] Li, J.;Meng, Z.;Brett, D. J.;Shearing, P. R.;Skipper, N. T.;Parkin, I. P.; Gadielli, S. High-Performance Zinc–Air Batteries with Scalable Metal–Organic Frameworks and Platinum Carbon Black Bifunctional Catalysts. *ACS Appl. Mater. Interfaces.* **2020**, *12*, 42696-42703. DOI: <https://doi.org/10.1021/acsami.0c10151>.
- [132] Liu, K.;Huang, H.;Zhu, Y.;Wang, S.;Lyu, Z.;Han, X.;Kuang, Q.; Xie, S. Edge-segregated ternary Pd–Pt–Ni spiral nanosheets as high-performance bifunctional oxygen redox electrocatalysts for rechargeable zinc–air batteries. *J. Mater. Chem. A* **2022**, *10*, 3808-3817. DOI: 10.1039/d1ta10585j.
- [133] Qin, Q.;Jang, H.;Chen, L.;Li, P.;Wei, T.;Liu, X.; Cho, J. Coupling a Low Loading of IrP<sub>2</sub>, PtP<sub>2</sub>, or Pd<sub>3</sub>P with Heteroatom-Doped Nanocarbon for Overall Water-Splitting Cells and Zinc–Air Batteries. *ACS Appl. Mater. Interfaces.* **2019**, *11*, 16461-16473. DOI: 10.1021/acsami.8b21155.
- [134] Zhou, C.;Chen, X.;Liu, S.;Han, Y.;Meng, H.;Jiang, Q.;Zhao, S.;Wei, F.;Sun, J.;Tan, T.; Zhang, R. Superdurable Bifunctional Oxygen Electrocatalyst for High-Performance Zinc–Air Batteries. *J Am Chem Soc.* **2022**, *144*, 2694-2704. DOI: 10.1021/jacs.1c11675.
- [135] Zhuang, X.;Zhou, Y.;Jiang, Z.;Yao, X.; Yu, X.-Y. Synergetic electronic modulation and nanostructure engineering of heterostructured RuO<sub>2</sub>/Co<sub>3</sub>O<sub>4</sub>

- as advanced bifunctional electrocatalyst for zinc–air batteries. *J. Mater. Chem. A* **2021**, *9*, 26669-26675. DOI: <https://doi.org/10.1039/D1TA09278B>.
- [136] Wang, X.;Sunarso, J.;Lu, Q.;Zhou, Z.;Dai, J.;Guan, D.;Zhou, W.; Shao, Z. High-performance platinum-perovskite composite bifunctional oxygen electrocatalyst for rechargeable Zn–air battery. *Adv. Energy Mater.* **2020**, *10*, 1903271. DOI: <https://doi.org/10.1002/aenm.201903271>
- [137] Kang, T.;Nam, D.; Kim, J. Activated palladium deposited on defect-rich carbon and cobalt oxide composite materials as bi-functional catalysts for stable rechargeable Zn–air battery. *Appl. Surf. Sci.* **2022**, *582*, 152442. DOI: <https://doi.org/10.1016/j.apsusc.2022.152442>
- [138] Wang, S.;Lin, Z.;Li, M.;Yu, Z.;Zhang, M.;Gong, M.;Tang, Y.; Qiu, X. Coupling isolated Ni single atoms with sub-10 nm Pd nanocrystals embedded in porous carbon frameworks to boost oxygen electrocatalysis for Zn–air batteries. *J. Mater. Chem. A* **2022**, *10*, 6086-6095. DOI: 10.1039/d1ta06897k.
- [139] Li, Z.;Li, H.;Li, M.;Hu, J.;Liu, Y.;Sun, D.;Fu, G.; Tang, Y. Iminodiacetonitrile induce-synthesis of two-dimensional PdNi/Ni@carbon nanosheets with uniform dispersion and strong interface bonding as an effective bifunctional eletrocatalyst in air-cathode. *Energy Storage Mater.* **2021**, *42*, 118-128. DOI: <https://doi.org/10.1016/j.ensm.2021.07.027>.
- [140] Zhang, J.;Lian, J.;Jiang, Q.; Wang, G. Boosting the OER/ORR/HER activity of Ru-doped Ni/Co oxides heterostructure. *Chem. Eng. J.* **2022**, *439*, 135634. DOI: <https://doi.org/10.1016/j.cej.2022.135634>.
- [141] Feng, W.;Feng, Y.;Chen, J.;Wang, H.;Hu, Y.;Luo, T.;Yuan, C.;Cao, L.;Feng, L.; Huang, J. Interfacial electronic engineering of Ru/FeRu nanoparticles as efficient trifunctional electrocatalyst for overall water splitting and Zn-air battery. *Chem. Eng. J.* **2022**, *437*, 135456. DOI: <https://doi.org/10.1016/j.cej.2022.135456>.
- [142] Liu, X.;Chen, S.;Wang, H.;Liu, A.;Wen, S.;Mi, L.; Li, Y. Lattice confined Ru single sites in hollow Co<sub>9</sub>S<sub>8</sub> polyhedron triggering Co-S-Ru catalytic centers for rechargeable Zn-air battery. *Nano Research* **2023**, *16*, 6701-6709. DOI: 10.1007/s12274-023-5469-5.
- [143] Muthurasu, A.;Tiwari, A. P.;Chhetri, K.;Dahal, B.; Kim, H. Y. Construction of iron doped cobalt-vanadate-cobalt oxide with metal-organic framework oriented nanoflakes for portable rechargeable zinc-air batteries powered total

- water splitting. *Nano Energy* **2021**, *88*, 106238. DOI: <https://doi.org/10.1016/j.nanoen.2021.106238>.
- [144] Weng, C.-C.;Lv, X.-W.;Ren, J.-T.;Wang, Y.-S.;Tian, W.-W.;Gao, L.-J.;Wang, H.-Y.; Yuan, Z.-Y. Self-Promoted Electrocatalysts Derived from Surface Reconstruction for Rechargeable Zinc–Air Batteries. *ACS Sustain. Chem. Eng* **2022**, *10*, 6456-6465. DOI: <https://doi.org/10.1021/acssuschemeng.2c01568>.
- [145] Qin, Z.;Song, Y.;Shi, H.-Y.;Li, C.;Guo, D.;Sun, X.; Liu, X.-X. Heterojunction induced activation of iron oxide anode for high-power aqueous batteries. *Chem. Eng. J.* **2020**, *400*, 125874. DOI: <https://doi.org/10.1016/j.cej.2020.125874>.
- [146] Arafat, Y.;Zhong, Y.;Azhar, M. R.;Asif, M.;Tadé, M. O.; Shao, Z. CoNiFe-layered double hydroxide decorated Co-N-C network as a robust bi-functional oxygen electrocatalyst for zinc-air batteries. *EcoMat* **2023**, *5*, e12394. DOI: <https://doi.org/10.1002/eom2.12394>.
- [147] Zhang, T.;Bian, J.;Zhu, Y.; Sun, C. FeCo Nanoparticles Encapsulated in N-Doped Carbon Nanotubes Coupled with Layered Double (Co, Fe) Hydroxide as an Efficient Bifunctional Catalyst for Rechargeable Zinc–Air Batteries. *Small* **2021**, *17*, 2103737. DOI: <https://doi.org/10.1002/smll.202103737>.
- [148] Wei, L.;Ang, E. H.;Yang, Y.;Qin, Y.;Zhang, Y.;Ye, M.;Liu, Q.; Li, C. C. Recent advances of transition metal based bifunctional electrocatalysts for rechargeable zinc-air batteries. *J. Power Sources* **2020**, *477*, 228696. DOI: <https://doi.org/10.1016/j.jpowsour.2020.228696>.
- [149] Cano, Z. P.;Park, M. G.;Lee, D. U.;Fu, J.;Liu, H.;Fowler, M.; Chen, Z. New Interpretation of the Performance of Nickel-Based Air Electrodes for Rechargeable Zinc–Air Batteries. *J. Phys. Chem. C* **2018**, *122*, 20153-20166. DOI: [10.1021/acs.jpcc.8b06243](https://doi.org/10.1021/acs.jpcc.8b06243).
- [150] Ibrahim, K. B.;Tsai, M.-C.;Chala, S. A.;Berihun, M. K.;Kahsay, A. W.;Berhe, T. A.;Su, W.-N.; Hwang, B.-J. A review of transition metal-based bifunctional oxygen electrocatalysts. *J. Chin. Chem. Soc.* **2019**, *66*, 829-865. DOI: <https://doi.org/10.1002/jccs.201900001>.
- [151] Gao, Y.;Zhang, T.;Mao, Y.;Wang, J.; Sun, C. Highly efficient bifunctional layered triple Co, Fe, Ru hydroxides and oxides composite electrocatalysts for Zinc-Air batteries. *J. Electroanal. Chem.* **2023**, *935*, 117315. DOI: <https://doi.org/10.1016/j.jelechem.2023.117315>.

- [152] Wu, M.;Wei, Q.;Zhang, G.;Qiao, J.;Wu, M.;Zhang, J.;Gong, Q.; Sun, S. Fe/Co Double Hydroxide/Oxide Nanoparticles on N-Doped CNTs as Highly Efficient Electrocatalyst for Rechargeable Liquid and Quasi-Solid-State Zinc–Air Batteries. *Adv. Energy Mater.* **2018**, *8*, 1801836. DOI: <https://doi.org/10.1002/aenm.201801836>.
- [153] Mondal, S.;Majee, R.;Arif Islam, Q.; Bhattacharyya, S. 2D Heterojunction Between Double Perovskite Oxide Nanosheet and Layered Double Hydroxide to Promote Rechargeable Zinc-Air Battery Performance. *ChemElectroChem* **2020**, *7*, 5005-5012. DOI: <https://doi.org/10.1002/celc.202001412>.
- [154] Moloudi, M.;Noori, A.;Rahmanifar, M. S.;Shabangoli, Y.;El-Kady, M. F.;Mohamed, N. B.;Kaner, R. B.; Mousavi, M. F. Layered Double Hydroxide Templated Synthesis of Amorphous NiCoFeB as a Multifunctional Electrocatalyst for Overall Water Splitting and Rechargeable Zinc–Air Batteries. *Adv. Energy Mater.* **2023**, *13*, 2203002. DOI: <https://doi.org/10.1002/aenm.202203002>.
- [155] Li, S.;Yang, X.;Yang, S.;Gao, Q.;Zhang, S.;Yu, X.;Fang, Y.;Yang, S.; Cai, X. An amorphous trimetallic (Ni–Co–Fe) hydroxide-sheathed 3D bifunctional electrode for superior oxygen evolution and high-performance cable-type flexible zinc–air batteries. *J. Mater. Chem. A* **2020**, *8*, 5601-5611. DOI: [10.1039/d0ta00888e](https://doi.org/10.1039/d0ta00888e).
- [156] Zhou, Q.;Zhang, S.;Zhou, G.;Pang, H.;Zhang, M.;Xu, L.;Sun, K.;Tang, Y.; Huang, K. Interfacial Engineering of CoN/Co<sub>3</sub>O<sub>4</sub> Heterostructured Hollow Nanoparticles Embedded in N-Doped Carbon Nanowires as a Bifunctional Oxygen Electrocatalyst for Rechargeable Liquid and Flexible all-Solid-State Zn-Air Batteries. *Small* **2023**, *19*, 2301324. DOI: <https://doi.org/10.1002/smll.202301324>.
- [157] Zhu, J.;Xiao, M.;Li, G.;Li, S.;Zhang, J.;Liu, G.;Ma, L.;Wu, T.;Lu, J.;Yu, A.;Su, D.;Jin, H.;Wang, S.; Chen, Z. A Triphasic Bifunctional Oxygen Electrocatalyst with Tunable and Synergetic Interfacial Structure for Rechargeable Zn-Air Batteries. *Adv. Energy Mater.* **2020**, *10*, 1903003. DOI: <https://doi.org/10.1002/aenm.201903003>.
- [158] Chandrasekaran, S.;Yao, L.;Deng, L.;Bowen, C.;Zhang, Y.;Chen, S.;Lin, Z.;Peng, F.; Zhang, P. Recent advances in metal sulfides: from controlled fabrication to electrocatalytic, photocatalytic and photoelectrochemical water

- splitting and beyond. *Chem. Soc. Rev.* **2019**, *48*, 4178-4280. DOI: <https://doi.org/10.1039/C8CS00664D>
- [159] Li, W.;Wu, L.;Wu, X.;Shi, C.;Li, Y.;Zhang, L.;Mi, H.;Zhang, Q.;He, C.; Ren, X. Regulation and mechanism study of the CoS<sub>2</sub>/Cu<sub>2</sub>S-NF heterojunction as highly-efficient bifunctional electrocatalyst for oxygen reactions. *Appl. Catal. B: Environ.* **2022**, *303*, 120849. DOI: <https://doi.org/10.1016/j.apcatb.2021.120849>.
- [160] Yin, M.;Miao, H.;Dang, J.;Chen, B.;Zou, J.;Chen, G.; Li, H. High-performance alkaline hybrid zinc batteries with heterostructure nickel/cobalt sulfide. *J. Power Sources* **2022**, *545*, 231902. DOI: <https://doi.org/10.1016/j.jpowsour.2022.231902>.
- [161] Gui, L.;Huang, Z.;Ai, D.;He, B.;Zhou, W.;Sun, J.;Xu, J.;Wang, Q.; Zhao, L. Integrated Ultrafine Co0.85Se in Carbon Nanofibers: An Efficient and Robust Bifunctional Catalyst for Oxygen Electrocatalysis. *Chemistry – A European J.* **2020**, *26*, 4063-4069. DOI: <https://doi.org/10.1002/chem.201903616>.
- [162] Hong, X.;Xu, Y.;Wang, R.;Du, P.;Zhao, Z.;Huang, K.;Tang, H.;Liu, Y.;Lei, M.; Wu, H. Boosting the Performance of Nitrogen-Doped Mesoporous Carbon Oxygen Electrode with Ultrathin 2D Iron/Cobalt Selenides. *Adv. Mater. Interfaces* **2020**, *7*, 2000740. DOI: <https://doi.org/10.1002/admi.202000740>.
- [163] Pan, Q.-R.;Li, S.-J.;Tong, K.;Xie, C.;Peng, L.;Li, N.;Wang, D.-Y.; Su, H. Engineering Ni<sup>3+</sup> inside nickel selenide as efficient bifunctional oxygen electrocatalysts for Zn–air batteries. *J. Mater. Sci.* **2019**, *54*, 9063-9074. DOI: [10.1007/s10853-019-03520-w](https://doi.org/10.1007/s10853-019-03520-w).
- [164] Zheng, X.;Han, X.;Cao, Y.;Zhang, Y.;Nordlund, D.;Wang, J.;Chou, S.;Liu, H.;Li, L.;Zhong, C.;Deng, Y.; Hu, W. Identifying Dense NiSe<sub>2</sub>/CoSe<sub>2</sub> Heterointerfaces Coupled with Surface High-Valence Bimetallic Sites for Synergistically Enhanced Oxygen Electrocatalysis. *Adv. Mater.* **2020**, *32*, 2000607. DOI: <https://doi.org/10.1002/adma.202000607>.
- [165] Peng, L.-J.;Huang, J.-P.;Pan, Q.-R.;Liang, Y.;Yin, N.;Xu, H.-C.; Li, N. A simple method for the preparation of a nickel selenide and cobalt selenide mixed catalyst to enhance bifunctional oxygen activity for Zn–air batteries. *RSC Adv.* **2021**, *11*, 19406-19416. DOI: [10.1039/d1ra02861h](https://doi.org/10.1039/d1ra02861h).
- [166] Sun, C.;Ding, J.;Wang, H.;Liu, J.;Han, X.;Deng, Y.;Zhong, C.; Hu, W. Cobalt sulfides constructed heterogeneous interfaces decorated on N,S-codoped carbon

- nanosheets as a highly efficient bifunctional oxygen electrocatalyst. *J. Mater. Chem. A* **2021**, *9*, 13926-13935. DOI: 10.1039/d1ta02330f.
- [167] Peng, Y.;Zhang, F.;Zhang, Y.;Luo, X.;Chen, L.; Shi, Y. ZnS modified N, S dual-doped interconnected porous carbon derived from dye sludge waste as high-efficient ORR/OER catalyst for rechargeable zinc-air battery. *J. Colloid Interface Sci.* **2022**, *616*, 659-667. DOI: <https://doi.org/10.1016/j.jcis.2022.02.102>.
- [168] Shang, X.;Shen, Q.;Xiong, Y.;Jiang, Z.;Qin, C.;Tian, X.;Yang, X.; Jiang, Z.-J. Effect of Co-Fe alloy nanoparticles on the surface electronic structure of molybdenum disulfide nanosheets and its application as a bifunctional catalyst for rechargeable zinc air battery. *J. Alloys Compd.* **2022**, *916*, 165482. DOI: <https://doi.org/10.1016/j.jallcom.2022.165482>.
- [169] Cao, Y.;Zheng, X.;Zhang, H.;Zhang, J.;Han, X.;Zhong, C.;Hu, W.; Deng, Y. Interface engineering of NiS<sub>2</sub>/CoS<sub>2</sub> nanohybrids as bifunctional electrocatalysts for rechargeable solid state Zn-air battery. *J. Power Sources* **2019**, *437*, 226893. DOI: <https://doi.org/10.1016/j.jpowsour.2019.226893>.
- [170] Yue, L.;Liang, J.;Wu, Z.;Zhong, B.;Luo, Y.;Liu, Q.;Li, T.;Kong, Q.;Liu, Y.;Asiri, A. M.;Guo, X.; Sun, X. Progress and perspective of metal phosphide/carbon heterostructure anodes for rechargeable ion batteries. *J. Mater. Chem. A* **2021**, *9*, 11879-11907. DOI: 10.1039/d1ta01626a.
- [171] Du, J.;Zhang, F.;Wang, Z.;Shang, Y.;Zhou, L.;Fan, Y.;Yu, M.;Wang, Y.; Kang, D. J. Synthesis of binary metal phosphides heterostructures as a stable and efficient hydrogen evolution reaction electrocatalyst. *Mater. Today Commun.* **2020**, *25*, 101257. DOI: <https://doi.org/10.1016/j.mtcomm.2020.101257>.
- [172] Zhang, H.;Maijenburg, A. W.;Li, X.;Schweizer, S. L.; Wehrspohn, R. B. Bifunctional Heterostructured Transition Metal Phosphides for Efficient Electrochemical Water Splitting. *Adv. Funct. Mater.* **2020**, *30*, 2003261. DOI: <https://doi.org/10.1002/adfm.202003261>.
- [173] Xu, X.;Wang, X.;Huo, S.;Liu, X.;Ma, X.;Liu, M.; Zou, J. Modulation of Phase Transition in Cobalt Selenide with Simultaneous Construction of Heterojunctions for Highly-Efficient Oxygen Electrocatalysis in Zinc–Air Battery. *Adv. Mater.* **2024**, *36*, 2306844. DOI: <https://doi.org/10.1002/adma.202306844>.

- [174] Lian, Y.;Yu, T.;Qu, Y.;Yuan, C.;Lu, Z.-H.; Guo, M. Interface Electronic Modulation of Monodispersed Co Metal-Co<sub>7</sub>Fe<sub>3</sub> Alloy Heterostructures for Rechargeable Zn–Air Battery. *Ind. Eng. Chem. Res.* **2024**, *63*, 1369-1379. DOI: 10.1021/acs.iecr.3c03149.
- [175] Shi, Q.;Zheng, Y.;Li, W.;Tang, B.;Qin, L.;Yang, W.; Liu, Q. A rationally designed bifunctional oxygen electrocatalyst based on Co<sub>2</sub>P nanoparticles for Zn–air batteries. *Catal. Sci. Technol.* **2020**, *10*, 5060-5068. DOI: 10.1039/d0cy01012j.
- [176] Bo, L.;Liu, W.;Liu, R.;Hu, Y.;Pu, L.;Nian, F.;Zhang, Z.;Li, P.; Tong, J. CoP/Co<sub>2</sub>P hollow spheres embedded in porous N-doped carbon as highly efficient multifunctional electrocatalyst for Zn–air battery driving water splitting device. *Electrochim. Acta* **2022**, *403*, 139643. DOI: <https://doi.org/10.1016/j.electacta.2021.139643>.
- [177] Sun, X.;Liang, H.;Yu, H.;Bai, J.; Li, C. Embedding Co<sub>2</sub>P nanoparticles in Cu doping carbon fibers for Zn–air batteries and supercapacitors. *Nanotechnology* **2022**, *33*, 135202. DOI: 10.1088/1361-6528/ac43ea.
- [178] Liu, Y.;Li, C.;Yuan, M.;Zhang, X.;Lan, H.;Chen, Y.;Tian, M.;Liu, K.; Wang, L. Tunable phosphorization degree of CoxPy@N,P-doped carbon as a highly-active bifunctional electrocatalyst for rechargeable zinc–air batteries. *Catal. Sci. Technol.* **2023**, *13*, 3084-3093. DOI: 10.1039/d3cy00287j.
- [179] Wang, Y.;Liu, J.;Lu, T.;He, R.;Xu, N.; Qiao, J. Ultra-high voltage efficiency rechargeable zinc-air battery based on high-performance structurally regulated metal-rich nickel phosphides and carbon hybrids bifunctional electrocatalysts. *Appl. Catal. B: Environ.* **2023**, *321*, 122041. DOI: <https://doi.org/10.1016/j.apcatb.2022.122041>.
- [180] Thakur, N.;Kumar, M.;Mandal, D.; Nagaiah, T. C. Nickel Iron Phosphide/Phosphate as an Oxygen Bifunctional Electrocatalyst for High-Power-Density Rechargeable Zn–Air Batteries. *ACS Appl. Mater. Interfaces*. **2021**, *13*, 52487-52497. DOI: 10.1021/acsami.1c12053.
- [181] Gao, L.;Chang, S.; Zhang, Z. High-Quality CoFeP Nanocrystal/N, P Dual-Doped Carbon Composite as a Novel Bifunctional Electrocatalyst for Rechargeable Zn–Air Battery. *ACS Appl. Mater. Interfaces*. **2021**, *13*, 22282-22291. DOI: 10.1021/acsami.1c00484.

- [182] Ahn, S. H.; Manthiram, A. Cobalt Phosphide Coupled with Heteroatom-Doped Nanocarbon Hybrid Electroctalysts for Efficient, Long-Life Rechargeable Zinc–Air Batteries. *Small* **2017**, *13*, 1702068. DOI: <https://doi.org/10.1002/smll.201702068>.
- [183] Chandrasekaran, S.; Ma, T.; Hu, Z.; Liu, Q.; Zhan, C.; Li, Y.; Bowen, C.; Lu, H.; Liu, Y. Delocalization of d-electrons induced by cation coupling in ultrathin Chevrel-phase NiMo<sub>3</sub>S<sub>4</sub> nanosheets for efficient electrochemical water splitting. *Appl. Catal. B: Environ.* **2023**, *338*, 123007. DOI: <https://doi.org/10.1016/j.apcatb.2023.123007>.
- [184] Wu, Y.-j.; Wu, X.-h.; Tu, T.-x.; Zhang, P.-f.; Li, J.-t.; Zhou, Y.; Huang, L.; Sun, S.-g. Controlled synthesis of FeNx-CoNx dual active sites interfaced with metallic Co nanoparticles as bifunctional oxygen electrocatalysts for rechargeable Zn-air batteries. *Appl. Catal. B: Environ.* **2020**, *278*, 119259. DOI: <https://doi.org/10.1016/j.apcatb.2020.119259>.
- [185] Ruan, Y.; Lei, H.; Xue, W.; Wang, T.; Song, S.; Xu, H.; Yu, Y.; Zhang, G.-R.; Mei, D. Cu-N-C assisted MnO nanorods as bifunctional electrocatalysts for superior long-cycle Zn-air batteries. *J. Alloys Compd.* **2023**, *934*, 167781. DOI: <https://doi.org/10.1016/j.jallcom.2022.167781>.
- [186] Lee, K.; Duan, X.; Hersam, M. C.; Kim, J. Fundamentals and applications of mixed-dimensional heterostructures. *APL Materials* **2022**, *10*. DOI: 10.1063/5.0097804 (acccessed 12/5/2023)
- [187] Jariwala, D.; Marks, T. J.; Hersam, M. C. Mixed-dimensional van der Waals heterostructures. *Nat. Mater.* **2017**, *16*, 170-181. DOI: 10.1038/nmat4703.
- [188] Lu, Q.; Wu, H.; Zheng, X.; Cao, Y.; Li, J.; Wang, Y.; Wang, H.; Zhi, C.; Deng, Y.; Han, X. Controllable constructing janus homologous heterostructures of transition metal alloys/sulfides for efficient oxygen electrocatalysis. *Adv. Energy Mater.* **2022**, *12*, 2202215. DOI: <https://doi.org/10.1002/aenm.202202215>.
- [189] Hu, H.; Wang, X.; Attfield, J. P.; Yang, M. Metal nitrides for seawater electrolysis. *Chem. Soc. Rev.* **2024**, *53*, 163-203. DOI: <https://doi.org/10.1039/D3CS00717K>
- [190] Huang, Y.; Liu, Y.; Deng, Y.; Zhang, J.; He, B.; Sun, J.; Yang, Z.; Zhou, W.; Zhao, L. Enhancing the bifunctional activity of CoSe<sub>2</sub> nanocubes by surface

- decoration of CeO<sub>2</sub> for advanced zinc-air batteries. *J. Colloid Interface Sci.* **2022**, *625*, 839-849. DOI: <https://doi.org/10.1016/j.jcis.2022.06.094>.
- [191] Zhang, Y.; Ma, J.; Ma, M.; Zhang, C.; Jia, X.; Wang, G. Co and Co<sub>9</sub>S<sub>8</sub> nanoparticles uniformly embedded in S, N-doped porous carbon as electrocatalysts for rechargeable zinc-air batteries. *J. Mater. Res.* **2022**, *18*, 3764-3776. DOI: <https://doi.org/10.1016/j.jmrt.2022.04.048>.
- [192] Zhang, Y.; Shi, W.; Bo, L.; Shen, Y.; Ji, X.; Xia, L.; Guan, X.; Wang, Y.; Tong, J. Electrospinning construction of heterostructural Co<sub>3</sub>W<sub>3</sub>C/CoP nanoparticles embedded in N, P-doped hierarchically porous carbon fibers as excellent multifunctional electrocatalyst for Zn-air batteries and water splitting. *Chem. Eng. J.* **2022**, *431*, 134188. DOI: <https://doi.org/10.1016/j.cej.2021.134188>.
- [193] Yang, H.; Wang, B.; Kou, S.; Lu, G.; Liu, Z. Mott-Schottky heterojunction of Co/Co<sub>2</sub>P with built-in electric fields for bifunctional oxygen electrocatalysis and zinc-air battery. *Chem. Eng. J.* **2021**, *425*, 131589. DOI: <https://doi.org/10.1016/j.cej.2021.131589>.
- [194] Tian, W.-W.; Ren, J.-T.; Lv, X.-W.; Gao, L.-J.; Yuan, Z.-Y. In Situ Sulfidation for Controllable Heterointerface of Cobalt Oxides–Cobalt Sulfides on 3D Porous Carbon Realizing Efficient Rechargeable Liquid-/Solid-State Zn–Air Batteries. *ACS Sustain. Chem. Eng.* **2021**, *9*, 510-520. DOI: [10.1021/acssuschemeng.0c07890](https://doi.org/10.1021/acssuschemeng.0c07890).
- [195] Huang, J.; Luo, Q.; Zou, J.; Zeng, X.; Chen, B.; Wu, H.; Tang, Q. Electrostatic spun hierarchically porous carbon matrix with CoSe<sub>2</sub>/Co heterostructure as bifunctional electrocatalysts for zinc-air batteries. *J. Alloys Compd.* **2021**, *875*, 160056. DOI: <https://doi.org/10.1016/j.jallcom.2021.160056>.
- [196] Hu, T.; Jiang, Z.; Fu, Z.; Jiang, Z.-J. A NiFe/NiSe<sub>2</sub> heterojunction bifunctional catalyst rich in oxygen vacancies introduced using dielectric barrier discharge plasma for liquid and flexible all-solid-state rechargeable Zn–air batteries. *J Mater Chem A* **2022**, *10*, 8739-8750. DOI: [10.1039/d2ta00949h](https://doi.org/10.1039/d2ta00949h).
- [197] Wang, Y.; Wu, X.; Jiang, X.; Wu, X.; Tang, Y.; Sun, D.; Fu, G. Citrulline-induced mesoporous CoS/CoO heterojunction nanorods triggering high-efficiency oxygen electrocatalysis in solid-state Zn-air batteries. *Chem. Eng. J.* **2022**, *434*, 134744. DOI: <https://doi.org/10.1016/j.cej.2022.134744>.
- [198] Yang, T.; Hu, X.; Zheng, W.; Li, Z.; Wu, D.; Lu, G.; Zhao, Q.; Yang, Z.; Wang, R.; Xu, C. Rational Design of an FeCo<sub>2</sub>O<sub>4</sub>@FeCo<sub>2</sub>S<sub>4</sub> Heterostructure as an

- Efficient Bifunctional Electrocatalyst for Zn–Air Batteries. *ACS Appl. Energy Mater.* **2022**, *5*, 9742–9749. DOI: 10.1021/acsaem.2c01417.
- [199] Go, H. W.; Nguyen, T. T.; Ngo, Q. P.; Chu, R.; Kim, N. H.; Lee, J. H. Tailored Heterojunction Active Sites for Oxygen Electrocatalyst Promotion in Zinc-Air Batteries. *Small* **2023**, *19*, 2206341. DOI: <https://doi.org/10.1002/smll.202206341>.
- [200] Wei, Y.; Xia, H.; Lan, H.; Xue, D.; Zhao, B.; Yu, Y.; Hu, Y.; Zhang, J.-N. Boosting the Catalytic Activity of Nitrogen Sites by Spin Polarization Engineering for Oxygen Reduction and Wide-Temperature Ranged Quasi-Solid Zn–Air Batteries. *Adv. Energy Mater.* **2024**, *14*, 2303011. DOI: <https://doi.org/10.1002/aenm.202303011>.
- [201] Li, S.; Zhou, Y.; Xu, C.; Wang, L.; Wang, T.; Zhu, B.; Xu, W.; Wu, Y. A.; Tao, H. ZIFs-Derived Hollow Nanostructures via a Strong/Weak Coetching Strategy for Long-Life Rechargeable Zn–Air Batteries. *Small*, **2024**, 2309932. DOI: <https://doi.org/10.1002/smll.202309932>.
- [202] Wang, B.; Chen, Y.; Liu, G.; Liu, D.; Liu, Y.; Ge, C.; Wang, L.; Wang, Z.; Wu, R.; Wang, L. Interfaces coupling of Co<sub>8</sub>FeS<sub>8</sub>-Fe<sub>5</sub>C<sub>2</sub> with elevated d-band center for efficient water oxidation catalysis. *Appl. Catal. B: Environ.* **2024**, *341*, 123294. DOI: <https://doi.org/10.1016/j.apcatb.2023.123294>.
- [203] Zheng, J.; Hu, G.; Liu, B.; Liu, Y.; Li, H.; Zhao, H.; Yang, M. In-situ spatial-embedding construction of FeCo nucleus-bound carbon skeletons for durable rechargeable liquid and flexible Zn-air batteries. *Energy Storage Mater.* **2024**, *65*, 103106. DOI: <https://doi.org/10.1016/j.ensm.2023.103106>.
- [204] Jin, T.; Nie, J.; Dong, M.; Chen, B.; Nie, J.; Ma, G. 3D Interconnected Honeycomb-Like Multifunctional Catalyst for Zn–Air Batteries. *Nano-Micro Lett.* **2022**, *15*, 26. DOI: 10.1007/s40820-022-00959-6.
- [205] Zhao, Q.; Pan, Z.; Liu, B.; Bao, C.; Liu, X.; Sun, J.; Xie, S.; Wang, Q.; Wang, J.; Gao, Y. Electrochromic-Induced Rechargeable Aqueous Batteries: An Integrated Multifunctional System for Cross-Domain Applications. *Nano-Micro Lett.* **2023**, *15*, 87. DOI: 10.1007/s40820-023-01056-y.
- [206] Yu, J.; Dai, Y.; Zhang, Z.; Liu, T.; Zhao, S.; Cheng, C.; Tan, P.; Shao, Z.; Ni, M. Tailoring structural properties of carbon via implanting optimal co nanoparticles in n-rich carbon cages toward high-efficiency oxygen

- electrocatalysis for rechargeable zn-air batteries. *Carbon Energy* **2022**, *4*, 576-585. DOI: <https://doi.org/10.1002/cey2.171>.
- [207] Xu, X.;Xie, J.;Liu, B.;Wang, R.;Liu, M.;Zhang, J.;Liu, J.;Cai, Z.;Zou, J. PBA-derived FeCo alloy with core-shell structure embedded in 2D N-doped ultrathin carbon sheets as a bifunctional catalyst for rechargeable Zn-air batteries. *Appl. Catal. B: Environ.* **2022**, *316*, 121687. DOI: <https://doi.org/10.1016/j.apcatb.2022.121687>.
- [208] Chen, D.;Zhu, J.;Mu, X.;Cheng, R.;Li, W.;Liu, S.;Pu, Z.;Lin, C.; Mu, S. Nitrogen-Doped carbon coupled FeNi<sub>3</sub> intermetallic compound as advanced bifunctional electrocatalyst for OER, ORR and zn-air batteries. *Appl. Catal. B: Environ.* **2020**, *268*, 118729. DOI: <https://doi.org/10.1016/j.apcatb.2020.118729>.
- [209] Kim, K.;Min, K.;Go, Y.;Lee, Y.;Shim, S. E.;Lim, D.;Baeck, S.-H. FeCo alloy nanoparticles embedded in N-doped carbon supported on highly defective ketjenblack as effective bifunctional electrocatalysts for rechargeable Zn-air batteries. *Appl. Catal. B: Environ.* **2022**, *315*, 121501. DOI: <https://doi.org/10.1016/j.apcatb.2022.121501>.
- [210] Zhao, D.;Zhang, L.;Zuo, S.;Lv, X.;Zhao, M.;Sun, P.;Sun, X.; Liu, T. L. Developing Superior Hydrophobic 3D Hierarchical Electrocatalysts Embedding Abundant Catalytic Species for High Power Density Zn–Air Battery. *Small* **2023**, *19*, 2206067. DOI: <https://doi.org/10.1002/smll.202206067>.
- [211] Vijayakumar, E.;Ramakrishnan, S.;Sathiskumar, C.;Yoo, D. J.;Balamurugan, J.;Noh, H. S.;Kwon, D.;Kim, Y. H.; Lee, H. MOF-derived CoP-nitrogen-doped carbon@NiFeP nanoflakes as an efficient and durable electrocatalyst with multiple catalytically active sites for OER, HER, ORR and rechargeable zinc-air batteries. *Chem. Eng. J.* **2022**, *428*, 131115. DOI: <https://doi.org/10.1016/j.cej.2021.131115>.
- [212] Li, W.;Wang, J.;Chen, J.;Chen, K.;Wen, Z.; Huang, A. Core–Shell Carbon-Based Bifunctional Electrocatalysts Derived from COF@MOF Hybrid for Advanced Rechargeable Zn–Air Batteries. *Small* **2022**, *18*, 2202018. DOI: <https://doi.org/10.1002/smll.202202018>.

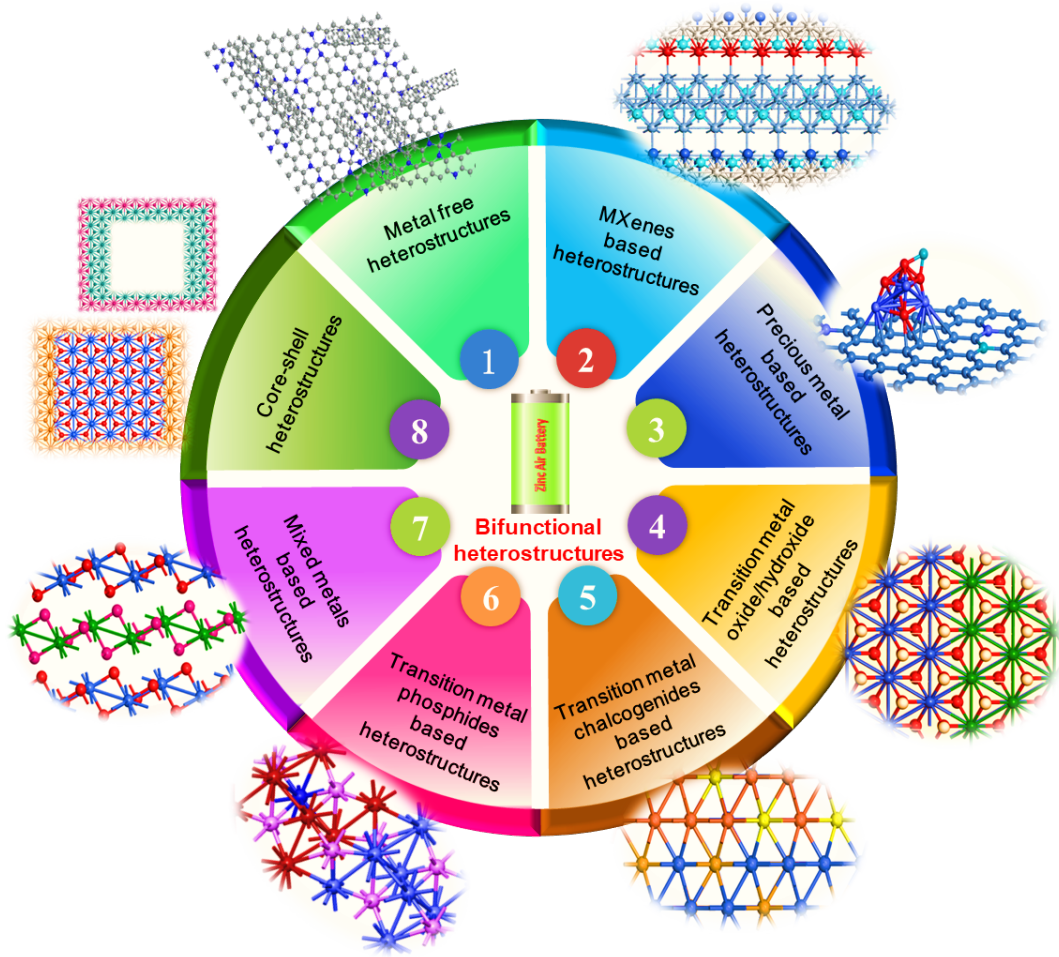
- [213] Rai, P.;Majhi, S. M.;Yu, Y.-T.; Lee, J.-H. Noble metal@metal oxide semiconductor core@shell nano-architectures as a new platform for gas sensor applications. *RSC Adv.* **2015**, *5*, 76229-76248. DOI: 10.1039/c5ra14322e.
- [214] Paudel, D. R.;Pan, U. N.;Ghising, R. B.;Dhakal, P. P.;Dinh, V. A.;Wang, H.;Kim, N. H.;Lee, J. H. Interface modulation induced by the 1T Co-WS<sub>2</sub> shell nanosheet layer at the metallic NiTe<sub>2</sub>/Ni core–nanoskeleton: Glib electrode-kinetics for HER, OER, and ORR. *Nano Energy* **2022**, *102*, 107712. DOI: <https://doi.org/10.1016/j.nanoen.2022.107712>.
- [215] Konkena, B.;Masa, J.;Botz, A. J. R.;Sinev, I.;Xia, W.;Koßmann, J.;Drautz, R.;Muhler, M.; Schuhmann, W. Metallic NiPS<sub>3</sub>@NiOOH Core–Shell Heterostructures as Highly Efficient and Stable Electrocatalyst for the Oxygen Evolution Reaction. *ACS Catal.* **2017**, *7*, 229-237. DOI: 10.1021/acscatal.6b02203.
- [216] Ma, M.;Sun, W.;Wang, Y.;Wang, J.;Ma, L.; Yang, Q. Low-temperature liquid reflux synthesis of core@shell structured Ni@Fe-doped NiCo nanoparticles decorated on carbon nanotubes as a bifunctional electrocatalyst for Zn–air batteries. *J. Mater. Chem. A* **2022**, *10*, 13088-13096. DOI: 10.1039/d2ta03047k.
- [217] Yan, Y.;Liang, S.;Wang, X.;Zhang, M.;Hao, S.-M.;Cui, X.;Li, Z.; Lin, Z. Robust wrinkled MoS<sub>2</sub>/N-C bifunctional electrocatalysts interfaced with single Fe atoms for wearable zinc-air batteries. *Proc. Natl. Acad. Sci.* **2021**, *118*, e2110036118. DOI: doi:10.1073/pnas.2110036118.
- [218] Wang, H.;Kou, R.-H.;Jin, Q.;Liu, Y.-Z.;Yin, F.-X.;Sun, C.-J.;Wang, L.;Ma, Z.-Y.;Ren, Y.;Liu, N.; Chen, B.-H. Boosting the Oxygen Reduction Performance via Tuning the Synergy between Metal Core and Oxide Shell of Metal–Organic Frameworks-Derived Co@CoOx. *ChemElectroChem* **2020**, *7*, 1590-1597. DOI: <https://doi.org/10.1002/celc.202000038>.
- [219] Pan, H.;Cao, Y.;Zhang, B.;Han, J.;Bai, Y.;Shang, X.;Jiang, Z.;Tian, X.; Jiang, Z.-J. Amino functionalized carbon nanotubes supported CoNi@CoO–NiO core/shell nanoparticles as highly efficient bifunctional catalyst for rechargeable Zn-air batteries. *Int. J. Hydrog. Energy* **2021**, *46*, 374-388. DOI: <https://doi.org/10.1016/j.ijhydene.2020.09.174>.
- [220] Nguyen, D. C.;Tran, D. T.;Doan, T. L. L.;Kim, D. H.;Kim, N. H.; Lee, J. H. Rational Design of Core@shell Structured CoS<sub>x</sub>@Cu<sub>2</sub>MoS<sub>4</sub> Hybridized MoS<sub>2</sub>/N,S-Codoped Graphene as Advanced Electrocatalyst for Water Splitting

- and Zn-Air Battery. *Adv. Energy Mater.* **2020**, *10*, 1903289. DOI: <https://doi.org/10.1002/aenm.201903289>.
- [221] Chen, K.; Wang, X.; Zhang, C.; Xu, R.; Wang, H.; Chu, L.; Huang, M. Three-phases Co/Co<sub>9</sub>S<sub>8</sub>/MnS heterostructures engineering for boosted ORR/OER activities in Zn-air batteries. *Mater. Today Energy* **2022**, *30*, 101150. DOI: <https://doi.org/10.1016/j.mtener.2022.101150>.
- [222] Xie, M.; Zhou, Y.; Wang, Z.; Wang, H.; Yan, D.; Han, B.; Zhang, S.; Deng, C. Heterostructured hollow fibers stitched together from nickel sulfides capped S, N-codoped carbon nanotubes as a trifunctional electrode for flexible hybrid Zn batteries. *Chem. Eng. J.* **2022**, *431*, 133920. DOI: <https://doi.org/10.1016/j.cej.2021.133920>.
- [223] Mai, L.; Sheng, J.; Xu, L.; Tan, S.; Meng, J. One-Dimensional Hetero-Nanostructures for Rechargeable Batteries. *Acc. Chem. Res.* **2018**, *51*, 950-959. DOI: 10.1021/acs.accounts.8b00031.
- [224] Wang, P.; Li, C.; Dong, S.; Ge, X.; Zhang, P.; Miao, X.; Wang, R.; Zhang, Z.; Yin, L. Hierarchical NiCo<sub>2</sub>S<sub>4</sub>@NiO Core–Shell Heterostructures as Catalytic Cathode for Long-Life Li-O<sub>2</sub> Batteries. *Adv. Energy Mater.* **2019**, *9*, 1900788. DOI: <https://doi.org/10.1002/aenm.201900788>.
- [225] Ding, D.; Shen, K.; Chen, X.; Chen, H.; Chen, J.; Fan, T.; Wu, R.; Li, Y. Multi-Level Architecture Optimization of MOF-Templated Co-Based Nanoparticles Embedded in Hollow N-Doped Carbon Polyhedra for Efficient OER and ORR. *ACS Catal.* **2018**, *8*, 7879-7888. DOI: 10.1021/acscatal.8b02504.
- [226] Wang, R.; Liu, J.; Xie, J.; Cai, Z.; Yu, Y.; Zhang, Z.; Meng, X.; Wang, C.; Xu, X.; Zou, J. Hollow nanocage with skeleton Ni-Fe sulfides modified by N-doped carbon quantum dots for enhancing mass transfer for oxygen electrocatalysis in zinc-air battery. *Appl. Catal. B: Environ.* **2023**, *324*, 122230. DOI: <https://doi.org/10.1016/j.apcatb.2022.122230>.
- [227] Liu, Z.-Q.; Liang, X.; Ma, F.-X.; Xiong, Y.-X.; Zhang, G.; Chen, G.; Zhen, L.; Xu, C.-Y. Decoration of NiFe-LDH Nanodots Endows Lower Fe-d Band Center of Fe<sub>1</sub>-N-C Hollow Nanorods as Bifunctional Oxygen Electrocatalysts with Small Overpotential Gap. *Adv. Energy Mater.* **2023**, *13*, 2203609. DOI: <https://doi.org/10.1002/aenm.202203609>.
- [228] Xie, W. W.; Tian, T. Z.; Yang, M.; Li, N. W.; Yu, L. Formation of hollow frameworks of dual-sided Fe/Fe<sub>3</sub>C@N-doped carbon nanotubes as bifunctional

- oxygen electrocatalyst for Zn-air batteries. *Appl. Catal. B: Environ.* **2022**, *317*, 121760. DOI: <https://doi.org/10.1016/j.apcatb.2022.121760>.
- [229] Wagh, N. K.;Shinde, S. S.;Lee, C. H.;Jung, J.-Y.;Kim, D.-H.;Kim, S.-H.;Lin, C.;Lee, S. U.; Lee, J.-H. Densely colonized isolated Cu-N single sites for efficient bifunctional electrocatalysts and rechargeable advanced Zn-air batteries. *Appl. Catal. B: Environ.* **2020**, *268*, 118746. DOI: <https://doi.org/10.1016/j.apcatb.2020.118746>.
- [230] Go, Y.;Min, K.;An, H.;Kim, K.;Eun Shim, S.; Baeck, S.-H. Oxygen-vacancy-rich CoFe/CoFe<sub>2</sub>O<sub>4</sub> embedded in N-doped hollow carbon spheres as a highly efficient bifunctional electrocatalyst for Zn–air batteries. *Chem. Eng. J.* **2022**, *448*, 137665. DOI: <https://doi.org/10.1016/j.cej.2022.137665>.
- [231] Butera, V. Density functional theory methods applied to homogeneous and heterogeneous catalysis: a short review and a practical user guide. *Phys. Chem. Chem. Phys.* **2024**, *26*, 7950-7970. DOI: <https://doi.org/10.1039/D4CP00266K>.
- [232] Liang, W.;Chen, J.;Liu, Y.; Chen, S. Density-Functional-Theory Calculation Analysis of Active Sites for Four-Electron Reduction of O<sub>2</sub> on Fe/N-Doped Graphene. *ACS Catal.* **2014**, *4*, 4170-4177. DOI: <https://doi.org/10.1021/cs501170a>.
- [233] Liu, J.;Liu, H.;Chen, H.;Du, X.;Zhang, B.;Hong, Z.;Sun, S.; Wang, W. Progress and Challenges Toward the Rational Design of Oxygen Electrocatalysts Based on a Descriptor Approach. *Adv. Sci.* **2020**, *7*, 1901614. DOI: <https://doi.org/10.1002/advs.201901614>.
- [234] Sameera, W. M. C.; Maseras, F. Transition metal catalysis by density functional theory and density functional theory/molecular mechanics. *Wiley Interdiscip. Rev. Comput. Mol. Sci.* **2012**, *2*, 375-385. DOI: <https://doi.org/10.1002/wcms.1092>
- [235] Liao, X.;Lu, R.;Xia, L.;Liu, Q.;Wang, H.;Zhao, K.;Wang, Z.; Zhao, Y. Density Functional Theory for Electrocatalysis. *Energy Environ. Mater.* **2022**, *5*, 157-185. DOI: <https://doi.org/10.1002/eem2.12204>
- [236] Zhang, P.;Yang, Y.;Duan, X.;Liu, Y.; Wang, S. Density Functional Theory Calculations for Insight into the Heterocatalyst Reactivity and Mechanism in Persulfate-Based Advanced Oxidation Reactions. *ACS Catal.* **2021**, *11*, 11129-11159. DOI: <https://doi.org/10.1021/acscatal.1c03099>.

- [237] Deng, D.;Novoselov, K. S.;Fu, Q.;Zheng, N.;Tian, Z.; Bao, X. Catalysis with two-dimensional materials and their heterostructures. *Nat. Nanotech.* **2016**, *11*, 218-230. DOI: <https://doi.org/10.1038/nnano.2015.340>
- [238] Li, Y.;Zhang, J.;Chen, Q.;Xia, X.; Chen, M. Emerging of Heterostructure Materials in Energy Storage: A Review. *Adv. Mater.* **2021**, *33*, 2100855. DOI: <https://doi.org/10.1002/adma.202100855>.
- [239] Zhao, X.;Liu, M.;Wang, Y.;Xiong, Y.;Yang, P.;Qin, J.;Xiong, X.; Lei, Y. Designing a Built-In Electric Field for Efficient Energy Electrocatalysis. *ACS Nano* **2022**, *16*, 19959-19979. DOI: <https://doi.org/10.1021/acsnano.2c09888>.
- [240] Hu, X.;Fan, J.;Wang, R.;Li, M.;Sun, S.;Xu, C.; Pan, F. Vacancies and interfaces engineering of core–shell heterostuctured NiCoP/NiO as trifunctional electrocatalysts for overall water splitting and zinc-air batteries. *Green Energy Environ.* **2023**, *8*, 601-611. DOI: <https://doi.org/10.1016/j.gee.2021.11.003>.
- [241] Li, J.;Kang, Y.;Lei, Z.; Liu, P. Well-controlled 3D flower-like CoP<sub>3</sub>/CeO<sub>2</sub>/C heterostructures as bifunctional oxygen electrocatalysts for rechargeable Zn-air batteries. *Appl. Catal. B: Environ.* **2023**, *321*, 122029. DOI: <https://doi.org/10.1016/j.apcatb.2022.122029>.
- [242] Hammer, B.; Nørskov, J. K. Theoretical surface science and catalysis—calculations and concepts. In *Advances in Catalysis*. Academic Press, 2000; pp 71-129. DOI: [https://doi.org/10.1016/S0360-0564\(02\)45013-4](https://doi.org/10.1016/S0360-0564(02)45013-4).
- [243] Lamas, E. J.; Balbuena, P. B. Oxygen Reduction on Pd0.75Co0.25 (111) and Pt0.75Co0.25 (111) Surfaces: An ab Initio Comparative Study. *J. Chem. Theory Comput.* **2006**, *2*, 1388-1394. DOI: <https://doi.org/10.1021/ct6002059>
- [244] Shi, Z.;Yang, W.;Gu, Y.;Liao, T.; Sun, Z. Metal-Nitrogen-Doped Carbon Materials as Highly Efficient Catalysts: Progress and Rational Design. *Adv. Sci.* **2020**, *7*, 2001069. DOI: <https://doi.org/10.1002/advs.202001069>.
- [245] Sun, S.;Zhang, Y.;Shi, X.;Sun, W.;Felser, C.;Li, W.; Li, G. From Charge to Spin: An In-Depth Exploration of Electron Transfer in Energy Electrocatalysis. *Adv. Mater.*, **2024**, 2312524. DOI: <https://doi.org/10.1002/adma.202312524>.
- [246] Xu, L.;Wu, S.;He, X.;Wang, H.;Deng, D.;Wu, J.; Li, H. Interface Engineering of Anti-Perovskite Ni<sub>3</sub>FeN/VN Heterostructure for High-Performance Rechargeable Zinc–Air batteries. *Chem. Eng. J.* **2022**, *437*, 135291. DOI: <https://doi.org/10.1016/j.cej.2022.135291>.

- [247] Xu, X.;Liu, M.;Nie, Y.;Wang, C.;Wang, W.;Liu, C.;Wang, X.;Cai, Z.;Liu, X.;Huo, S.;Liu, B.;Zou, J. Modulating electronic structure of interfacial Fe sites in Fe<sub>2</sub>N/CoFe<sub>2</sub>O<sub>4</sub> nano-heterostructure for enhancing corrosion-resistance and oxygen electrocatalysis in zinc-air battery. *Chem. Eng. J.* **2023**, *471*, 144639. DOI: <https://doi.org/10.1016/j.cej.2023.144639>.
- [248] Wang, B.; Zhang, F. Main Descriptors To Correlate Structures with the Performances of Electrocatalysts. *Angew. Chem. Int. Ed.* **2022**, *61*, e202111026. DOI: <https://doi.org/10.1002/anie.202111026>.
- [249] Maiti, S.;Maiti, K.;Curnan, M. T.;Kim, K.;Noh, K.-J.; Han, J. W. Engineering electrocatalyst nanosurfaces to enrich the activity by inducing lattice strain. *Energy Environ. Sci.* **2021**, *14*, 3717-3756. DOI: <https://doi.org/10.1039/D1EE00074H>.



**Scheme 1.** Schematic of hetero-interfacial engineering strategies for fabricating robust heterostructured bifunctional oxygen electrocatalysts for rechargeable zinc-air batteries (ZABs).

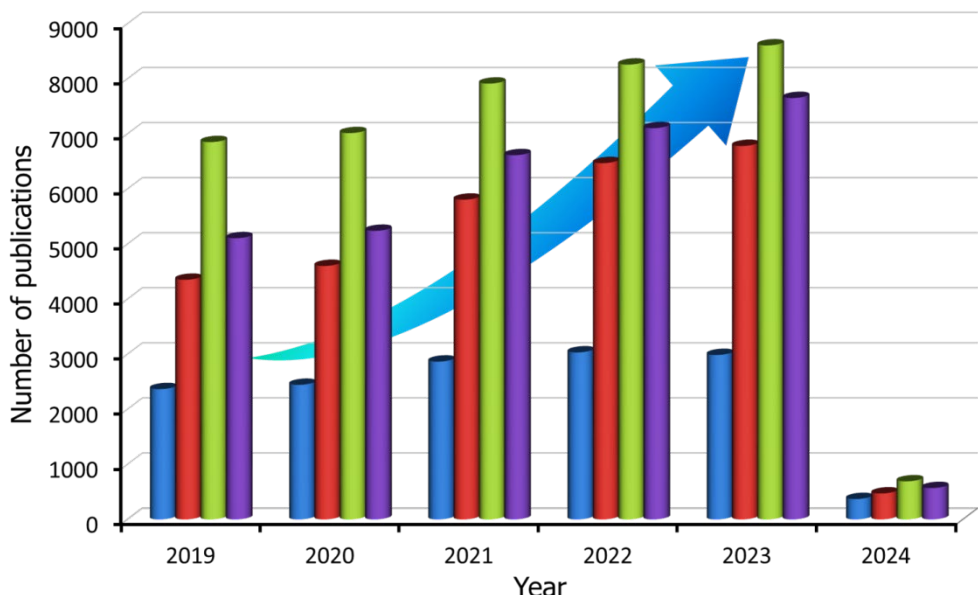


**Figure 1.** Bar chart illustrating number of articles published on traditional catalysts for bifunctional electrocatalytic ORR/OER reactions (blue bars), heterostructured catalysts for bifunctional electrocatalytic ORR/OER reactions with rechargeable zinc-air batteries (ZAB) uses (red bars), and those related to electrocatalysts for ORR (green bars) and electrocatalysts for OER reactions (purple bars). Data for traditional and/or heterostructured bifunctional electrocatalysis were attained by searching keywords “(“bifunctional oxygen electrocatalyst”) OR (“ORR/OER”) OR (“interface engineered bifunctional oxygen electrocatalyst”) OR (“heterostructured bifunctional oxygen electrocatalyst”) OR (“heterostructure + rechargeable ZABs”) AND (“heterostructure + ZABs”)” OR “(“oxygen reduction reaction and ZABs”) OR (“oxygen evolution reaction”) OR (“OER”)” as keywords. Web of Science Core Collection was used to search the entire dataset.

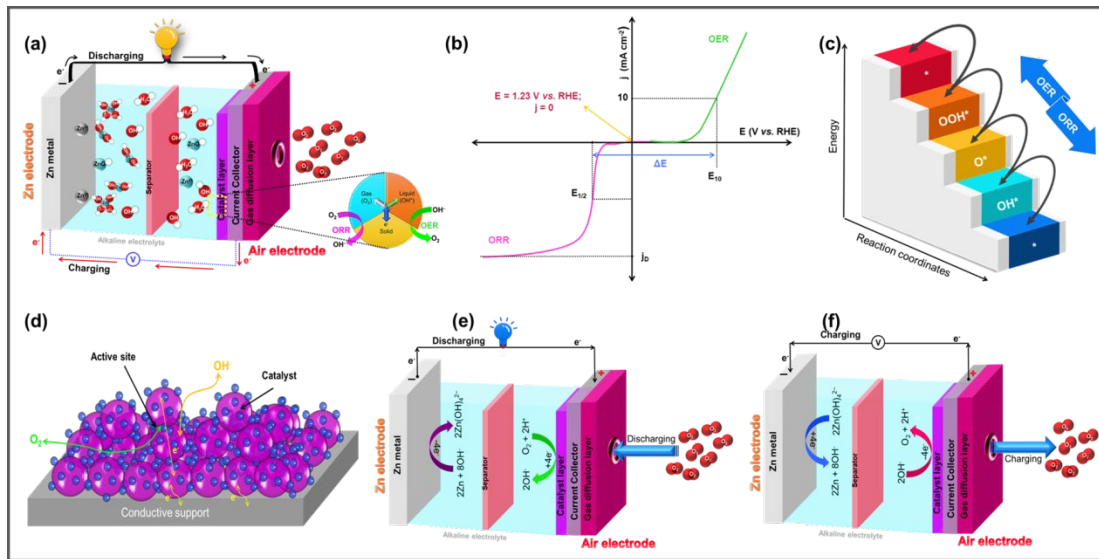


**Figure 2.** Basic configuration of a rechargeable Zn–air battery (ZABs) and schematic of surface/interface nanoengineering in terms of four key parameters, including surface reaction area, reaction energy barrier, electron conductivity, and mass transfer of the electrocatalysts and air electrode. (b-c) Electrocatalytic ORR and OER reactions and their energetics of oxygen redox intermediates during the bifunctional catalytic process. It is worth noting that the Gibbs free energy diagrams of different catalysts at different potentials/reaction conditions may vary. (d) Characteristic structural features of the heterostructured O<sub>2</sub> electrocatalysts for ORR and OER. (e-f) Discharging and charging process in rechargeable ZAB, respectively.



**Scheme 2.** Strategies on interfacial engineering of bifunctional oxygen electrocatalysts for rechargeable zinc-air batteries (ZABs).

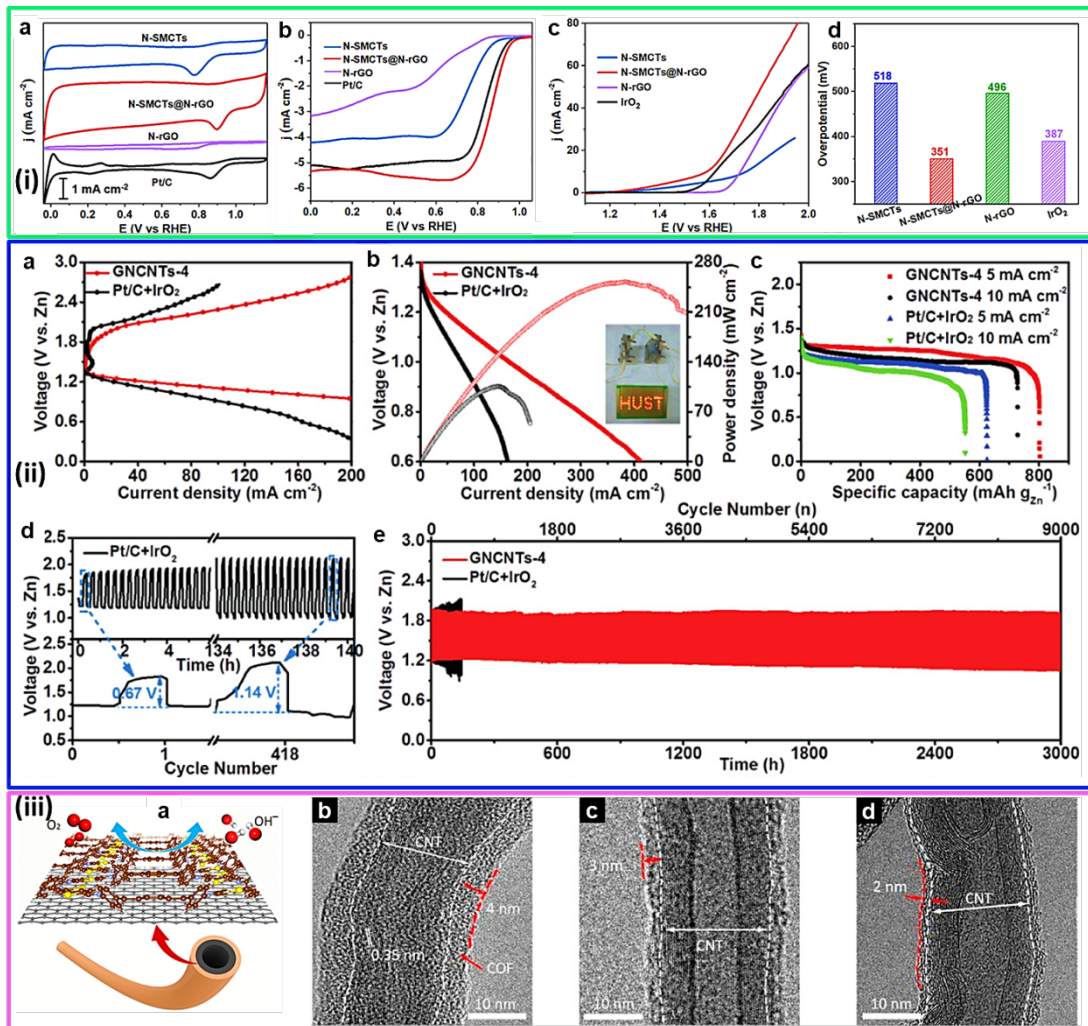


**Figure 3.** (i) Bifunctional electrocatalytic performance of N-SMCTs, N-rGO, Pt/C, and N-SMCTs@N-rGO catalysts. (a) ORR cyclic voltammetry (CV) and (b) LSV curves at 1600 rpm in  $\text{O}_2$  saturated 0.1 M KOH. (c) and (d) represents OER LSV curves and corresponding overpotential of N-SMCTs, N-rGO, IrO<sub>2</sub>, and N-SMCTs@N-rGO catalysts at 1600 rpm in  $\text{O}_2$  saturated 0.1 M KOH. Reproduced from Ref.<sup>114</sup> with permission from Elsevier, Copyright©2022. (ii) (a) Discharge/charge curves, (b) Discharge polarization curves and their resultant power density plots of GNCNTs-4 based ZABs and Pt/C+IrO<sub>2</sub> based ZABs, (c) Galvanostatic discharge curves at different current densities. Galvanostatic cycling stability of (d) Pt/C+IrO<sub>2</sub> based ZABs and (e) GNCNTs-4 based ZABs at 5  $\text{mA cm}^{-2}$ , respectively. Reproduced from Ref.<sup>24</sup> with permission from Wiley-VCH, Copyright©2020. (iii) (a) Schematic of the synthesis of one-dimensional van der Waals heterostructures (1D vdWHs) with carbon nanotube (CNT) core and a COF shell (CC-X). (b-d) TEM images of (b) CC-4, (c) CC-3, and (d) CC-2. Reproduced from Ref.<sup>116</sup> with permission from American Chemical Society, Copyright©2021.

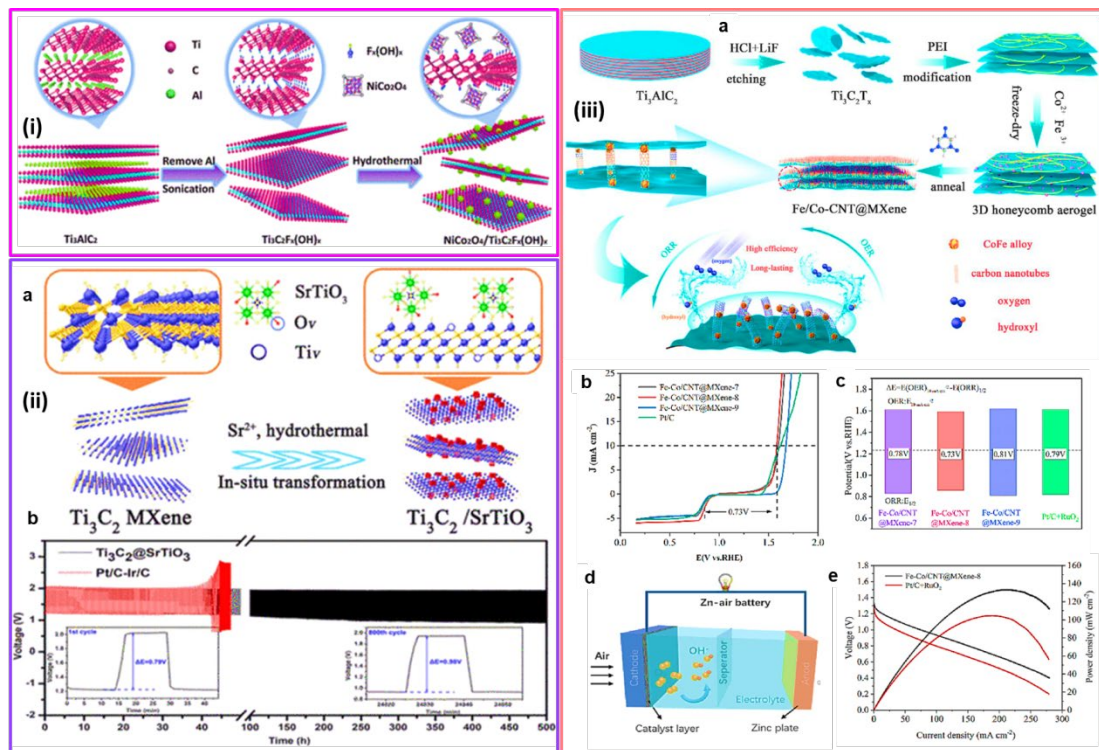


**Figure 4.** (i) Schematic of the fabrication of NiCo<sub>2</sub>O<sub>4</sub>/MXene catalyst. Reproduced from Ref.<sup>122</sup> with permission from American Chemical Society, Copyright©2020. (ii) (a) Schematic of the fabrication of vacancy defect-rich heterostructured SrTiO<sub>3</sub>/Ti<sub>3</sub>C<sub>2</sub>, and (b) Galvanostatic cycling stability of SrTiO<sub>3</sub>/Ti<sub>3</sub>C<sub>2</sub> based ZABs. Reproduced from Ref.<sup>125</sup> with permission from American Chemical Society, Copyright©2022. (iii) Illustration of the fabrication of Fe/Co-CNT@MXene-T catalyst, (b) Bifunctional catalytic activity of Fe/Co-CNT@MXene catalysts, and (c) their corresponding  $\Delta E$  values. (d) Schematic of Fe/Co-CNT@MXene-T catalyst based rechargeable ZAB and the catalyst power density plots (e). Reproduced from Ref.<sup>127</sup> with permission from Elsevier, Copyright©2021.

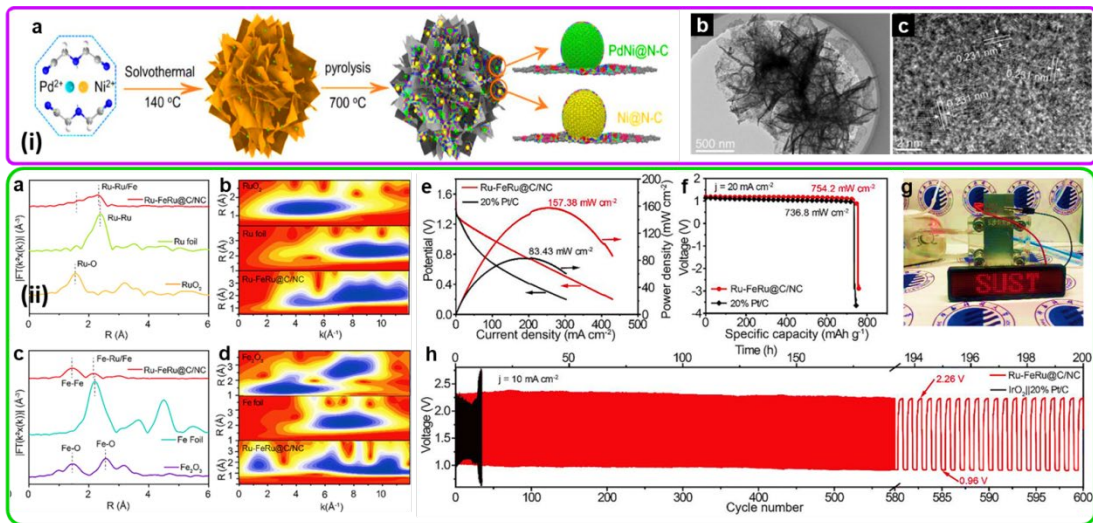


**Figure 5.** (i) (a) Schematic of the fabrication route of hierarchical heterostructure PdNi/Ni@N-C catalyst, (b-c) TEM and HR-TEM images of hierarchical PdNi/Ni@N-C catalyst. Reproduced from Ref.<sup>139</sup> with permission from Elsevier, Copyright©2021. (ii) (a-b) Fourier-transform EXAFS spectra and (b) Wavelet transform of Ru K-edge of Ru-FeRu@C/NC, with their respective Ru foil, and RuO<sub>2</sub>, respectively. (c-d) Fourier-transform EXAFS spectra and Wavelet transform of Fe K-edge of Ru-FeRu@C/NC, with their respective Fe foil, and Fe<sub>2</sub>O<sub>3</sub>. (e) Discharging polarization curves and resultant power density plots of the ZABs made by Ru-FeRu@C/NC and Pt/C, respectively. (f) Specific capacity tests for ZABs made by Ru-FeRu@C/NC and Pt/C, respectively. (g) Digital photograph of LEDs powered by the Ru-FeRu@C/NC-based ZABs. (h) Cycling stability ZABs assembled by Ru-FeRu@C/NC and IrO<sub>2</sub>||Pt/C under a discharge/charge current density of 10 mA cm<sup>-2</sup>. Reproduced from Ref.<sup>141</sup> with permission from Elsevier, Copyright©2022.

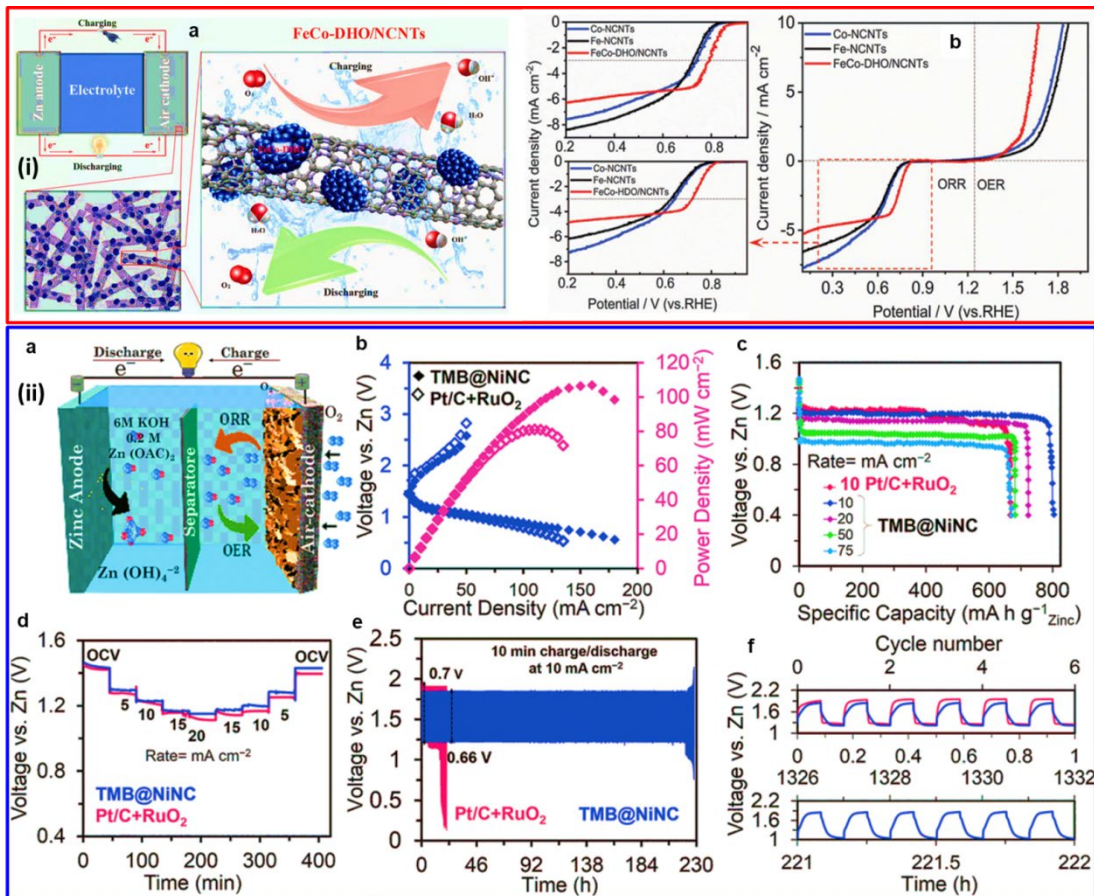


**Figure 6.** (i) Schematic of FeCo-DHO/NCNTs catalysts ZAB configuration and mechanism, (ii) Schematic of rechargeable ZABs based on Zn powder electrode and an air electrode of TMB@NiNC, (iii) ORR activity of Fe-NCNTs, Co-NCNTs, and FeCoDHO/NCNTs catalysts in 1.0 M KOH and 0.1 M KOH region and their Bifunctional ORR and OER activity in  $O_2$ -saturated 1.0 M KOH. Reproduced from Ref.<sup>152</sup> with permission from Wiley-VCH, Copyright©2018. (ii) Schematic of rechargeable ZABs based on Zn powder electrode and an air electrode of TMB@NiNC, (b) Power density plots for TMB@NiNC based ZABs and Pt/C+RuO<sub>2</sub> based ZABs, (c-d) Specific capacity test and Galvanostatic discharge test at different current densities for ZABs, (e-f) Durability tests of the ZABs based on the TMB@NiNC and Pt/C+RuO<sub>2</sub> at a current density of  $10\ mA\ cm^{-2}$ . Reproduced from Ref.<sup>154</sup> with permission from Wiley-VCH, Copyright©2023.

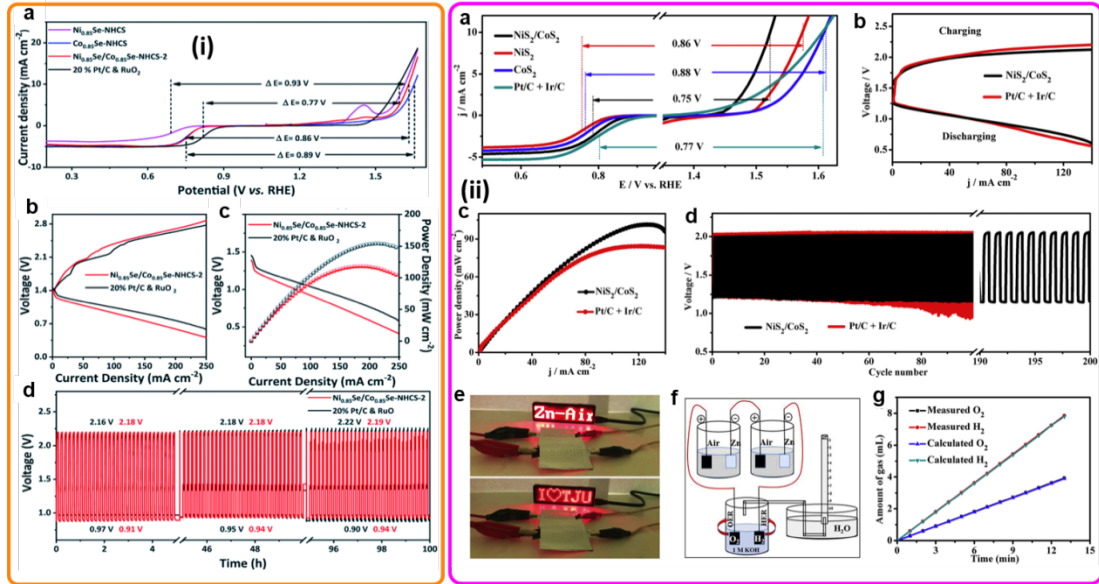


**Figure 7.** (i) (a) Bifunctional ORR/OER overpotential of  $\text{Ni}_{0.85}\text{Se-NHCS}$ ,  $\text{Co}_{0.85}\text{Se-NHCS}$   $\text{Ni}_{0.85}\text{Se}/\text{Co}_{0.85}\text{Se-NHCS-2}$  and  $\text{Pt/C+RuO}_2$  catalysts, (b) Charge/discharge polarization curves, (c) Power density plots and (d) Durability tests by charge and discharge of ZABs assembled with  $\text{Ni}_{0.85}\text{Se}/\text{Co}_{0.85}\text{Se-NHCS-2}$  and  $\text{Pt/C+RuO}_2$  at  $25 \text{ mA cm}^{-2}$ . Reproduced from Ref.<sup>165</sup> with permission from Royal Society of Chemistry, Copyright©2021. (ii) (a) Bifunctional ORR/OER overpotential of  $\text{CoS}_2$ ,  $\text{NiS}_2$ ,  $\text{NiS}_2/\text{CoS}_2$ , and  $\text{Pt/C+Ir/C}$  catalysts, (b) Charge/discharge polarization curves, (c) power densities and (d) cycling performance of the  $\text{NiS}_2/\text{CoS}_2$ -based ZABs. (e) Digital photographs of LEDs driven by  $\text{NiS}_2/\text{CoS}_2$ -based ZABs. (f-g) Schematic of self-driven water splitting powered by two-series-connected  $\text{NiS}_2/\text{CoS}_2$ -based ZABs and their corresponding evolved amount of  $\text{H}_2$  and  $\text{O}_2$  gases. Reproduced from Ref.<sup>169</sup> with permission from Elsevier, Copyright©2019.

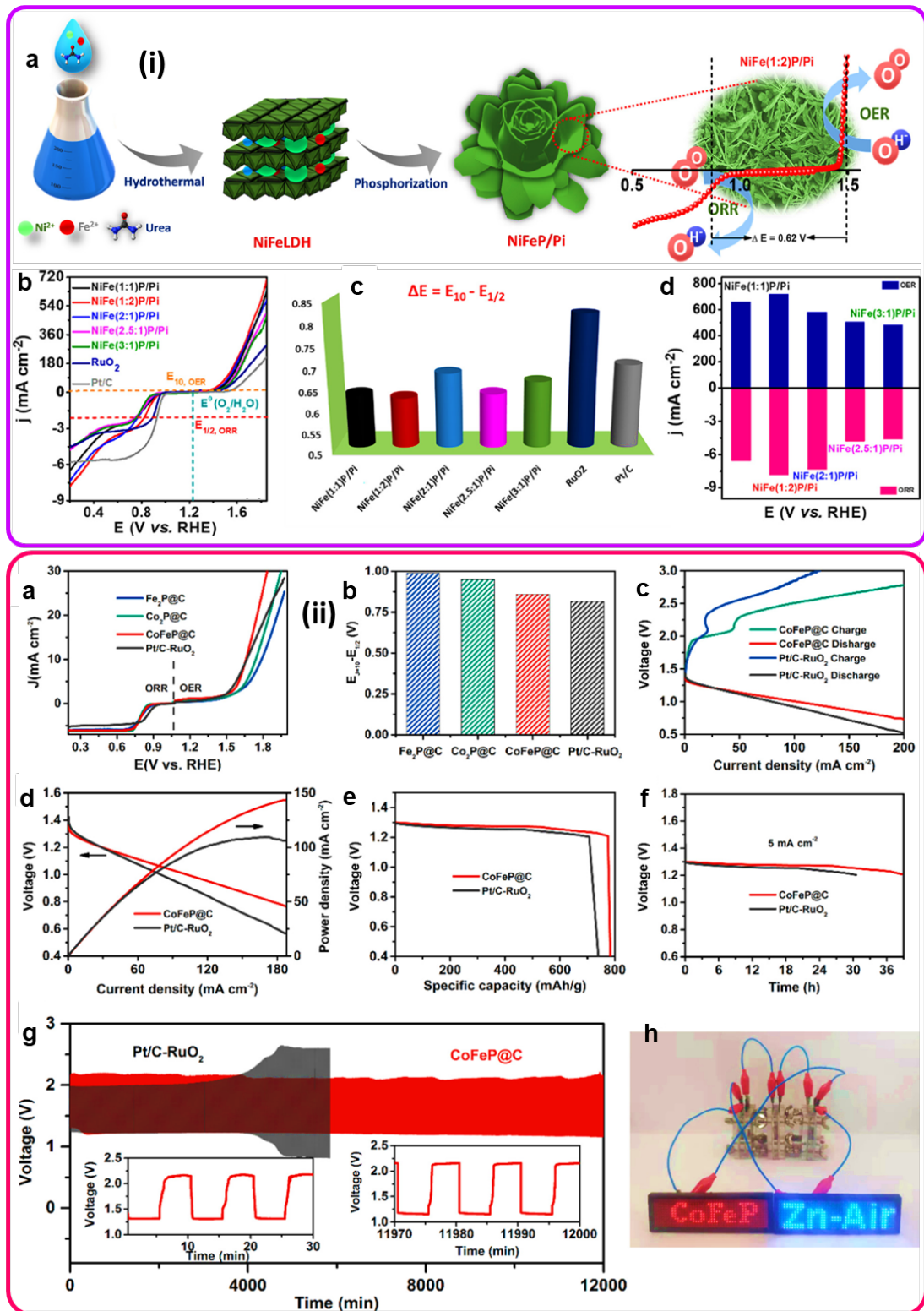


**Figure 8.** (i) (a) Schematic of the preparation of NiFeP/Pi catalyst, (b-d) Bifunctional ORR and OER performance of Ni/Fe metal ratios varied NiFeP/Pi catalysts and their bifunctional overpotentials as well their current density respectively. Reproduced from Ref.<sup>180</sup> with permission from American Chemical Society, Copyright©2021. (ii) (a) Bifunctional ORR and OER LSV curves of various catalysts in 0.1 M KOH electrolytes. (b) Histogram of bifunctional overpotential. (c-d) Charge/discharge curves and power density curves of the CoFeP@C based ZABs compared with Pt/C+RuO<sub>2</sub> based ZABs.

(e-f) Specific capacity and durability tests for CoFeP@C based ZABs compared with Pt/C+RuO<sub>2</sub> based ZABs, respectively. (g) Charging and discharging curves of the CoFeP@C based ZABs compared with Pt/C+RuO<sub>2</sub> based ZABs at the current density of 2 mA cm<sup>-2</sup>. (h) Photograph of LED screens driven by CoFeP@C based ZABs. Reproduced from Ref.181 with permission from American Chemical Society, Copyright©2021.

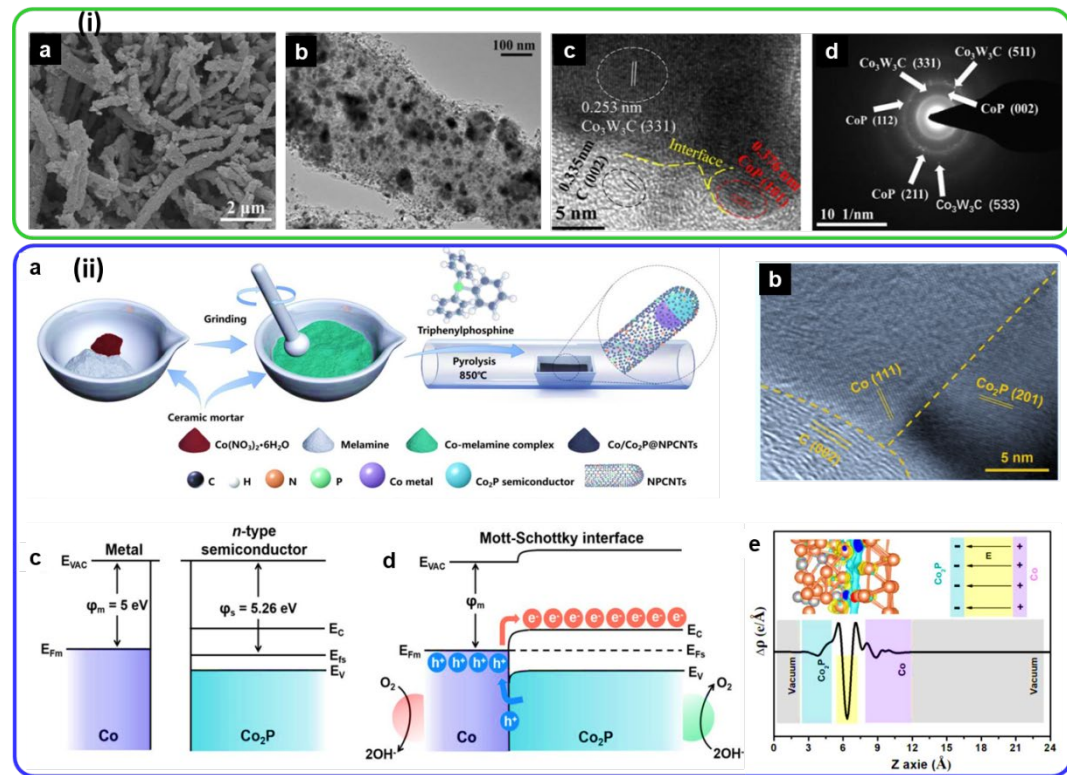


**Figure 9.** (i) (a-c) SEM, TEM, and HR-TEM images of CoWCP-NPC-2:1 catalyst, respectively. (d) SAED pattern of CoWCP-NPC-2:1 catalyst. Reproduced from Ref.<sup>192</sup> with permission from Elsevier, Copyright©2022. (ii) (a) Schematic of the production of Co/Co<sub>2</sub>P@NPCNTs electrocatalyst, (b) HR-TEM image of Co/Co<sub>2</sub>P@NPCNTs hetero-interface. Energy band diagrams for n-type Co<sub>2</sub>P semiconductor and Co metal (c) before and (d) after Schottky contact, whereas, EVAC vacuum energy is denoted as E<sub>VAC</sub>, E<sub>F</sub> is Fermi level, vacuum electrostatic potential is φ, the conduction band is denoted as E<sub>c</sub>, and the valence band is E<sub>v</sub>. (e) Charge density difference plot of Co/Co<sub>2</sub>P heterojunction, whereas, the left inset is the atomic model of Co/Co<sub>2</sub>P heterojunction and the right inset is the schematic of formation of built-in electric fields. Reproduced from Ref.<sup>193</sup> with permission from Elsevier, Copyright©2021.

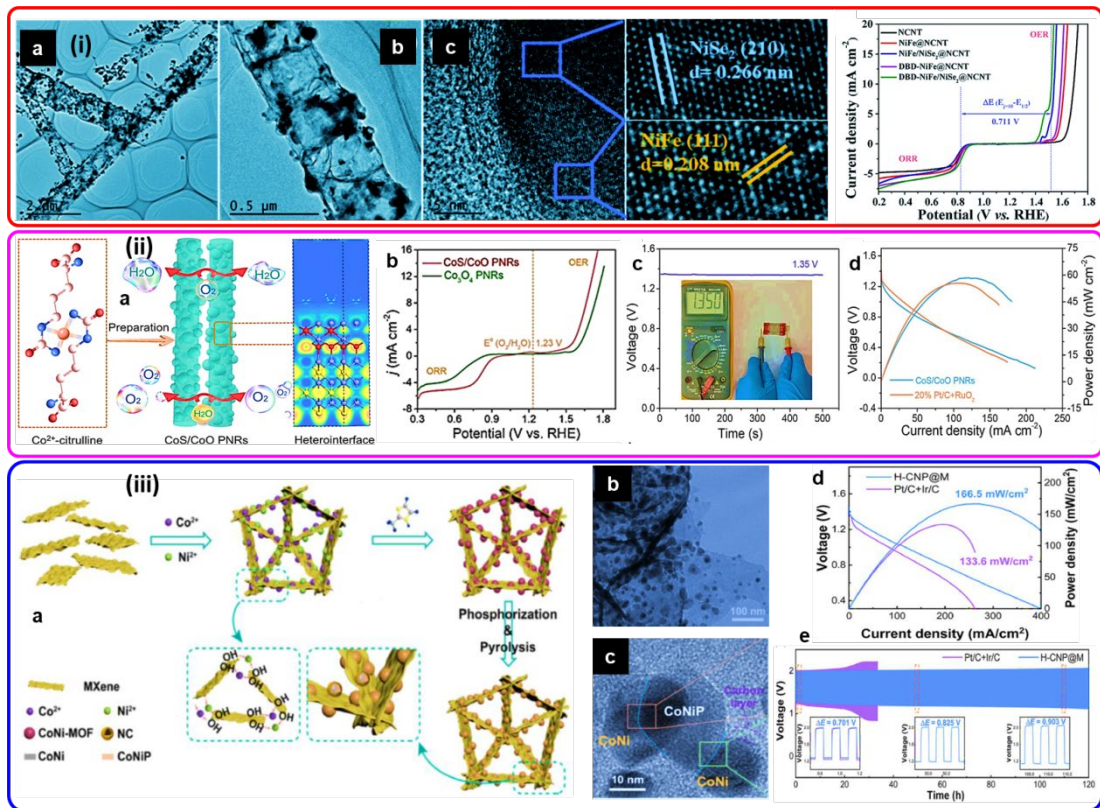


**Figure 10.** (i) (a-c) TEM images, and SAED pattern of DBD-NiFe/NiSe<sub>2</sub>@NCNT catalyst, the heterointerface region between NiSe<sub>2</sub> and NiFe-LDH was designated (c). (d) Bifunctional ORR and OER performance of DBD-NiFe/NiSe<sub>2</sub>@NCNT catalyst. Reproduced from Ref.<sup>196</sup> with permission from Royal Society of Chemistry, Copyright©2022. (ii) (a) Charge density difference of CoS/CoO PNRs, whereas, yellow and blue colours represent electron depletion and electron accumulation respectively. (b) Bifunctional ORR and OER performance of Co<sub>3</sub>O<sub>4</sub> and CoS/CoO PNRs catalyst. (c-d) Open circuit potential and power density plots of CoS/CoO PNRs based ZABs. Reproduced from Ref.<sup>197</sup> with permission from Elsevier, Copyright©2021. (iii) (a) Schematic of the synthesis of H-CNP@M, (b-c) TEM and HR-TEM images of H-CNP@M, (d) Discharge polarization curves and the equivalent power density of H-CNP@M based ZABs and Pt/C+IrC based ZABs. (e) Galvanostatic charge/discharge curves ZABs at 10 mA cm<sup>-2</sup>. Reproduced from Ref.<sup>119</sup> with permission from Elsevier, Copyright©2023.

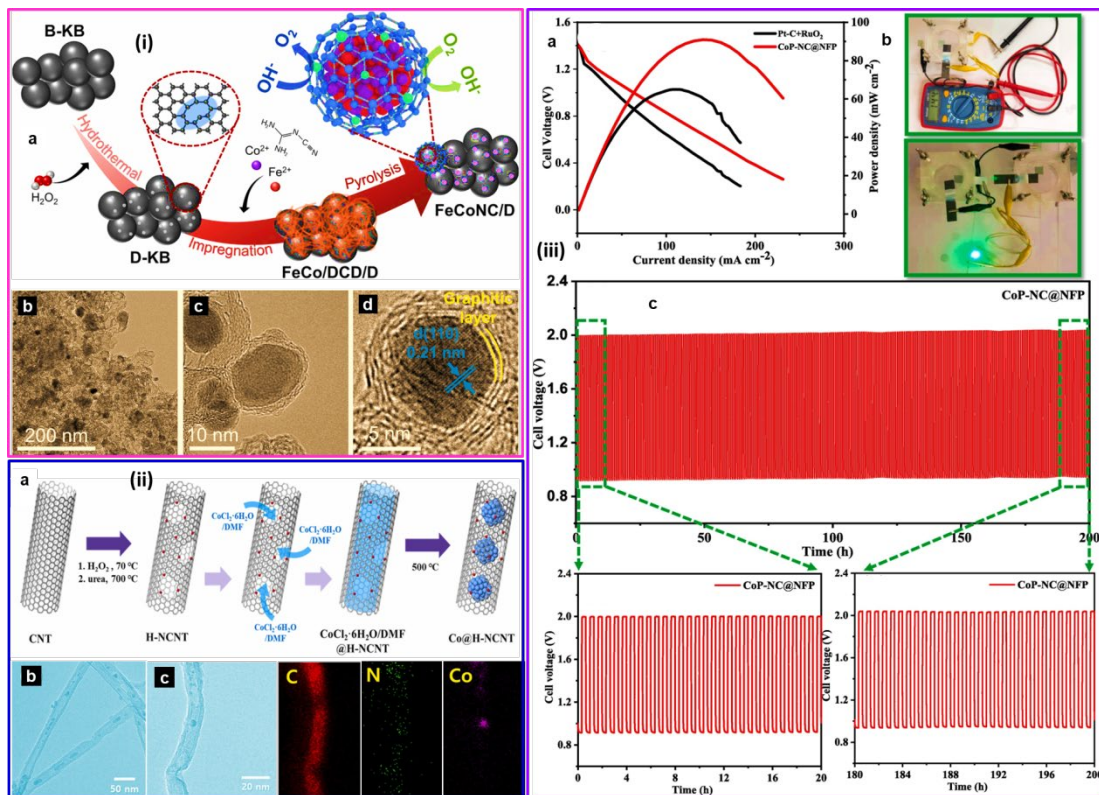
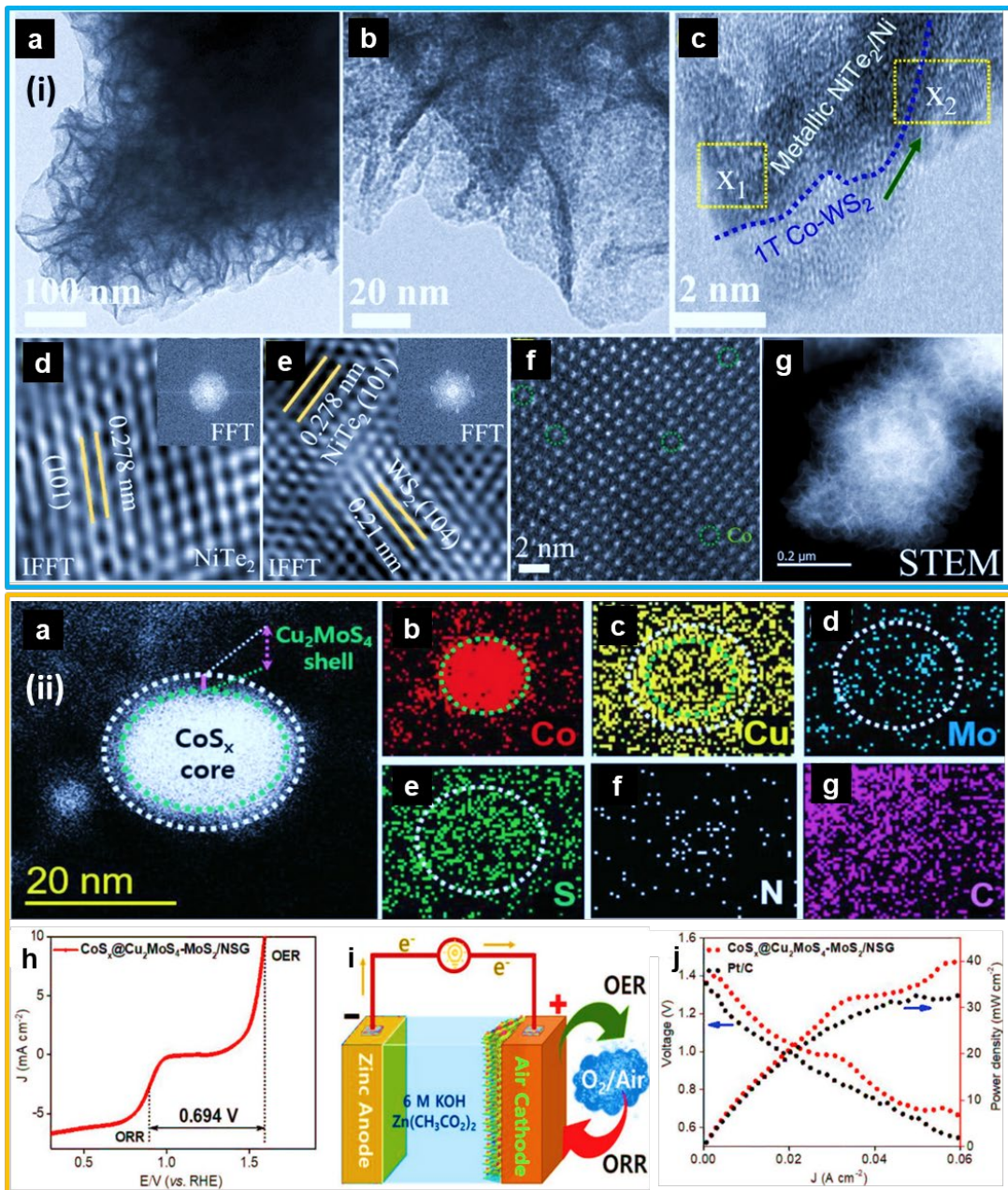


**Figure 11.** (i) Schematic of synthesis of FeCoNC/D catalyst, (b-d) TEM and HR-TEM images of FeCo alloy and graphitic layers in FeCoNC/D catalyst. Reproduced from Ref.<sup>209</sup> with permission from Elsevier, Copyright©2022. (ii) Schematic illustration for the preparation of Co@H-NCNT, (b-c) TEM and HR-TEM images, and the EDS mapping of Co@H-NCNT. Reproduced from Ref.<sup>57</sup> with permission from Elsevier, Copyright©2023. (iii) (a) Performance of the ZABs assembled by CoP-NC@NFP air electrode, (b) Photo images of the assembled ZABs, presenting the open circuit voltage (upper) and powering a green LED (lower) and; (c) Galvanostatic charge/discharge test at a current density of 2 mA cm<sup>-2</sup>. Reproduced from Ref.<sup>211</sup> with permission from Elsevier, Copyright©2022.



respectively. Reproduced from Ref.<sup>220</sup> with permission from Wiley-VCH, Copyright©2020.

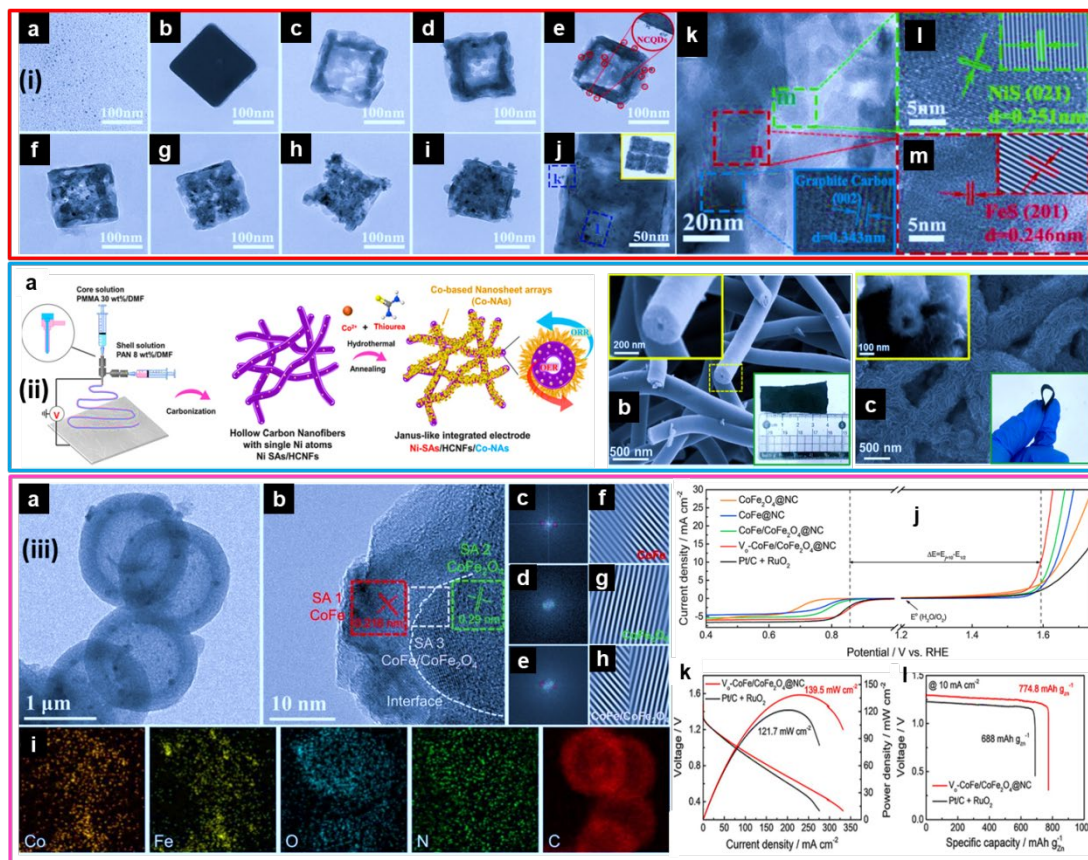


**Figure 13.** (i) TEM images of NCQDs (a), NiFePBA (b), E-NiFePBA (c), Ni-Fe-S (d), and Ni-Fe-S/xNCQDs ( $x = 1$  (e), 2 (f), 3 (g), 4 (h) and 5 (i)). TEM images of Ni-Fe-S/xNCQDs (j); HR-TEM images of Ni-Fe-S/xNCQDs (k and l correspond to the square regions marked in TEM image (j)); (l) and (m) correspond to the square regions marked in HRTEM image (l)). Reproduced from Ref.<sup>226</sup> with permission from Elsevier, Copyright©2023. (ii) Schematic of the preparation of Ni-SAs/HCNFs/Co-NAs. The SEM images of (b) Ni-SAs/HCNFs and (c) Ni-SAs/HCNFs/Co-NAs, respectively. Insets display corresponding magnified images and digital photos. Reproduced from Ref.<sup>101</sup> with permission from American Chemical Society, Copyright©2022. (iii) (a-b) TEM and HR-TEM images including three different selected areas including SA1 for CoFe, SA2 for CoFe<sub>2</sub>O<sub>4</sub>, and SA3 for CoFe/CoFe<sub>2</sub>O<sub>4</sub> and heterointerface between CoFe and CoFe<sub>2</sub>O<sub>4</sub>, (c-e) corresponding FFTs, (f-h) inversed FFT images of the SAs, and (i) EDS mapping of Vo-CoFe/CoFe<sub>2</sub>O<sub>4</sub>@NC. (j) Bifunctional ORR/OER LSV curves of CoFe@NC, CoFe<sub>2</sub>O<sub>4</sub>@NC, CoFe/CoFe<sub>2</sub>O<sub>4</sub>@NC, Vo-CoFe/CoFe<sub>2</sub>O<sub>4</sub>@NC, and Pt/C+RuO<sub>2</sub> catalysts, (k) Power density plots and (l) Galvanostatic discharge curves at a constant current density of 10 mA cm<sup>-2</sup> for Vo-CoFe/CoFe<sub>2</sub>O<sub>4</sub>@NC based ZABs, and Pt/C+RuO<sub>2</sub> based ZABs, respectively. Reproduced from Ref.<sup>230</sup> with permission from Elsevier, Copyright©2022.

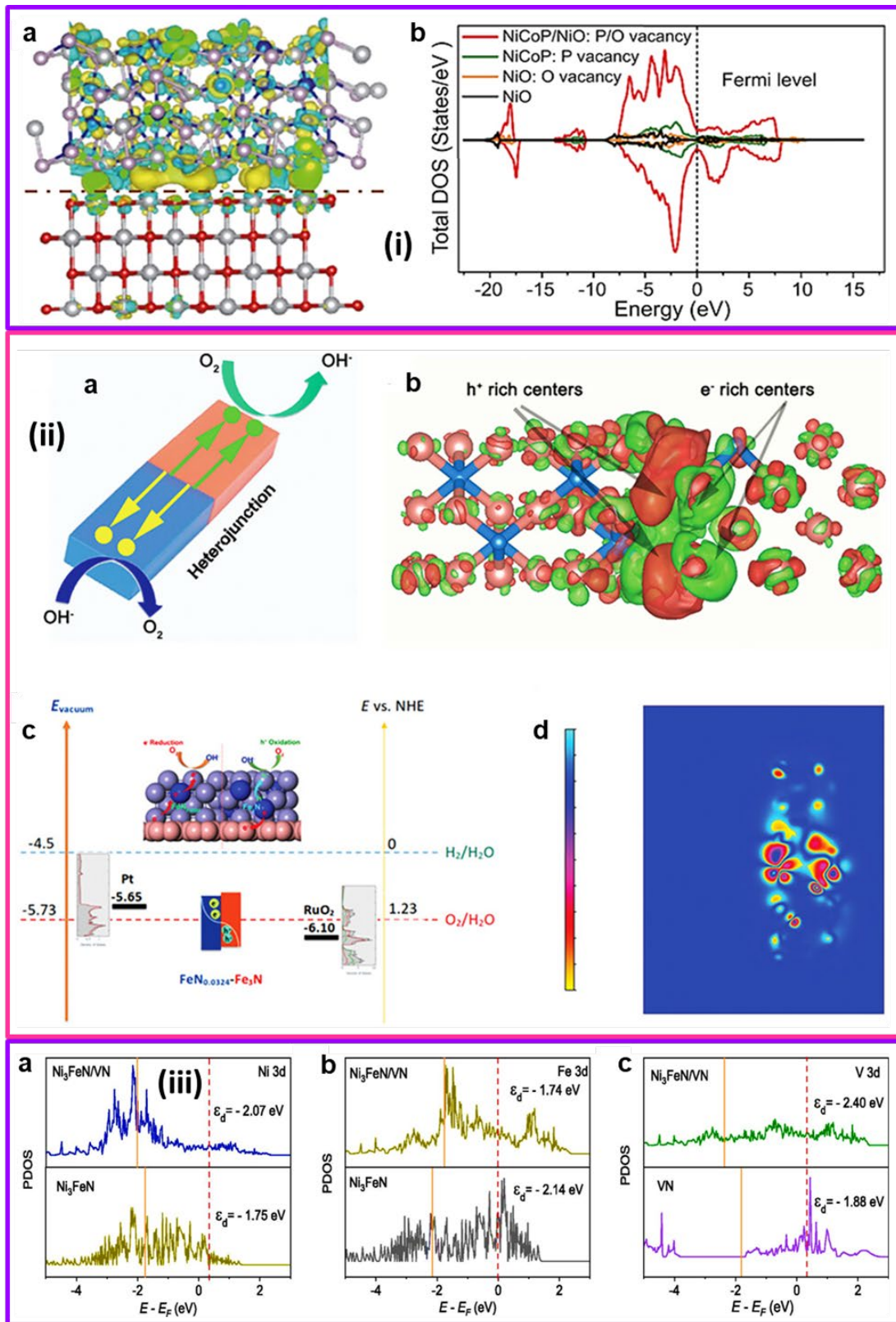
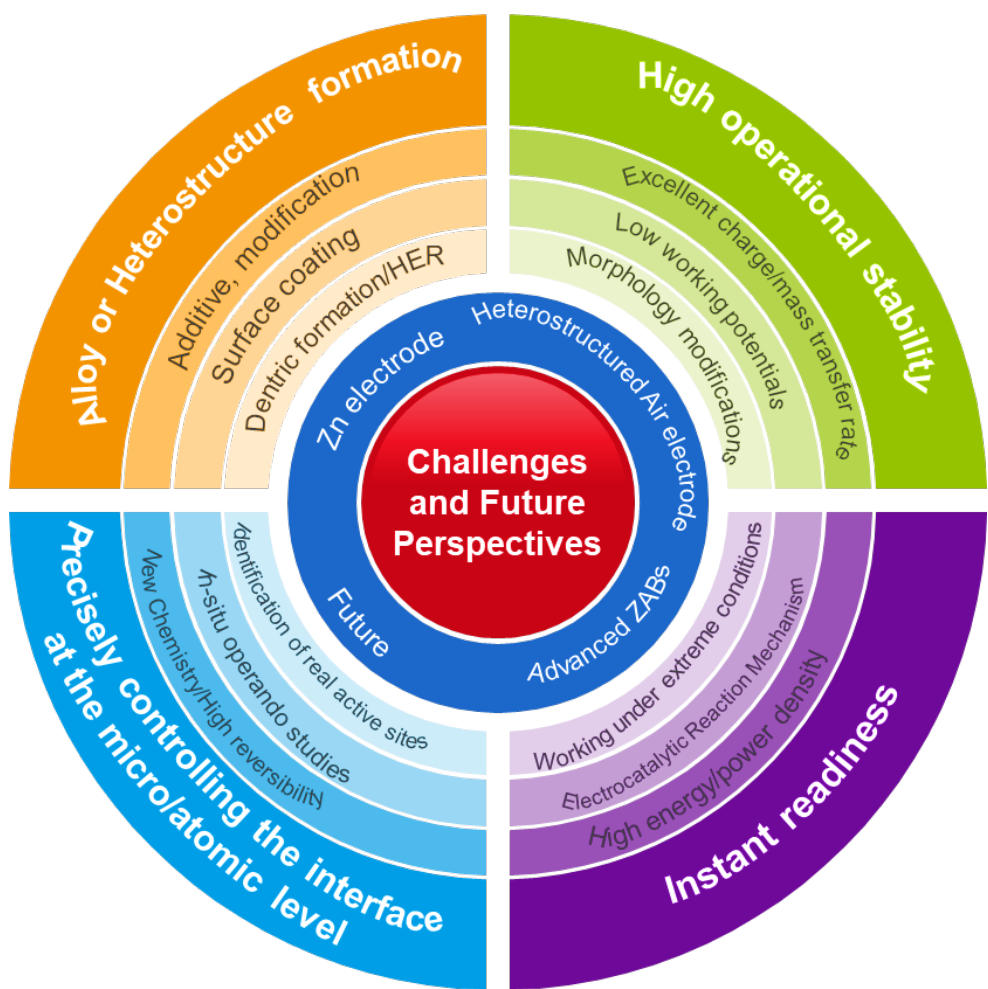


**Figure 14.** (i) (a) Interfacial charge density difference of NiCoP/NiO heterostructure. Yellow and Cyan isosurfaces stand for charge accumulation and depletion in the system, respectively. (b) Total density of states (TDOS) of NiO, NiO:O vacancy, NiCoP:P vacancy, and NiCoP/NiO:P/O vacancy. Reproduced from Ref.<sup>240</sup> with permission from Elsevier, Copyright©2023. (ii) (a) Schematic representation of the

spontaneous internal electric field in the  $\text{Fe}_3\text{N}-\text{FeN}_{0.0324}$  heterojunction. (b) The electron-/hole-rich centers in heterojunctions attained from DFT calculations, (c) the density of states (DOS) near the Fermi level of heterojunction versus vacuum and NHE, (d) the cross-sectional charge density difference of the heterojunction shows the loss of electron density (orange) and enrichment (green) in the heterojunction. Reproduced from Ref.<sup>38</sup> with permission from Wiley-VCH, Copyright©2023. (iii) (a) The electronic density of states of (a) Ni 3d (b) Fe 3d and (c) V 3d orbitals in  $\text{Ni}_3\text{FeN}/\text{VN}$  and  $\text{Ni}_3\text{FeN}$ , respectively. Reproduced from Ref.<sup>246</sup> with permission from Elsevier, Copyright©2022.



**Scheme 3.** Scheme showing challenges and future outlook on the progress of rechargeable zinc-air batteries (ZABs).

**Table 1.** Robust bifunctional electrocatalytic ORR/OER activity and their zinc-air battery (ZAB) performance of reported advanced heterostructured catalysts

Electrocatalyst	Synthesis method	ORR $E_{1/2}$ (V vs. RHE)	OER $E_{J10}$ (V vs. RHE)	$\Delta E = E_{J10} - E_{1/2}$ (V)	ZAB performance			Ref
					Open circuit voltage (V)	Current density (mA cm <sup>-2</sup> ) and Power density (mW cm <sup>-2</sup> )	Specific capacity (mA h g <sup>-1</sup> ) and Durability (h)	
N,S-GOQD-RGO/CNT	Hydrothermal method followed by annealing	0.84	1.62	0.78	1.414	— 134.3 mW cm <sup>-2</sup>	—	115
N-SMCTs@N-rGO	Hydrothermal method followed by urea-assisted pyrolysis strategy	0.87	1.581	0.711	1.485	159.0 mA cm <sup>-2</sup> ; 126.0 mW cm <sup>-2</sup>	— 500 cycles	114
CoNi-MOF/rGO	Wet chemical method followed by pyrolysis strategy	0.88	1.71	0.83	1.37	120 mA cm <sup>-2</sup> ; 97 mW cm <sup>-2</sup>	711mA h g <sup>-1</sup> ; 102 h	90
Fe/Co-CNT@MXene-8	Freeze-drying followed by annealing	0.85	1.58	0.73	1.41	156 mA cm <sup>-2</sup> ; 138 mW cm <sup>-2</sup>	759mA h g <sup>-1</sup> ; 375 h	127
MnCo <sub>2</sub> O <sub>4</sub> /NGQD/MXene	Solvothermal method	0.69	1.54	0.85	1.461	156 mA cm <sup>-2</sup> ; 152.8 mW cm <sup>-2</sup>	753 mA h g <sup>-1</sup> ; 300 h	123
NiCoFeLDH/MXene/NCNT	Hydrothermal method	0.78	1.562	0.782	1.51	103 mA cm <sup>-2</sup> ; 63 mW cm <sup>-2</sup>	753mA h g <sup>-1</sup> ; 80 h	124
Nb <sub>2</sub> CO <sub>2</sub> @COF	Freeze-drying followed by annealing solution method	0.81	1.603	0.79	1.26	216 mA cm <sup>-2</sup> ; 75 mW cm <sup>-2</sup>	545mA h g <sup>-1</sup> ; 120 h	120
Pd/CoO <sub>x</sub> /d-NC	Solution method followed by reduction strategy	0.72	1.589	0.869	1.476	242 mA cm <sup>-2</sup> ; 184 mW cm <sup>-2</sup>	760.4mA h g <sup>-1</sup> ; 84 h	137

Ni SAs-Pd@NC	Solution method followed by annealing	0.84	1.61	0.77	1.44	$\bar{134.2 \text{ mW cm}^{-2}}$	$719.2 \text{ mA h g}^{-1}$ ; 700cycles	138
Ru-Co <sub>9</sub> S <sub>8</sub>	Solution method followed by annealing	0.80	1.393	0.593	1.36	$\bar{92 \text{ mW cm}^{-2}}$	$760 \text{ mA h g}^{-1}$ ; 500 h	142
Co/Co <sub>9</sub> S <sub>8</sub> @SNC900	Hydrothermal method followed by annealing	0.82	1.54	0.72	—	$163.2 \text{ mA cm}^{-2}$ ; $106.6 \text{ mW cm}^{-2}$	$\bar{107 \text{ h}}$	191
CoFeRu-oxides/LDH-2	Hydrothermal method followed partial oxidation	0.818	1.552	0.734	1.482	$268 \text{ mA cm}^{-2}$ ; $163 \text{ mW cm}^{-2}$	$730 \text{ mA h g}^{-1}$ ; 210 h	151
FeCo-DHO/NCNTs	Solvothermal method followed by pyrolysis strategy	0.86	1.55	0.69	1.48	$503 \text{ mA cm}^{-2}$ ; $326 \text{ mW cm}^{-2}$	$793 \text{ mA h g}^{-1}$ ; 350 h	152
CoFe-LDH@FeCo NPs-N-CNTs	Hydrothermal method followed by annealing	0.868	1.548	0.68	1.51	$172 \text{ mA cm}^{-2}$ ; $116 \text{ mW cm}^{-2}$	$799 \text{ mA h g}^{-1}$ ; 110 h	147
Ru-FeRu@C/NC	Hydrothermal method followed by annealing	0.9	1.575	0.675	1.48	$264 \text{ mA cm}^{-2}$ ; $157.38 \text{ mW cm}^{-2}$	$754.2 \text{ mA h g}^{-1}$ ; 600cycles	141
CoS <sub>2</sub> /Cu <sub>2</sub> S-NF	Electrospinning followed by annealing	0.80	1.53	0.73	1.49	$255.47 \text{ mA cm}^{-2}$ ; $260.60 \text{ mW cm}^{-2}$	$812.78 \text{ mAh g}^{-1}$ ; 590 h	159
Co <sub>9</sub> S <sub>8</sub> /Co <sub>1-x</sub> S@NSC	One-pot salt template-assisted pyrolysis procedure	0.86	1.52	0.66	1.48	$189.2 \text{ mA cm}^{-2}$ ; $141.9 \text{ mW cm}^{-2}$	$765.4 \text{ mAh g}^{-1}$ ; 2000 cycles	166
Ni <sub>3</sub> S <sub>4</sub> @CoS <sub>x</sub> -NF	Two-step hydrothermal method	0.662	1.562	0.90	1.90	$143.0 \text{ mW cm}^{-2}$	$792.3 \text{ mAh g}^{-1}$ ; 4000 cycles	160
Co/Co <sub>2</sub> P@NPCNTs	Solid state pyrolysis method	0.88	1.54	0.66	1.465	$318.3 \text{ mA cm}^{-2}$ ; $189.7 \text{ mW cm}^{-2}$	$\bar{200 \text{ h}}$	193
Fe-Co <sub>2</sub> P/Co@NC	Solution method followed by annealing	0.876	1.497	0.621	1.54	$217 \text{ mW cm}^{-2}$	$783 \text{ mAh g}^{-1}$ ; 155 h	98
CoO/Co <sub>x</sub> P	One-step phosphorization of	0.86	1.60	0.74	1.4	$122.73 \text{ mW cm}^{-2}$	$\bar{200 \text{ h}}$	105

	layered Co-hexamine metal-organic frameworks							
DBD-NiFe/NiSe <sub>2</sub> @NCNT	Dielectric barrier discharge plasma method	0.811	1.522	0.711	1.413	131.61 mW cm <sup>-2</sup>	802 mAh g <sup>-1</sup> ; 1000 cycles	196
Co <sub>3</sub> W <sub>3</sub> C/CoP/NPC	Electrospinning followed by phosphorization	0.803	1.43	0.627	1.411	205.5 mW cm <sup>-2</sup>	800.5 mAh g <sup>-1</sup> ; 83.5 h	192
NiCo/NiCo <sub>2</sub> S@NSCNT	Solution method followed by carbonization/sulfidation	0.865	1.579	0.714	1.50	239.72 mA cm <sup>-2</sup> ; 155.82 mW cm <sup>-2</sup>	756.16 mA h g <sup>-1</sup> ; 300 cycles	102
FeCo/NUCsSs	Co-precipitation method followed by carbonization	0.89	1.54	0.65	1.51	207.16 mA cm <sup>-2</sup> ; 152.38 mW cm <sup>-2</sup>	791.86 mA h g <sup>-1</sup> ; 102 h	207
CoFe-S@3D-S-NCNT	Chemical vapour deposition, pyrolysis and a subsequent hydrothermal sulfurization method	0.855	1.54	0.685	1.55	330 mA cm <sup>-2</sup> ; 223 mW cm <sup>-2</sup>	805 mA h g <sup>-1</sup> ; 900 h	210
Fe/Ni@NiCo-CNT	Low-temperature liquid reflux synthesis	0.80	1.547	0.747	1.427	104.8 mA cm <sup>-2</sup> ; 51.6 mW cm <sup>-2</sup>	796.5 mA h g <sup>-1</sup> ; 1500 cycles	216
MoS <sub>2</sub> @FeN-C NSs	Hydrothermal polymerization followed by annealing	0.80	1.59	0.79	1.47	114mA cm <sup>-2</sup> ; 78 mW cm <sup>-2</sup>	442 mA h g <sup>-1</sup> ; 22 h	217
H-Co@FeCo/N/C	Solution method followed by carbonization	0.9	1.608	0.698	1.45	50 mA cm <sup>-2</sup> ; 125.2 mW cm <sup>-2</sup>	— 200 h	184
Ni-Fe-S/3NCQDs	Co-precipitation method followed by hydrothermal and carbonization	0.85	1.525	0.675	1.40	93.9 mA cm <sup>-2</sup> ; 94 mW cm <sup>-2</sup>	845.27 mA h g <sup>-1</sup> —	226

NiFe-LDH/Fe <sub>I</sub> -N-C	Solution method followed by carbonization	0.90	1.55	0.65	1.54	— 205.0 mW cm <sup>-2</sup>	815mA h g <sup>-1</sup> ; 400 h	227
MnO@Cu-N-C	Hydrothermal polymerization followed by annealing	0.81	1.61	0.80	1.43	350 mA cm <sup>-2</sup> ; 196.8 mW cm <sup>-2</sup>	800 mAh g <sup>-1</sup> ; 650 h	185
<b>H-NSC@Co/NSC</b>	Epitaxial growth followed by pyrolysis	0.85	1.60	0.75	1.50	289.1 mA cm <sup>-2</sup> ; 246 mW cm <sup>-2</sup>	828 mAh g <sup>-1</sup> ; 2000 cycles	212

## TOC Graphic

